Configuration and Performance of Hydraulic Transformer Power Distribution Systems

A THESIS
SUBMITTED TO THE FACULTY OF THE GRADUATE SCHOOL
OF THE UNIVERSITY OF MINNESOTA
BY

Pieter James Gagnon

IN PARTIAL FULFILLMENT OF THE REQUIREMENTS
FOR THE DEGREE OF
MASTER OF SCIENCE

Perry Y. Li

September, 2016

Acknowledgements

This research was funded through NSF EEC-0540834 and the Center for Compact and Efficient Fluid Power. I would also like to acknowledge the valuable contribution of Takako Industries, INC, for their donation of several micropumps and micromotors. I wish to extend my gratitude to my fellow researchers - in particular Sangyoon Lee, Mohsen Saadat, and Kai Loon Cheong - for their unwavering support and invaluable companionship. Lastly, and far from least, I would like to thank my advisor Perry Li. As I build my contributions beyond the university, I will continue to hone the analytical methods were first formed under his guidance.

Dedication

This thesis is dedicated to my parents, James Gagnon and Rebecca Fillmore. In my youth they gave me a basic set of reasoning tools, built me a sandbox, and let me play. Everything subsequent was built on this environment they initially provided.

Abstract

Hydraulic transformers implemented in a common pressure rail architecture have been suggested as a means to efficiently distribute hydraulic power to a system of actuators. This thesis explores the role that the configuration of the system plays in the operating region and efficiency performance of the power distribution system.

The primary tool used in this thesis is a dynamic loss model of a hydraulic transformer. Full mathematical documentation and experimental parameter tuning are described. Six configurations for distributing power with a hydraulic transformer are presented, and it is shown that each configuration has a unique operating region and efficiency trend. The hydraulic circuit is given for a port switching transformer that utilizes valves to switch between configurations during operation, and experimental tests demonstrate successful switching on a prototype machine.

The maximum displacements of the two rotating groups within a set of hydraulic transformers distributing power to linear actuators driving the hip, knee, and ankle joints of a humanoid robot are optimized to maximize efficiency over a walking gait duty cycle. The resulting size ratios of the groups vary from a 1:1 ratio to a 1:2.4 ratio for the three duty cycles investigated. A comparison of the hydraulic transformer architecture against a throttling valve architecture for the humanoid robot indicates that the transformer system can achieve a distribution efficiency of 47.6%, which is a 31.9% increase over the throttling architecture distribution efficiency of 16.0%. The transformer system consumes 142 J to drive a single step of the walking gait, which is a decrease of 281 J from the 422 J required by the throttling architecture.

This thesis thoroughly captures the efficiency performance and operating region of hydraulic transformers, and demonstrates how system configurations can improve the performance of the system beyond what has been generally considered in previous literature. These factors can then be weighed along with complexity, size, control performance, production cost, and other such metrics to enable a decision as to whether transformers are an appropriate power distribution architecture for a given application.

Contents

Acknowledgements i

Dedication ii

Abstract iii

List of Tables vii

List of Figures viii

1 Introduction 1

1.1 Chapter Overview 1
1.2 Background 1
1.3 Literature Review 4
1.4 Research Objectives 7
1.5 Thesis Outline 8

2 Development of a Dynamic Loss Model of a Hydraulic Transformer 10

2.1 Chapter Overview 10
2.2 Transformer Description and Modeling Approach 11
2.3 Development of Dynamic Loss Model 13
2.4 Parameter Scaling 37
2.5 Map Generating Procedure 39
2.6 Experimental Parameter Identification 43
2.7 Loss Distributions 51

2.8 Chapter Summary 52

3 Impact of the Configuration of a Hydraulic Transformer on System Efficiency 54

3.1 Chapter Overview 54
3.2 Description of Hydraulic Transformer Configurations 55
3.3 Definition of Unit Efficiency 57
3.4 Definition of System Efficiency 60
3.5 Description of the Transformer and System Under Analysis in this Chapter 63
3.6 Efficiency Performance and Operating Regions of the Three Unit Configurations 65
3.7 Discussion of Three Unit Configurations 66
3.8 Efficiency Performance and Operating Regions of the Six System Configurations 70
3.9 Discussion of Six System Configurations 71
3.10 Generating a Composite Map from System Maps 74
3.11 Chapter Summary 77

4 Port Switching Experimental Implementation 79

4.1 Chapter Overview 79
4.2 Control Approach 80
4.3 Generation of the Porting Map 84
4.4 Port Switching Transition Event Results 84
4.5 Discussion of Port Switching Transition Events 92
4.6 Chapter Summary 96

5 Optimal Sizing: Humanoid Robot Case Study 98

5.1 Chapter Overview 98
5.2 Motivation for Investigating Optimal Rotating Group Sizes 99
5.3 Description of a Humanoid Robot System and Duty Cycle 101
5.4 Evaluating Total System Efficiency of a Trajectory for a Given Performance Map 107
5.5 Method for Evaluating a Point Within the Design Space 110

5.6 Results for D_1 D_2 Design Space Exploration for Hip, Knee, and Ankle Actuators . . . 113
5.7 Discussion of Results of D_1 D_2 Design Space Exploration . . . 117
5.8 Example of Efficiency Improvement Potential of a Variable Pressure Rail 118
5.9 Chapter Summary . . . 120

6 Comparison of Distribution Efficiency in a Humanoid Robot Case Study 122
6.1 Chapter Overview . . . 122
6.2 Objectives and Methods of Distribution Efficiency Comparison . . . 123
6.3 Description of Throttling Valve Architecture . . . 125
6.4 Power Trajectory Comparison and Efficiency Results . . . 128
6.5 Discussion of Efficiency Comparison . . . 133
6.6 Chapter Summary . . . 136

7 Conclusion 138
7.1 Review of Thesis Content . . . 138
7.2 Summary of Research Conclusions . . . 139
7.3 Recommendations for Future Work . . . 140

References 142

Appendix A. Model Parameters for Hydraulic Transformer Simulations 147

Appendix B. Model Parameters for Hydraulic Transformer Simulations 149

Appendix C. List of Instrumentation and Valves 150

List of Tables

2.1 Configuration Port Connections 26
3.1 Hydraulic transformer size parameters and constraints 64
3.2 System parameters 64
3.3 Port switch valve states for all six configurations 75
5.1 Comparison of full vs restricted optimization 117
5.2 Efficiency comparison of 20 MPa rail against a 5.3 MPa rail 120
6.1 Optimal rotating group sizes 125
6.2 Distribution Efficiency Results for Transformer and Throttling Architectures 130
6.3 Energy consumption for one cycle with transformer and throttling architectures 133
A.1 Transformer Simulation Parameters 148
B.1 Measured Dimensions of Takako Micropumps 149
C.1 Instrument and valve list 150

List of Figures

2.1 Hydraulic Transformer Architecture 11
2.2 Example Hydraulic Transformer Port Connections 12
2.3 Angular Location of Piston Bores within Rotating Group 14
2.4 Piston Top Dead Center ($\varphi_{p,k} = \pi$) and a general position ($0 < \varphi_{p,k} < \pi$) 15
2.5 Valve plate port orifice geometry 17
2.6 Piston orifice area over one cycle for 3.15 cc rotating group 18
2.7 Piston Leakage Pathways 20
2.8 Piston Shoe Geometry 21
2.9 Valve Plate Geometry 23
2.10 Transformer Port Connections PM-1 (Left) PM-2 (Center) PM-3 (Right) 26
2.11 Piston Forces 28
2.12 Piston Shoe Velocity Components 33
2.13 Piston Shoe Velocity Vectors 34
2.14 Takako 3.15 cc Micro Pump disassembled for parameter measurements . 38
2.15 Geometrical parameter scaling laws 38
2.16 Impact of fractional displacement on the efficiency of a 3.15 cc pump . . 40
2.17 Total transformer efficiency as a function of the fractional displacement of the 2nd unit, where the pressure ratio is fixed at 0.75 and output flow rate is fixed at 100 cc/s 41
2.18 Example point dispersion and convex hull of map generating procedure 43
2.19 Experimental Efficiency Maps of Prototype Transformer 45
2.20 Simulated efficiency maps of a prototype transformer with untuned shoe and valve plate gaps of 5 μm 46

2.21 Simulated efficiency maps of a prototype transformer with tuned shoe and valve plate gaps of 13.8 and 16.7 μm 48
2.22 Experimental efficiency maps of a 0.4 cc hydraulic pump 49
2.23 Simulated efficiency maps of a 0.4 cc hydraulic pump with untuned shoe and valve plate gaps of 13.8 μm and 16.7 μm respectively 50
2.24 Simulated efficiency maps of a 0.4 cc hydraulic pump with tuned shoe and valve plate gaps of 9.1 μm and 10.6 μm respectively 50
2.25 Simulated losses at three operating points for a transformer consisting of two 3.15cc rotating groups 52
3.1 Examples of two non-meaningful transformer configurations 56
3.2 Three meaningful transformer unit configurations 56
3.3 Series Architecture 57
3.4 Power Split Architecture 57
3.5 Six system configurations for distributing power with a hydraulic transformer from a common pressure rail 58
3.6 Boundary of Hydraulic Transformer Unit Within System 59
3.7 Boundary of Power Distributing System 61
3.8 Efficiency maps and operating regions of three transformer unit configurations operating off of a 20 MPa rail pressure, corresponding to three configurations shown in Figure 3.2 66
3.9 Efficiency maps and operating regions of six system configurations operating off of a 20 MPa pressure rail, corresponding to the six configurations shown in Figure 3.5 72
3.10 Example of how a power split configuration can achieve higher system efficiency than unit efficiency 73
3.11 Hydraulic circuit capable of switching between all six system configurations - valves shown in default position 75
3.12 Composite efficiency map of highest efficiency possible across all six configurations for an example transformer 76
3.13 A 'porting map' showing which configuration has the highest steady state efficiency for a given load flow rate and pressure drop 77
4.1 Experimental test bench used for investigating transition events 80

4.2 Hydraulic circuit used for investigating port switching behavior 81
4.3 Control approach used for port switching investigation 83
4.4 Composite efficiency map of the prototype transformer, with lines A - D showing approximate trajectories explored in this chapter 85
4.5 Porting map of the prototype transformer, showing which configuration is most efficient for each operating region. Lines A - D show approximate trajectories explored in this chapter 86
4.6 Transition event between mode 3 series configuration and mode 2 power split configuration, corresponding to line A on figure 4.5 88
4.7 Transition event through the origin, corresponding to line B on figure 4.5 90
4.8 Transition event between mode 2 series configuration and mode 2 power split configuration, corresponding to line C on figure 4.5 91
4.9 Transition events between mode 2 series configuration, mode 1 series configuration, and mode 2 power split configuration, corresponding to line D on figure 4.5 93
4.10 Transition event between mode 2 series configuration and mode 1 series configuration 94
5.1 Relationship between maximum efficiency of a hydraulic pump and its total displacement 100
5.2 Impact of fractional displacement on the efficiency of a 3.15 cc hydraulic pump 100
5.3 Example of a hydraulic humanoid robot 101
5.4 Schematic of common pressure rail hydraulic power distribution system 102
5.5 Hydromechanical actuator for humanoid robot joints 104
5.6 Torque and rotational velocity demand profiles for hip, knee, and ankle joint of humanoid robot 105
5.7 Force and velocity demand profiles for hip, knee, and ankle joint of humanoid robot 106
5.8 Power boundaries for humanoid robot joint actuator 108
5.9 Example of a composite efficiency map for a transformer with $D_{1,max} = D_{2,max} = 0.4cc$ operating off of a 1500 psi rail 111

5.10 Example of transforming the shape of the power demand trajectory with three different actuator cross-sectional areas 112
5.11 Total trajectory efficiency η_t for the hip duty cycle within the $D_{1,max}D_{2,max}$ design space 114
5.12 Total trajectory efficiency η_t for the knee duty cycle within the $D_{1,max}D_{2,max}$ design space 115
5.13 Total trajectory efficiency η_t for the ankle duty cycle within the $D_{1,max}D_{2,max}$ design space 115
5.14 Duty cycle trajectories for hip, knee, and ankle systems overlaid on the optimal composite efficiency maps 116
6.1 Schematic of hydraulic common pressure rail power distribution system with generic power distribution and control devices 124
6.2 Boston Scientific's BigDog robot, as an example of a mobile robot using a throttling valve architecture to control a system of linear actuators . . 126
6.3 Throttling valve power distribution architecture 126
6.4 Power, Pressure, and demand profiles for hip actuator 130
6.5 Power, Pressure, and demand profiles for knee system 131
6.6 Power, Pressure, and demand profiles for ankle system 132

Chapter 1

Introduction

1.1 Chapter Overview

This chapter specifies the research objectives of this thesis and provides context in order to facilitate an understanding of how the work builds upon and extends existing literature. Section 1.2 describes a brief background, introducing the concept of a hydraulic transformer and explaining its potential as a means of distributing hydraulic power. Section 1.3 reviews the existing literature on hydraulic transformers, with emphasis on system configuration and efficiency performance work that is closely related to the activities of this thesis. Section 1.4 explicitly states the research objectives of this thesis and section 1.5 gives a brief overview of the contents of the document.

1.2 Background

Engineering design work is essentially a complex multi-objective optimization problem. Choosing the physical form that a solution will take is often a process of evaluating the performance of several options across a range of competing metrics. Electric motors, pneumatic actuators, internal combustion engines, and hydraulic actuators are some general classes of devices that should be considered when a requirement is motion generation or imparting forces on the environment. Hydraulic actuators benefit from exceedingly high power density and the capability for precise control. Therefore, when it comes to a subclass of high force and low velocity duty cycles, hydraulic actuators

generally dominate due to their ability to meet power and control requirements in a compact, reliable, and cost-effective package.

The majority of hydraulic actuators can be placed into two broad classes, rotary pump/motors and linear cylinders. In addition to deciding which actuator style is most appropriate for the application, it is also necessary to determine what architecture would be best to distribute power to the actuators. The most common method of powering multiple actuators is by distributing fluid power to them along a common pressure rail. The force or torque output of a hydraulic actuator is proportional to the product of the pressure drop across the device and the displacement of the device. Variable displacement rotary actuators are a mature technology, and their power output can be controlled off of the given pressure of the rail by varying their displacement. In contrast to this, there is no commercially available variable displacement linear actuator. The current approach is to use throttling valves to reduce the pressure supplied to the actuator and therefore control its power output.

The practice of throttling pressures down from a high distribution pressure incurs significant losses, and the use of throttling valves prevents the recovery of energy from overrunning loads. A state of the art solution is a load sensing system, which distributes fluid power at pressures slightly greater than the maximum that is instantaneously required. Such a system reduces throttling losses, but cannot eliminate them, as separate actuators will inevitably operate at different pressure levels. Another architecture of interest is displacement controlled systems, which has a dedicated pump for each actuator. Displacement control has shown impressive fuel efficiencies [1], but is a relatively young architecture and must yet demonstrate sufficient reliability to justify the increased system complexity prior to commercial adoption. Common pressure rail distribution architectures could remain competitive by the introduction of an efficient and cost effective means to control linear actuators. Hydraulic transformers have been suggested as a throttle-less device capable of achieving such an outcome.

A hydraulic transformer is a device that transforms fluid power conservatively from one pressure/flow combination to another pressure/flow combination. They are to the fluid domain as gear sets are to the rotary mechanical domain, levers are to the linear mechanical domain, and electrical transformers are to the electrical domain. Hydraulic transformers were suggested as early as 1894 [2], even prior to the introduction of the

first modern oil-based hydraulic system, which was developed in 1905 by Williams and Janney for the gun control systems of US warships [3]. The 1894 patent of a Transformer for Hydraulic Machines, submitted by T.R. Morgan, Sr. captures the essence of the objective of a transformer:

> "My invention relates to an improvement in devices for varying the pressure of the water supplied for actuating hydraulic machines. Heretofore the water supplied to hydraulic machines has been conveyed from the accumulator to the machine at accumulator pressure, and as practically all machines are constructed for light as well as heavy work it follows that when the machine is on light work the same power is not required as for heavy work. Hence the excess of power over and above the power actually required for the work is wasted. My devices are designed to be interposed between the accumulator and the machine actuated by the water for varying the pressure of water taken from the accumulator, whereby water at or above or below accumulator pressure may be supplied to the machine."

T.R. Morgan, Sr correctly recognized the potential that a machine such as a hydraulic transformer has to increase the distribution efficiency of a system where the average required pressure is significantly different than the maximum required pressure for the anticipated duty cycle. Morgan's transformer operated off of area differentials in cylinders to generate a change in the pressure and flow terms, but over the following decades various other designs were proposed as transformers evolved. In 1970 a transformer based off of two mechanically connected axial piston rotating groups was introduced, an early precursor to the design studied in this thesis [4].

During the 1960s [5, 6] the language of hydraulic transformer patents changed to clearly emphasize the need to reduce the size, mass and complexity of the machines. This focus eventually prompted the introduction of a novel transformer design by the Dutch hydraulic design firm, Innas, in 1997 [7]. Their transformer combined the functions of both a pump and a motor into a single rotating group through the use of a three kidney valve plate, in contrast to the traditional approach of keeping the functions separate in two different rotating groups.

As of 2015 transformer-based fluid power distribution have been shown to be more

efficient than traditional throttling valve architectures for a range of duty cycles. Despite this, the hydraulic industry has chosen not to adopt the technology for commercial use. The plethora of patents related to hydraulic transformers generated by industry clearly indicates that modern companies are aware of the technology. This choice can be understood by the acknowledgment that the evaluation of a power distribution technology extends beyond just its efficiency. In a commercial setting the architecture is also evaluated in terms of its performance in areas such as complexity, reliability, form factor, and production cost. Therefore, it can be inferred that the perceived efficiency performance of a transformer is not sufficiently greater than that of competing technologies to offset the reduced performance in other metrics. If transformers are to be adopted they must either reduce the costs or increase the perceived benefits.

1.3 Literature Review

The literature covering hydraulic transformers is diverse in topics and methodologies. Numerous designs of the machine itself have been suggested, and examined to varying degrees of completeness. The most thoroughly investigated form is one that consists of two axial piston rotating groups mechanically connected through a common shaft, first unambiguously introduced by Herbert Kouns in 1971 [4]. In addition to the axial piston design there have been numerous experimental designs, such as a hypothetical transformer utilizing a pair of variable displacement gear pumps patented in 2002 [8], a digital transformer utilizing area differences of a stepped shaft patented in 2012 [9], a radial piston transformer patented by Hirose Valve Industry in 2000 [10], and a transformer based on vane pump and motor technology patented by Caterpillar Inc in 2000 [11]. The available literature on the non-axial-piston designs is limited to descriptions of the machines in patents, and therefore the performance of the devices is not known.

In addition to the traditional axial piston approach of mechanically connecting two rotating groups, an alternative axial piston design was introduced in 1997 by the Dutch company Innas. The design combines the functions of a pump and a motor into a single rotating group through the introduction of a three kidney valve plate [3]. Although Innas has provided extensive qualitative discussions of the loss mechanisms of their transformer, documentation of rigorous simulation models has been limited. Experiments

by Innas have demonstrated a maximum unit efficiency of 88% on a non-optimized prototype unit [12].

Experimental efforts by Innas have indicated that although the controllability of a transformer is good at high speeds, stick-slip effects can make control at low speeds difficult [12]. The need for further development of low speed control strategies is acknowledged. CFD simulations of the Innas Hydraulic Transformer have allowed Jein et al [13] to conclude that operating the IHT at low control angles will lead to local cavitation within the high pressure port, creating excessive noise and wear during operation.

Consideration has been given to the many potential applications of a hydraulic transformer. Proposals for utilizing hydraulic transformers in passenger vehicles were suggested as early as 1955 [14], and more recently the Innas group has put out a set of publication on an effort to promote a common pressure rail architecture for passenger vehicles [15, 16] . Volvo Construction Equipment, in collaboration with Innas, published a simulation study where a 33 metric ton wheel loader undergoing a particular duty cycle with a common pressure rail architecture was shown to reduce fuel consumption by 51.4% as compared to a conventional system with mechanical transmission and load sensing hydraulic circuit [17]. Non-mobile applications have also been considered, such as in a 1983 patent by Mannesmann Rexroth of a control device for applying constant force on the ropes or cables of a mooring structure such as is found in shipyards [18] and a 2003 patent by Bosch Rexroth for a method of powering an injection molding machine [19].

Although the bulk of transformer literature focuses just on the transformer itself, several authors investigate how the system configuration influences the performance of a transformer. In 2003 Werndin and Palmberg compared the performance of two different configurations of the traditional two-rotating group transformer and an Innas Hydraulic Transformer [20]. Their work indicates that the IHT has a slightly greater peak efficiency, and that each configuration has a different operating region, although they caution against the preliminary nature of their results. Although the recognition of additional configurations of a traditional transformer was valuable, the results and discussion of their effort did not properly characterize the efficiency trends of the two configurations. The figures shown in their paper suggest that the second traditional

configuration is entirely dominated by the first traditional configuration, whereas the work in this thesis clearly indicates that each configuration has a region it performs better in.

The implications of system configuration for the traditional transformer design was more thoroughly investigated by Ho and Ahn in an effort that examined the performance of various configurations in driving a loaded cylinder [21]. In addition to a preliminary exploration of the operating regions of the various configurations and recognition that each configuration has its own strengths, Ho and Ahn presented a switching circuit that enabled a transformer system to switch between configurations during operating. A simulation of the switching circuit under five different duty cycles saw a reduction in energy expenditure of over 50% for one of the cases, and more modest gains between 0% and 20% for the other four duty cycles. It should be noted that the number of configurations investigated by Ho and Ahn were non-exhaustive, and several configurations with useful operating regions were not explored in their work.

A potentially valuable feature of hydraulic transformers is their ability to regenerate fluid power into the common pressure rail from an overrunning load. This behavior has been most thoroughly investigated in 2012 by Inoguchi, Ito, and Ikeo in a paper that examined the recovery of energy from a mass load on a cylinder being raised and lowered in the presence of gravitational forces [22]. The study indicated that up to 83.1% of the energy that would have been lost in a throttling circuit could be recovered by a proposed transformer circuit. They acknowledge that the duty cycle under examination is a simple one, and the impact of the regeneration option of a transformer under a more realistic duty cycle has yet to be investigated.

Both simulated and experimental investigations of all types of transformers have been with non-optimized machines. The separate functions of motoring and pumping occurring within axial piston transformers motivates the optimization of the displacements associated with each function for a particular duty cycle. The majority of studies consider machines where the displacements assigned to each task are equal. Werndin and Palmberg [20] as well as Inoguchi et al. [22] considered traditional transformers with unequal displacements, but in both studies only a single machine was characterized and the general trends of the possible design space was not explored. There exists a clear opportunity to investigate the potential benefits of optimizing the relative displacements

of the motoring and pumping functions within a transformer.

1.4 Research Objectives

This thesis seeks to thoroughly characterize the efficiency benefits of hydraulic transformers by improving the understanding of how they impact system performance. An exploration of several new system configurations will illustrate how current transformer machines can achieve higher system efficiencies across broader operating regions than what is generally attributed to them. Furthermore, methodologies for optimizing key design parameters of transformers will be demonstrated in a case study. Due to the fact that the types and relative weights of the metrics used to evaluate distribution technologies depends on the application, this thesis does not seek to make a general conclusion as to which distribution technology is the best. Therefore these studies aim to characterize the potential for energy savings through the use of hydraulic transformers, as a single input to the complex multi-objective optimization problem that is choosing the actual device for a specific application.

The specific objectives of this thesis are:

- Completely document the mathematical underpinnings of a dynamic loss model for an axial piston hydraulic transformer.
- Illustrate the difference between the efficiency of the transformer and the efficiency of the system the transformer is within, and demonstrate how certain configurations enable system efficiencies greater than maximum possible transformer efficiencies.
- Characterize the steady state efficiency performance and operating regions of six different configurations of a hydraulic transformer based power distribution system, including four configurations yet unstudied in literature.
- Experimentally demonstrate the ability to switch between various configurations during operation by the introduction of directional valves.
- Outline a methodology for optimizing the size of the transformer rotating groups to maximize efficiency for a particular duty cycle and demonstrate the results of

such an optimization for the leg joints of a humanoid robot.

- Compare the efficiency performance of a hydraulic transformer distribution system against a throttling valve distribution system in a humanoid robot case study.

1.5 Thesis Outline

This thesis consists of seven chapters and an appendices with supporting information. This first chapter has briefly covered the background of hydraulic power distribution and motivated the potential benefits of a common power rail power distribution system. The concept of a hydraulic transformer was introduced, and the various forms that such a machine have taken were reviewed. Relevant literature on the topic of hydraulic transformers was reviewed and knowledge gaps were identified. The objectives of this thesis were presented.

Chapter two gives a detailed description of the mathematical underpinnings of the dynamic loss model that has been used to generate all of the simulation results of this thesis. The physical architecture of the transformer under consideration is described, and the trends of various dimensions as a function of the maximum displacement of the unit are discussed. The procedure for generating performance maps is described.

Chapter three describes six ways in which a transformer can be configured within a hydraulic power distributing system. Performance maps for the entire operating region of each of the six configurations are given in order to show the variation in efficiency trends. The concept of switching between configurations during operation is presented, hereafter called port switching, and a circuit that could achieve such a result is given.

Chapter four shows the results of an experimental effort exploring the implementation of port switching. Emphasis is given to the transformer behavior when transitioning between configurations.

Chapter five presents a case study in which the maximum displacements of the two transformer rotating groups is optimized to maximize the efficiency of actuators controlling three joint on a humanoid robot.

Chapter six presents a case study examining the use of hydraulic transformers for

distributing power to actuators controlling three joints on a humanoid robot. A methodology is described for optimizing the size of the two transformer rotating groups to maximize efficiency for the duty cycles under consideration. The optimal rotating group sizes are given.

Chapter six presents a case study comparing the efficiency of a hydraulic transformer architecture against the efficiency of a throttling valve architecture for distributing power to the same humanoid robot.

Chapter seven consists of a summary of the findings of the thesis and recommendations for future work.

Chapter 2

Development of a Dynamic Loss Model of a Hydraulic Transformer

2.1 Chapter Overview

This chapter gives a detailed documentation of the dynamic loss model that was created as a tool to explore the performance of hydraulic transformers and investigate their interaction with systems. The mathematical form of the model is largely adapted from literature on hydraulic pump/motor models, as a hydraulic transformer contains two rotating groups that are of similar structure to hydraulic pump/motors. The contents of this chapter provide detailed insight as to the relationship between the imposed conditions of a transformer and specific aspects its behavior, as well as the nature of the various losses that are impinged upon the machine.

The chapter begins with a complete description of the mathematical underpinnings of the model. Each equation is associated with one of two categories, mechanical and volumetric. The separation reflects whether the phenomenon under consideration impacts the mechanical power domain or the hydraulic fluid power domain, to remain consistent with hydraulic literature. Following the generalized mathematical documentation, section 2.4 describes the identification of key geometric parameters that characterize

the form of a hydraulic transformer. Section 2.5 describes a procedure for generating performance maps to show the results of the model. Lastly, section 2.6 shows how the bearing gap parameters of the transformer were tuned such that the results of the simulation matched experimental results. This model, as well as the methods for identifying parameters and generating maps described in this chapter are used for every simulation presented throughout this thesis.

2.2 Transformer Description and Modeling Approach

Figure 2.1 shows the physical architecture of the hydraulic transformer under consideration, consisting of two variable displacement axial-piston swashplate type hydraulic pump/motors connected by a common shaft. There are two fluid ports for each pump/motor, for a total of four hydraulic connection ports for the transformer. Each port is connected to one of three hydraulic lines, a line connected to a Common Pressure Rail, a line connected to a loading device, and a line connecting to the tank of the hydraulic system. To remain consistent with convention in hydraulic transformer literature, these connections will be referred to as A, B, and T respectively. An example connection is shown in figure 2.2, and a complete discussion of various connection configurations is given in chapter 2.

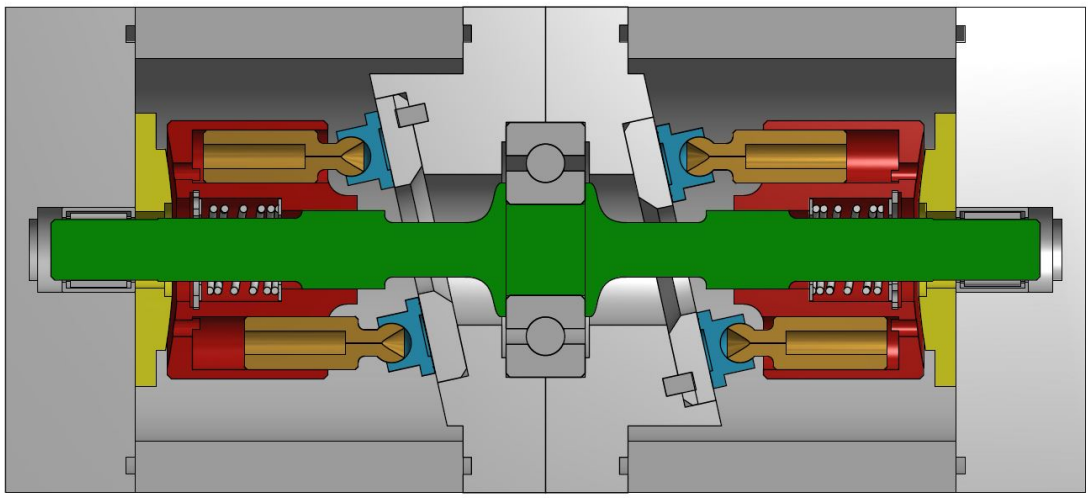

Figure 2.1: Hydraulic Transformer Architecture

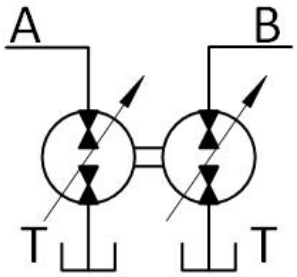

Figure 2.2: Example Hydraulic Transformer Port Connections

The hydraulic transformer was modelled with two types of dynamic states, the rotational velocity of the shaft and the pressure of the hydraulic fluid within each of the piston chambers. Convention in literature and industry groups the various components of the mathematical model into two categories, mechanical and volumetric, to reflect their contribution to either the mechanical rotational domain or the fluid power domain.

The mechanical derivations of section 2.3 will culminate in the derivation of the shafts radial acceleration term as a function of torque contributions from the pistons and all mechanical losses. The mechanical losses associated with each piston include throttling through the main piston orifice, Poiseuille and Couette friction forces within the cylinder bore, frictional losses at the reaction points between the piston and the bore, and viscous losses from relative motion between the piston shoes and the slipper plate. The forces from Poiseuille and Couette flow are a product of the motion of hydraulic fluid relative to the piston as a result of pressure differentials and motion, respectively. In addition to the summation of the piston losses, viscous losses from the relative motion of the valve plate and barrel are modelled. Viscous losses from oil churning within the case and torque losses from the roller bearings supporting the shaft are neglected due to their relatively low impact.

The volumetric analysis of section 2.3 will culminate in the derivation of a pressure dynamic term to express the rate of pressure change within each of the piston chambers. The volumetric losses associated with each piston are the leakage through the piston bore and the leakage through the piston shoes. Additionally, the leakage losses across the valve plate lands are modelled. The use of pressure dynamics in the model enable

fluid compressibility to be taken into account, increasing the accuracy of the fluid flow rate modeling beyond what a simper kinematic model would indicate.

2.3 Development of Dynamic Loss Model

Volumetric Analysis The objective of this section is to derive the $\dot{P}_{p,k}$ term that is the rate of change of fluid pressure within the piston chambers, as well as the Q_A, Q_B, and Q_T terms that are the instantaneous volumetric flow rate associated with each of the three connecting lines.

Kinematic Piston Motion Prior to deriving pressure dynamic and flow terms, it is necessary to determine the values and rates of change of several kinematic quantities of an individual piston. Deformation of the physical structure is not considered in this model, as the displacements from deformation are small relative to the size of the unit. Considering an axial piston machine such as shown in figure 2.1 and 2.3, the angular location $\varphi_{p,k}$ of the k-th piston is given by

$$\varphi_{p,k}(t) = \mod\left(\varphi(t) + (k-1)\,\frac{2\pi}{n}, 2\pi\right) \tag{2.1}$$

where n is the number of pistons in a single pump/motor unit and φ is the angular displacement of the entire group as measured by the angle of the $k = 1$ piston. The piston group and cylinder block subassembly is conventionally called a rotating group in the hydraulic industry. $\varphi_{p,k} = \pi$ corresponds to a position where the piston is fully retracted and the chamber volume is at a minimum, conventionally called top dead center. $\varphi_{p,k} = 0$ corresponds to the position where the k-th piston is fully extended such that the volume of the piston chamber is at maximum, a state conventionally called bottom dead center. These states are shown in Fig. 2.4.

Using this nomenclature for the k-th piston, the linear displacement $S_{p,k}$ of the piston with respect to top dead center is:

$$S_{p,k}(t) = R_p \tan(\alpha)\,(1 + \cos\varphi_{p,k}(t)) \tag{2.2}$$

where R_p is the radial distance of the piston center from the shaft center and α is the instantaneous swashplate angle. Taking the time derivative of the pistons linear displacement gives the linear velocity of the piston:

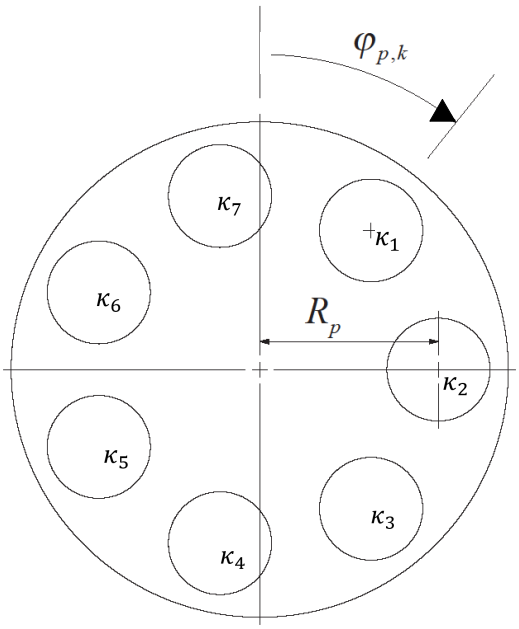

Figure 2.3: Angular Location of Piston Bores within Rotating Group

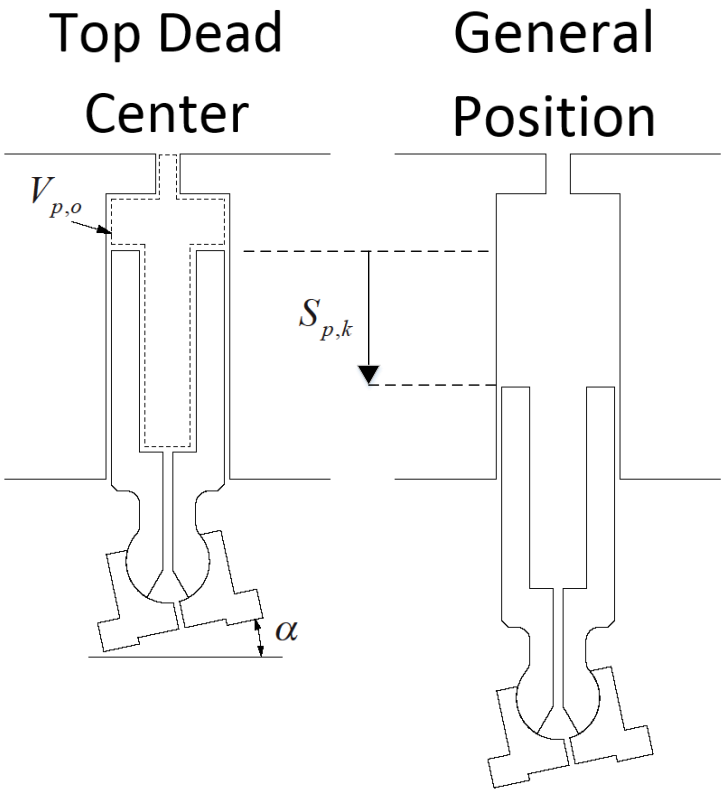

Figure 2.4: Piston Top Dead Center ($\varphi_{p,k} = \pi$) and a general position ($0 < \varphi_{p,k} < \pi$)

$$v_{p,k}(t) = \frac{dS_{p,k}(t)}{dt} = \frac{dS_{p,k}(t)}{d\varphi_{p,k}(t)}\frac{d\varphi_{p,k}(t)}{dt} = \frac{dS_{p,k}(t)}{d\varphi_{p,k}(t)}\omega(t)$$
$$= -\omega(t)R_p \tan(\alpha)\sin\left(\varphi_{p,k}(t)\right) \tag{2.3}$$

where ω is the rotational velocity of the rotating group. Summing the swept volume from the pistons linear displacement with the initial volume, the instantaneous volume of the piston chamber can be found as:

$$V_{p,k}(t) = V_{p,0} + A_p S_{p,k}(t) \tag{2.4}$$

where $V_{p,0}$ is the dead volume of the piston chamber when located at top dead center and A_p is the cross-sectional area of the piston. Multiplying the linear velocity of the piston with its cross-sectional area, the rate of change of the piston chamber volume can be obtained:

$$\dot{V}_{p,k}(t) = v_{p,k}(t)A_p = -\omega(t)R_p \tan(\alpha)\sin\left(\varphi_{p,k}(t)\right)A_p \tag{2.5}$$

Main Piston Orifice Flow Rate The bulk of the fluid transfer to and from the piston chamber occurs through an orifice in the barrel that forms a fluidic connection between the chamber and either one of the two ports associated with that rotating groups valve plate. This fluid transfer is driven by the pressure differential across the orifice, and can be modelled with a standard orifice flow rate equation:

$$Q_{p,k}(t) = C_d A_o(t)\sqrt{\frac{2|P_{p,k}(t) - P_P(t)|}{\rho}}sgn(P_{p,k}(t) - P_P(t)) \tag{2.6}$$

where $P_{p,k}$ is the instantaneous pressure within the fluid chamber, P_P is the pressure of the external port that the piston is in communication with (either the rail, load line, or tank line), C_d is a coefficient of discharge for the orifice, ρ is the density of the hydraulic oil, and A_o is the instantaneous area of the orifice. Note that table 2.1 gives the ranges at which the piston are connected to each port, for the particular configurations under consideration in the following analyses. The orifice equation assumes incompressible flow through the opening. By this declaration of the pressure difference a positive $Q_{p,k}$ represents fluid exiting the piston chamber, a convention that is held throughout this

thesis. The characteristics of the flow rate $Q_{p,k}$ during the transition between ports strongly depends on the manner in which the opening area A_o changes during the transition. Optimization of the design for discharge areas to reduce flow ripple during transition is discussed by Martin et al [23] and Wang [24]. The model implemented throughout the analysis of this paper includes triangular notches, as seen in figure 2.5. These notches, called relieving grooves or feathering, are standard practice in industry to reduce pressure spikes during transitions and enhance the rate of prepressurization of the piston chambers.

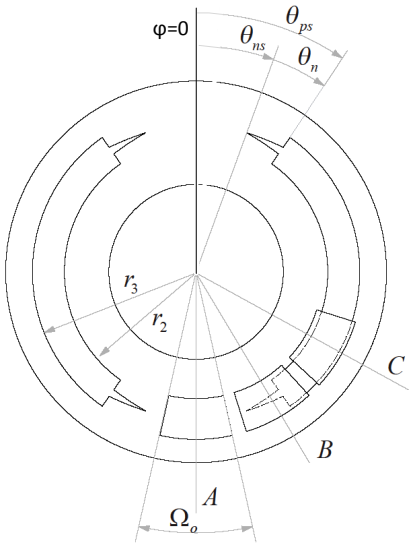

Figure 2.5: Valve plate port orifice geometry

A plot showing the variation of the orifice area during a single full revolution of a piston is given in figure 2.6, where the piston is one of seven in a $3.15cc$ pump/motor with the physical parameters listed in appendix A. The vertical lines A, B, and C correspond to the angular locations shown in figure 2.5. It can be observed that at location A there is no overlap between the piston opening and the valve plate openings, resulting in a orifice area of zero. Location B shows a transition period, and location C shows complete overlap where the maximum area possible is achieved.

The opening area of the piston is typically not a perfect circle, as it is desirable to increase the opening area as quickly as possible during operation. The opening is often

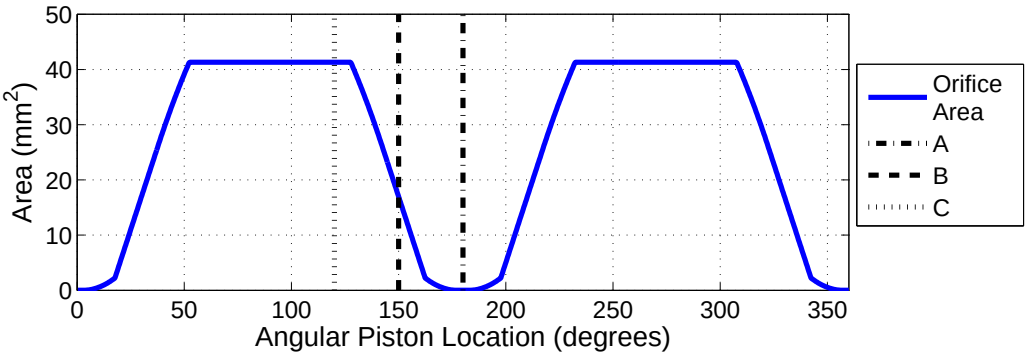

Figure 2.6: Piston orifice area over one cycle for 3.15 cc rotating group

a curved rectangular opening with rounded corners, idealized in this analysis as having perfect right-angle corners. Assuming that the angular port opening $2\Omega_o$ is greater than the angular notch size θ_n, the opening area $A_o\left(\varphi_{p,k}\right)$ can be described by the piecewise function:

$$A_o(\varphi_{p,k},t)=\begin{cases}0 & 0\le\varphi_{p,k}(t)+\frac{\Omega_o}{2}<\theta_{ns}\\ \left(\frac{\varphi_{p,k}(t)+\frac{\Omega_o}{2}-\theta_{ns}}{\theta_n}\right)^2 A_n & \theta_{ns}\le\varphi_{p,k}(t)+\frac{\Omega_o}{2}<\theta_{ps}\\ A_n+(\varphi_{p,k}(t)+\frac{\Omega_o}{2}-\theta_{ps})\beta_0 & \theta_{ps}\le\varphi_{p,k}(t)+\frac{\Omega_o}{2}<\theta_{ns}+\Omega_o\\ \left(A_n-\left(\frac{\varphi_{p,k}(t)-\frac{\Omega_o}{2}-\theta_{ns}}{\theta_n}\right)^2 A_n\right) & \\ +(\varphi_{p,k}(t)+\frac{\Omega_o}{2}-\theta_{ps})\beta_o & \theta_{ps}\le\varphi_{p,k}(t)+\frac{\Omega_o}{2}<\theta_{ps}+\Omega_o\\ \beta_o\Omega_0 & otherwise\end{cases} \tag{2.7}$$

where θ_{ns} is the angular location of the start of the feathering notch, θ_{ps} is the angular location of the start of the main section of the port opening, and θ_n is the angular size of one of the notches. A_n is the total area of one of the notches and Ω_o is the angular size of the opening in the cylinder block, as seen in figure 2.5. The term β_o is a parameter characterizing the area per unit angle of the main section of the port opening, and is given by:

$$\beta_o=\frac{\left(r_3^2-r_2^2\right)\pi}{2\pi}=\frac{\left(r_3^2-r_2^2\right)}{2} \tag{2.8}$$

where r_2 and r_3 are the inner and outer radii of the port opening in the port plate, as shown in Fig. 2.5.

Leakage Flow Rates In addition to the transmission of fluid through the main piston orifice there is also leakage out of the piston chamber along the cylinder block bore and through the hydrostatic bearings of the piston shoes. The leakage rate in the bore for an eccentrically located piston has been modeled by [25]:

$$Q_{lp,k}(t) = \frac{\pi d_p c^3 (1 + 1.5e^2)}{12 \mu L_{p,k}(t)} (P_{p,k}(t) - P_c) \tag{2.9}$$

where d_p is the diameter of the piston, c is the nominal gap size between the piston and the bore wall, P_c is the pressure of the case of the hydraulic transformer, μ is the absolute viscosity of the hydraulic fluid, and e is the eccentricity of the piston. The piston eccentricity is taken as 90% of the physical maximum ($e = 0.9 * c$) throughout this analysis to capture the experimentally observed trend that pistons loaded under pressure tend to be supported by a relatively thin hydrodynamic film approaching a mixed lubrication regime [26].

The case is assumed to be properly vented with a dedicated drain line, and therefore is considered to be at ambient pressure. A nominal clearance value of $8 \mu m$ between the piston and the cylinder block wall was used throughout this report, as it agrees with values in literature and approximately balanced the mechanical and volumetric losses through the gap across the breadth of unit sizes and operating conditions under examination ($0.4cc - 3.2cc$).

The leakage rate in the cylinder block gap of equation (2.9) is inversely proportional to the instantaneous sealing length $L_{p,k}$, which can be determined by the summation of the initial sealing length L_0 at top dead center and the linear displacement of the piston:

$$L_{p,k}(t) = L_0 - S_{p,k}(t) \tag{2.10}$$

The piston shoes are modeled as hydrostatic thrust bearings, where the leakage flow rate is derived assuming a uniform film thickness throughout and uniform pressure distribution across a given radial location [27]. For these conditions, the Reynolds

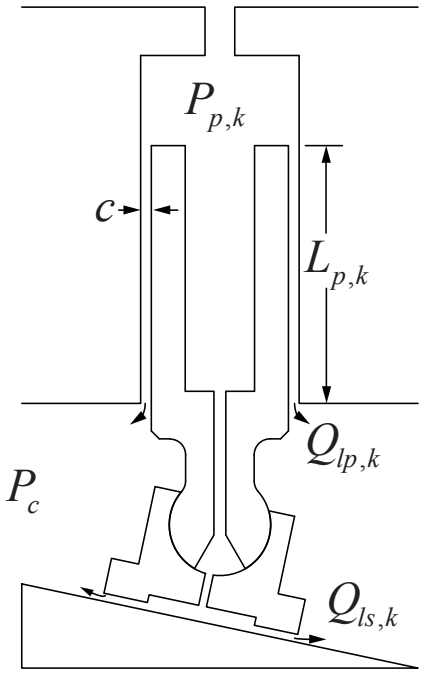

Figure 2.7: Piston Leakage Pathways

equation for the pressure distribution for any angular direction can be set up as:

$$\frac{\partial}{\partial r}\left(r\frac{\partial p}{\partial r}\right) = 0 \tag{2.11}$$

Integrating twice gives:

$$p = \bar{A}\ln r + \bar{B} \tag{2.12}$$

with boundary conditions of:

1. $p = P_{r,k}$ at $r = r_i$
2. $p = p_c = 0$ at $r = r_o$

where r_i is the inner radius of the shoe sealing land, r_o is the outer radius of the shoe sealing land, and $P_{r,k}$ is the recess pressure within the shoe cavity as seen in 2.8. Implementing the boundary conditions gives the pressure distribution across the radial length for any angular direction:

$$p(r,t) = P_{r,k}(t)\frac{\ln(r/r_0)}{\ln(r_i/r_o)} \tag{2.13}$$

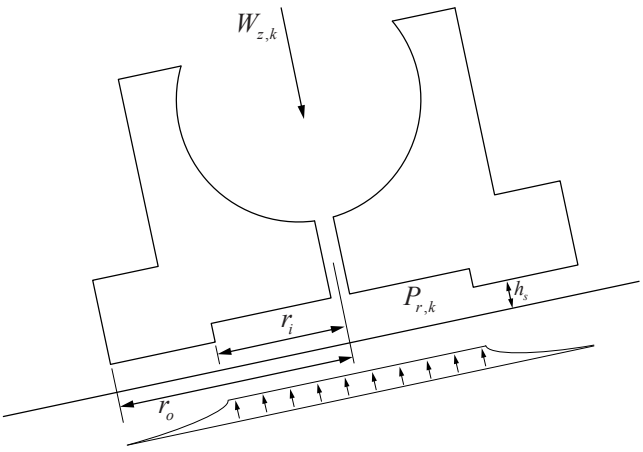

Figure 2.8: Piston Shoe Geometry

and the derivative of the pressure with respect to the radial location as:

$$\frac{\partial p}{\partial r} = \frac{P_{r,k}(t)}{r \ln(r_i/r_o)} \tag{2.14}$$

The total force generated from the pressurized fluid under the shoe slipper recess and lands can then be obtained by integrating the pressure distribution on the shoe lands and summing it with the contribution from the recess pressure:

$$W_{z,k}(t) = \pi r_i^2 P_{r,k}(t) + 2\pi \int_{r_i}^{r_o} \frac{P_{r,k}(t) \ln(r/r_o)}{\ln(r_i/r_o)} r dr \tag{2.15}$$

This can be rearranged to solve for the recess pressure necessary to support a given normal force $W_{z,k}$:

$$P_{r,k}(t) = W_{z,k}(t) \frac{2 \ln(r_o/r_i)}{\pi(r_o^2 - r_i^2)} \tag{2.16}$$

The normal force component $w_{z,k}$ was assumed to be equal to the normal reaction force between the piston shoe and swashplate, as is derived in equation (2.15).

Once the recess pressure has been determined the radial volumetric flow rate per unit circumference is given by:

$$q'_{r,k}(t) = -\frac{h_s^3}{12\mu} \frac{\partial P}{\partial r} = -\frac{h_s^3 P_{r,k}(t)}{12\mu r \ln(r_i/r_o)} \tag{2.17}$$

where h_s is the height of the gap between the shoe land and the swashplate. In absence of implementing a computationally expensive tribodynamic model for characterizing the shoe tilt [28] the gap height was taken as uniform. The assumption of uniformity would tend to underestimate leakage, as compared to a model that captured the variation in gap height that would occur in a typical duty cycle. However, the uniform gap sizes were chosen by experimentally matching loss trends as described in section 2.6, so it is assumed that this simpler model properly captures the average leakage rates as a function of loading conditions. Having obtained $q_{r,k}$ the total leakage flow through the slipper lands of a single piston can be obtained by multiplying $q_{r,k}$ by the circumference:

$$Q_{ls,k}(t) = 2\pi r q'_{r,k}(t) = \frac{\pi h_s^3 P_{r,k}(t)}{6\mu \ln(r_o/r_i)} \tag{2.18}$$

In addition to the leakage flow rates associated with individual pistons, there is also leakage associated with the valve plate of each of the rotating groups. For a uniform gap h_v between the cylinder block and the valve plate, the leakage flow from a port at pressure P_P, through the valve plate gap and into the case at pressure P_C, can be obtained by the following equation, as described in [29]:

$$Q_{lv}(t) = \frac{h_v^3}{12\mu}\left[\frac{1}{\ln(r_2/r_1) + \ln(r_4/r_3)}\right](P_P(t) - P_c) \tag{2.19}$$

where r_1, r_2, r_3,and r_4 are internal and external annuli around the valve plate as shown in figure 2.9 and P_c is the pressure of the transformer case. A more detailed approach that considers a tilted cylinder block is described in [30].

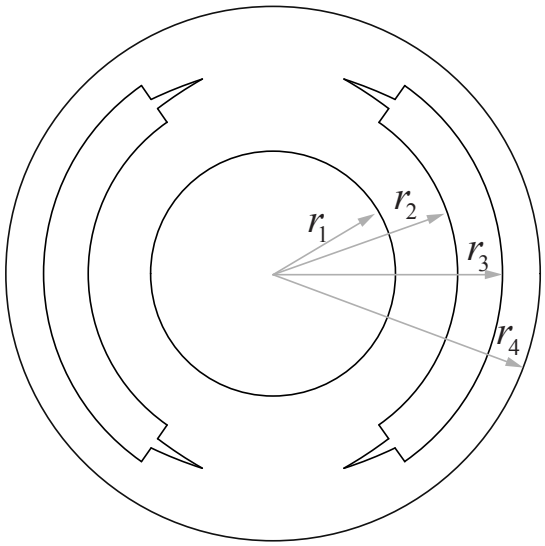

Figure 2.9: Valve Plate Geometry

Pressure dynamics Having solved for the kinematic motion of the piston and the pressure-driven flow rates associated with it, it is possible to derive the pressure dynamic term that describes the instantaneous rate of change of pressure within the piston chamber. The term can be obtained by starting from the definition of fluid bulk modulus:

$$\frac{d\rho}{\rho} = -\frac{dV}{V} = \frac{dP}{\beta(P)} \tag{2.20}$$

where ρ is the fluid density, V is the instantaneous volume of the piston chamber, and P is the fluid pressure. Taking the mass m of the fluid in the system as

$$m = \rho V \tag{2.21}$$

differentiating both sides to obtain:

$$dm = \rho dV + V d\rho \tag{2.22}$$

and then substituting in equation (2.20)

$$dm = \rho dV + \frac{V \rho dP}{\beta} \tag{2.23}$$

Taking the introduction of mass into the system as the summation of the piston orifice flow $Q_{p,k}$ (equation (2.6)), piston leakage flow $Q_{lp,k}$ (equation (2.9)), and piston shoe leakage $Q_{p,k}$ (equation (2.18)) as shown in figure 2.7, and rearranging the right side of equation (2.23) arrives at:

$$-\rho(Q_{p,k}(t) + Q_{lp,k}(t) + Q_{ls,k}(t))dt = \rho(dV + \frac{V(t)dP}{\beta(P,t)}) \tag{2.24}$$

where the ρ terms cancel out and the equation can be rearranged to solve for the pressure differential term dP:

$$dP = \frac{-\beta(P,t)}{V(t)}(dV(t) + Q_{p,k}(t) + Q_{lp,k}(t) + Q_{ls,k}(t)) \tag{2.25}$$

where volume V is the summation of the dead volume of the piston chamber $V_{p,o}$ and the volume swept by the pistons linear displacement $A_p S_{p,k}$ as given by (2.4). Replacing the generic P term with the specific term $P_{p,k}$ of the pressure under consideration, with the rate of change of the chamber volume $\dot{V}_{p,k}$ given by (2.5), representing the bulk modulus term β as being pressure dependant $\beta(P_{p,k})$ as derived by Cho in [31], and dividing both sides by dt and arrives at the rate of change of the piston chamber pressure $\dot{P}_{p,k}$:

$$\dot{P}_{p,k}(t) = \frac{-\beta(P_{p,k},t)}{V_{p,k}(t)}(\dot{V}_{p,k}(t) + Q_{p,k}(t) + Q_{lp,k}(t) + Q_{ls,k}(t)) \tag{2.26}$$

Total Unit Flow Rates A model is needed to aggregate the individual flow rates associated with each piston. The quantities of interest are the hydraulic oil flow rates

along each of the connecting lines. These are the pressure line, load line, and tank line, referred to as Q_A, Q_B, and Q_T respectively. The total flow rate to and from the transformer for each line is the summation of the contributing flow from each of the two rotating groups:

$$Q_A(t) = Q_{A,1}(t) + Q_{A,2}(t) \tag{2.27}$$

$$Q_B(t) = Q_{B,1}(t) + Q_{B,2}(t) \tag{2.28}$$

$$Q_T(t) = Q_{T,1}(t) + Q_{T,2}(t) \tag{2.29}$$

where $Q_{P,u}$ is the flow rate from the u-th unit to the P-th line. $Q_{P,u}$ is the summation of the aggregate individual piston flow rates $Q_{p,k}$ that are currently communicating with the P-th line and the leakage flow rate associated with the valve plate Q_{lv}:

$$Q_{P,u}(t) = \left[\sum_{k=1}^{n} C_P^k(\varphi_{p,k}, t) Q_{p,k}(t)\right] - Q_{lv}(t) \tag{2.30}$$

where $C_P^k(\varphi_{p,k})$ is an indicator function that has a value of unity if the k-th piston is orientated such that it is in fluid communication with the P-th line that is under consideration.

$$C_P^k(\varphi_{p,k}, t) = \begin{cases} 1 & \varphi_{p,k}(t) \in R_P^u \\ 0 & \text{else} \end{cases} \tag{2.31}$$

Table 2.1 gives the R_P^u values that indicate the ranges of the line connections for each of the three transformer unit configurations. The ranges reflect which two pressure lines bridge each of the rotating groups. For example, unit 1 is connected to the rail line A and the tank line T in both the PM-1 and PM-3 configurations, and the rail line A and the load line B in the PM-2 configuration. A full exploration of the implications of the various configurations can be found in chapter 3. A dash − indicates that the given port (A, B, or T) is not in communication with the given unit (1 or 2) at any point for that particular configuration (PM1, PM2, or PM3)

Table 2.1: Configuration Port Connections

Range	PM1	PM2	PM3
R_A^1	$[0, \pi)$	$[0, \pi)$	$[0, \pi)$
R_A^2	-	-	$[0, \pi)$
R_B^1	-	$[\pi, 2\pi)$	-
R_B^2	$[\pi, 2\pi)$	-	$[\pi, 2\pi)$
R_T^1	$[\pi, 2\pi)$	$[\pi, 2\pi)$	$[\pi, 2\pi)$
R_T^2	$[0, \pi)$	$[0, \pi)$	-

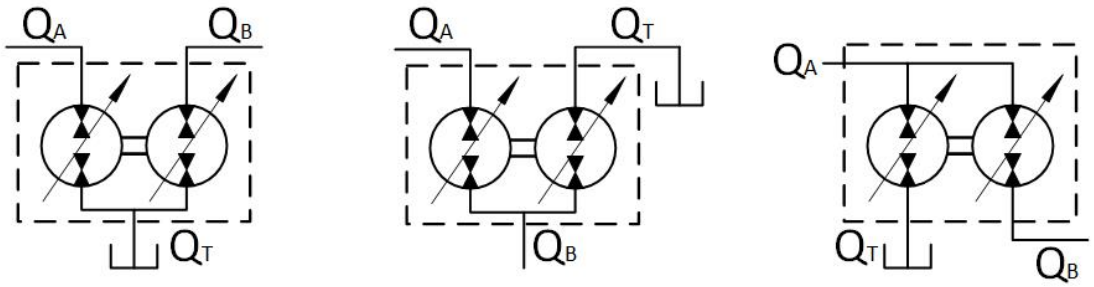

Figure 2.10: Transformer Port Connections PM-1 (Left) PM-2 (Center) PM-3 (Right)

Mechanical Analysis The objective of this section is to derive the inertial dynamics of the transformers shaft and rotating group $\dot{\omega}$. The first step is to evaluate the torque contribution of each individual piston where the losses from throttling, Poiseuille flow, Couette flow, viscous losses from relative motion between the piston shoes and the swashplate, and contact friction between the piston and the cylinder bore are all modelled. The piston torque contributions are then aggregated, and the torque losses from relative motion between the cylinder block and the valve plate are modelled. The net torque is the divided by the rotational inertia of the entire assembly to obtain the radial acceleration.

Friction Losses between Piston and Cylinder Block Bore The frictional forces within the cylinder bores of the transformer are determined using a mathematical model developed by Manring [32]. This model takes into account the tilt of the piston as prompted by the slipper reaction force and models the interaction of the piston and the cylinder bore as two point contacts, as shown in figure 2.11. The equations in this thesis are a simplified implementation of Manring's approach, as the piston is taken as having zero mass.

The reaction forces F_1 and F_2 are a function of the net force on the piston and the geometry of the piston and cylinder bore, and can be obtained through a force balance:

$$F_1(t) = \left(\frac{L_2(t)}{L_{p,k}(t)} F_{net}(t) \sin(\alpha) - \frac{d_p}{2L_{p,k}(t)} F_{net} \sin(\alpha) u_2(t) sgn(v_{p,k}(t)) \right) \frac{1}{D(t)} \tag{2.32}$$

$$F_2(t) = \left(\frac{L_2(t) + L_{p,k}(t)}{L_{p,k}(t)} F_{net}(t) \sin(\alpha) - \frac{d_p}{2L_{p,k}(t)} F_{net}(t) \sin(\alpha) u_1(t) sgn(v_{p,k}(t)) \right) \frac{1}{D(t)} \tag{2.33}$$

where

$$\begin{aligned} D(t) = & \cos(\alpha) + \frac{d_p}{L_{p,k}(t)} u_1(t) u_2(t) \sin(\alpha) \\ & - \left(\frac{d_p}{2L_{p,k}(t)} (u_1(t) - u_2(t)) \cos(\alpha) \right) sgn(v_{p,k}(t)) \\ & - \left(u_2(t) \sin(\alpha) + \frac{L_2(t)}{L_{p,k}(t)} (u_1(t) - u_2(t)) \sin(\alpha) \right) sgn(v_{p,k}(t)) \end{aligned} \tag{2.34}$$

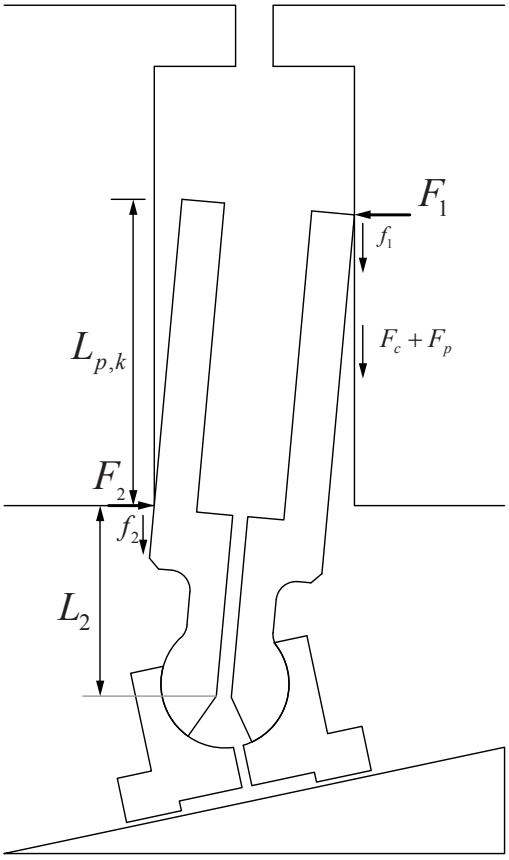

Figure 2.11: Piston Forces

where u_1 and u_2 are the coefficients of friction at the contact points, the determination of which is shown below in equation (2.37) and equation (2.38).

F_{net} is the net force aligned with the piston major axis, and is given by equation (2.35), where viscous forces from Couette and Poiseuille flows are derived in equations (2.45) through (2.52). The pressure force from the fluid in the piston chamber is assumed to be applied normal to the piston face it is in communication with, and as a simplifying assumption the viscous forces from the Couette and Poiseuille flows are applied as distributed forces normal to the piston face. The piston was taken as having zero mass.

$$F_{net}(t) = A_p P_{p,k}(t) + F_c(t) + F_p(t) \tag{2.35}$$

L_2 is the distance from the plane of the face of the cylinder block to the center of the piston shoe ball joint, given by:

$$L_2(t) = L_{p,0} - L_{p,k}(t) \tag{2.36}$$

where $L_{p,0}$ is the distance from the plane of the end of the piston to the center of the piston shoe ball joint.

Coefficient of friction calculation The coefficient of friction at the contact points is determined by modeling the Stribeck curve. The Stribeck curve characterizes the variation in the coefficient of friction between two lubricated sliding surfaces. The three zones of the curve are boundary lubrication, mixed lubrication, and hydrodynamic lubrication. For a complete discussion of the following derivation, see Manring [32].

The coefficients of friction u_1 and u_2 are determined by equations (2.37) and (2.38), which captures the tendency of the wedge shaped gap created by a tilted piston in motion to generate a hydrodynamic lifting force.

$$u_1(t) = \begin{cases} \hat{u} \exp\left(-\left(\frac{2L_{p,k}(t)\sqrt{6K^*(t)}}{h^*} \right)^2 \frac{\mu v_{p,k}(t)}{(F_1(t)/d)} \right) + \frac{\sqrt{\frac{\mu v_{p,k}(t)}{(F_1(t)/d)}}}{\sqrt{6K(t)}} & v_{p,k}(t) > 0 \\ \hat{u} & v_{p,k}(t) \leq 0 \end{cases} \tag{2.37}$$

$$u_2(t) = \begin{cases} \hat{u} & v_{p,k}(t) \geq 0 \\ \hat{u} \exp\left(\left(\frac{2L_{p,k}(t)\sqrt{6K^*(t)}}{h^*} \right)^2 \frac{\mu v_{p,k}(t)}{(F_2(t)/d)} \right) + \frac{\sqrt{\frac{-\mu v_{p,k}(t)}{(F_2(t)/d)}}}{\sqrt{6K(t)}} & v_{p,k}(t) < 0 \end{cases} \tag{2.38}$$

h^* is the critical fluid-film thickness at which the transition between mixed and hydrodynamic lubrication occurs. h^* is given by

$$h^* = 3\sqrt{R_a^2 + R_b^2} \tag{2.39}$$

where R_a and R_b are RMS surface roughness of the piston and bore. h^* is taken as 2.47 μm, as given by Manring, which equates to R_a and R_b values of approximately 0.58 μm. The terms K and ζ are both fluid-film thickness parameters, and K^* is the term K evaluated when $h_{min} = h^*$.

$$K(t) = \frac{2(2 - \zeta(t)) + \zeta(t)\ln(\zeta(t) - 1)}{\zeta(t)(\zeta(t) - 2)^2} \tag{2.40}$$

$$\zeta(t) = \frac{h_{max}}{h_{min}(t)} + 1 \tag{2.41}$$

h_{min} and h_{max} are the minimum and maximum gap heights along the length of the tilted piston. h_{max} is taken to be twice the nominal clearance within the bore to capture the absence of hydrodynamic lifting on the opposite side of the piston, and the minimum fluid film thickness can be determined for a particular piston velocity $v_{p,k}$ and loading condition W by:

$$h_{min}(t) = l\sqrt{6K\frac{\mu v_{p,k}}{W(t)}} \tag{2.42}$$

Having determined coefficients of friction u_1 and u_2 in equations (2.37) and (2.38), normal contact forces F_1 and F_2 in equations (2.32) and (2.33), and piston velocity $v_{p,k}$ in (2.3), the frictional forces can be determined by

$$f_1(t) = F_1(t)u_1(t)sgn(v_{p,k}(t)) \tag{2.43}$$

$$f_2(t) = F_2(t)u_2(t)sgn(v_{p,k}(t)) \tag{2.44}$$

Couette Viscous Shearing Derivation The motion of the piston relative to the cylinder bore generates a shearing viscous force, which can be approximated with the well-known Couette flow equations for shear-driven fluid motion between parallel plates. To maintain consistency with the previous assumption of an eccentric piston, Couette shear friction was also modelled for an eccentric piston as derived by Duan and Nielsen [33].

For eccentricity values as small as those found in hydraulic pistons, the actual local clearance c_e due to the eccentricity e as a function of the angular position ϕ on the piston can be approximated by:

$$c_e(\phi) = c + e\cos(\phi) \tag{2.45}$$

where c is the nominal clearance of the piston bore. Assuming unidirectional flow along the axial piston direct, no-slip boundary conditions for both the piston and the cylinder bore, and a linear velocity profile within the fluid, the fluid velocity component v_c from Couette flow can be determined using:

$$v_c(\phi, t) = v_{p,k}(t)\left(1 - \frac{y}{c_e(\phi)}\right) \tag{2.46}$$

where $v_{p,k}$ is the piston velocity and $\in (0, c_e)$. From Newtons law of viscous flow for fluids with a dynamic viscosity of μ, the local shear stress τ can be obtained by:

$$\tau_c(\phi, y, t) = -\mu\frac{dv_c}{dy} = \mu\frac{v_{p,k}(t)}{c + e\cos(\phi)} \tag{2.47}$$

Integrating τ_c across the entire area of overlap between the piston and cylinder bore obtains the Couette drag force:

$$\begin{aligned} F_c(t) = \int_0^{2\pi}\int_0^{L_{p,k}(t)} \frac{\mu v_{p,k}(t)}{c + e\cos\phi} dz d\phi \\ &= v_{p,k}(t)L_{p,k}(t)\mu d_p \int_0^{2\pi} \frac{1}{c + e\cos\phi} d\phi \\ &= \frac{v_{p,k}(t)L_{p,k}(t)\mu d_p \pi}{\sqrt{c^2 - e^2}} \end{aligned} \tag{2.48}$$

Poiseuille Viscous Shearing Derivation The pressure difference across the piston causes fluid to flow through the clearance gap between a piston and the cylinder

bore. This generates a viscous shearing force in the direction of fluid motion. Assuming laminar flow of an incompressible Newtonian fluid, the fluid velocity can be determined by

$$v_f(t) = -\frac{1}{2\mu}(c_e - y)y\frac{dP(t)}{dz} \tag{2.49}$$

where the rate of pressure drop $\frac{dP}{dz}$ is taken as constant along the axial length of the piston clearance:

$$\frac{dP(t)}{dz} = -\frac{P_{p,k}(t) - P_c}{L_{p,k}(t)} \tag{2.50}$$

Combining equation (2.49) and equation (2.50) with Newtons law of viscous flow, the local shear stress from Poiseuille flow can be obtained:

$$\tau_f(\phi, y, t) = \mu\frac{dv_f(t)}{dy} = \mu\left[\frac{P_{p,k}(t) - P_c}{2\mu L_{p,k}(t)}(c + e\cos(\phi) - 2y)\right] \tag{2.51}$$

where $y \in (0, c_e)$ and $\phi \in (0, 2\pi)$. Evaluating the shear stress τ_f at the piston surface, where $y = 0$ along the piston length $L_{p,k}$ arrives at the shearing viscous force from poiseuille flow:

$$\begin{aligned} F_p(t) &= 2\int_0^{\pi}\int_0^{L_{p,k}(t)} \frac{P_{p,k}(t) - P_c}{2L_{p,k}(t)}(c + e\cos(\varphi) - 2y)r_p dz d\varphi \\ &= \int_0^{\pi}(P_{p,k}(t) - P_c)(c + e\cos(\varphi))r_p d\varphi \\ &= (P_{p,k}(t) - P_c)r_p\int_0^{\pi}(c + e\cos(\varphi))d\varphi \\ &= (P_{p,k}(t) - P_c)r_p\pi c \end{aligned} \tag{2.52}$$

Piston Shoe Viscous Friction The relative motion between the sealing lands of the piston shoes and the swashplate generates a viscous shearing force. The exact nature of the elastrohydrodynamic lubrication within the bearing gap is not well understood and is currently an active area of research, however several numerical studies have indicated that a properly designed piston shoe will be fully supported on a fluid film without transition to mixed lubrication [34, 35]. Therefore this model assumes full

boundary lubrication where losses are entirely viscous shearing and are dependent on velocity, fluid viscosity, and the gap height.

The gap heights used in the shoe model were identified by the process described in section 2.6. The values ranged between $9.1\mu m$ and $13.8\mu m$, which agrees with gap sizes found in both numerical and experimental investigations in literature [35, 28].

The friction from compressive forces in the ball joints connecting the pistons and their shoes tends to prevent relative motion between the pistons and their shoes during steady state operation [26]. Therefore, as both the swashplate angle and the corresponding tilt angle of the shoe are fixed during steady state operation, the global angular orientation of the piston and shoe assemble is fully constrained and does not change as a function of its current angular position $\varphi_{p,k}$. The resulting motion of the piston shoe can be described as a combination of rotation around the shaft and rotation around the piston center, as shown in figure 2.12. Figure 2.13 shows a sample set of both velocity components as well as the total velocity vector as they would be dispersed on a shoe for a 3.15 cc rotating group piston.

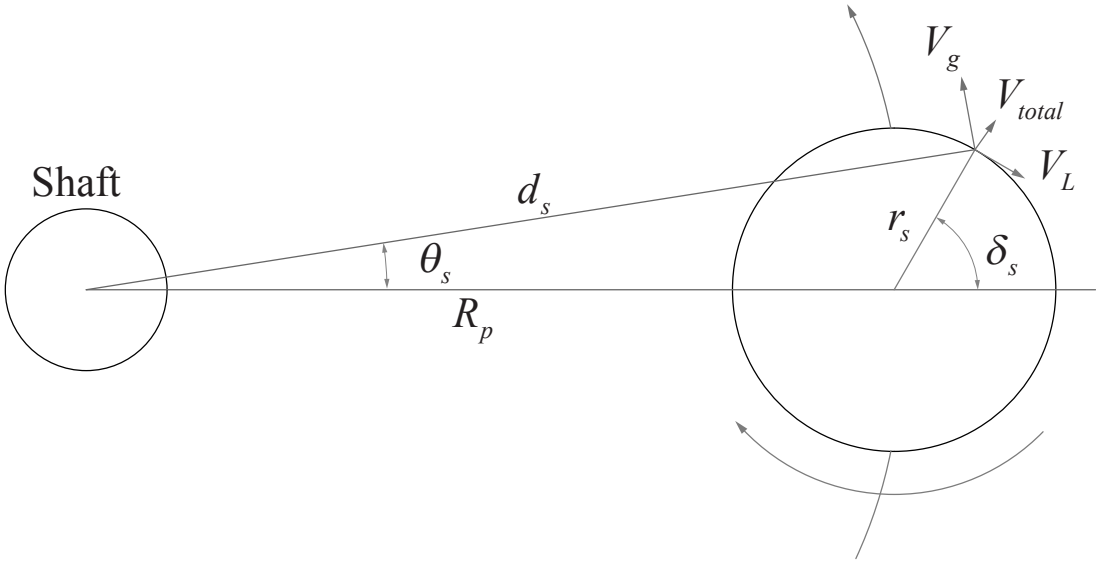

Figure 2.12: Piston Shoe Velocity Components

The instantaneous velocity magnitude from the shaft rotation v_1 and direction $v_{1\theta}$ can be obtained for an infinitesimal point on the shoe through geometrical considerations

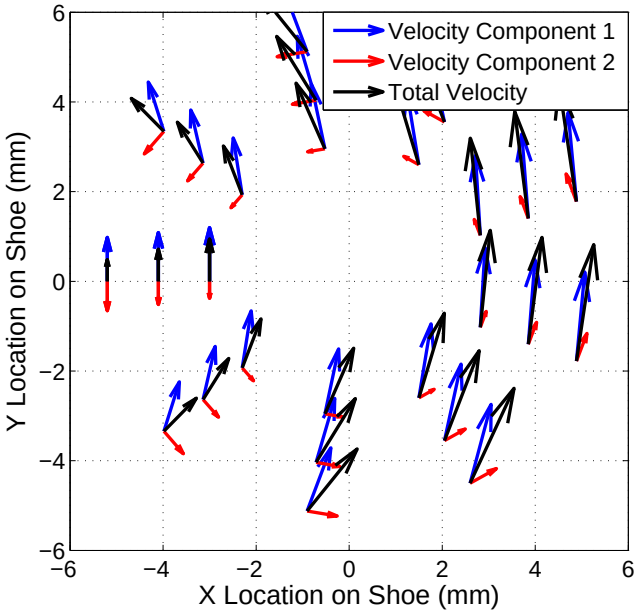

Figure 2.13: Piston Shoe Velocity Vectors

as:

$$\begin{aligned} v_1(t) &= d_s\omega(t) \\ v_{1\theta}(t) &= \theta_s(t) - \frac{\pi}{2} \end{aligned} \tag{2.53}$$

where d_s and θ_s characterize the location of the infinitesimal point as shown in figure 2.12 and are given by:

$$d_s(t) = \sqrt{R_p^2 + r_s^2 - 2R_p r_s \cos(\pi - \delta_s(t))} \tag{2.54}$$

$$\theta_s(t) = \sin^{-1}\left(r_s \sin\left(\frac{\pi - \delta_s(t)}{d_s}\right)\right) \tag{2.55}$$

The instantaneous velocity magnitude from rotation around the piston center v_2 and direction $v_{2\theta}$ can be obtained for the same infinitesimal point on the shoe through geometrical considerations as:

$$v_2(t) = r_s\omega(t)$$
$$v_{2\theta}(t) = \theta_s(t) + \pi \tag{2.56}$$

The total for the x-component v_x can be obtained by summing x-component contributions of both their velocity component terms. The process can be repeated for the y-component:

$$v_x(t) = v_1(t)\cos(v_{1\theta}(t)) + v_2(t)\cos(v_{2\theta}(t))$$
$$v_y(t) = v_1(t)\sin(v_{1\theta}(t)) + v_2(t)\sin(v_{2\theta}(t)) \tag{2.57}$$

From this, the total velocity magnitude at the given infinitesimal point follows:

$$v_s(t) = \sqrt{v_x^2(t) + v_y^2(t)} \tag{2.58}$$

Having obtained the velocity magnitude the shearing stress can be obtained as:

$$\tau_s(t) = \mu\frac{1}{h_s}v_s(t) \tag{2.59}$$

Using the relationship between power in the linear mechanical domain and the rotational mechanical domain:

$$\tau_s(t)v_s(t) = \frac{dT_s}{dA}\omega(t) \tag{2.60}$$

where dA is the area of the infinitesimal point under consideration. The values can be rearranged to solve for torque T_s, and then integrated over the entire area of the shoe sealing land to obtain the total torque exerted by the k-th piston on the transformer:

$$T_{s,k}(t) = \int_{r_i}^{r_o}\int_0^{2\pi}\tau_s(t)v_s(t)\frac{1}{\omega(t)}d\delta_s dr_s \tag{2.61}$$

Valve plate viscous friction losses Similarly to the piston shoes, the behavior of the elastrohydrodynamic lubrication within the bearing gap between the valve plate and the cylinder block is not well understood. Current state of the art research uses dedicated numerical models to consider some of the impacts of thermal deformation, elastic

deformations, micromotion, fluid property changes, hydrodynamic pressure forces, surface roughness, and wear patterns [36] within the gap, however it is often necessary to neglect some of the factors for the sake of model complexity and estimates of average gap heights vary significantly across literature. Estimations range from $2\mu m$ from numerical modeling [35] to $40\mu m$ in experimental trials [37]. All research indicates that the cylinder block will tilt relative to the valve plate.

This model assumed full boundary lubrication with a constant average gap height. The average gap heights used varied from $8\mu m$ to $20\mu m$ depending on the maximum displacement of the rotating group being modeled, which agrees with values observed in literature through both numerical simulations and experimental studies. The process by which the average gap heights were obtained is described in section 2.6.

The cylinder block tilt fraction σ is the fraction by which the local gap height deviates from the average gap height as compared to the maximum deviation physically possible if the edge of the cylinder block was in contact with the port plate. Experimental studies have observed tilt fractions varying between 0.35 and 0.82 [37] depending on the design of the valve plate and the current loading conditions. For all simulations in this thesis the cylinder block tilt fraction was assumed constant at 0.7, as an approximate average of the observed experimental values.

Taking into account the tilt, the local valve plate gap height $h_{v,l}$ can be obtained by:

$$h_{v,l} = h_v + r_v \sin\left(tan^{-1}\left(\sigma\frac{h_v}{r_4}\right)\right)\cos(\theta_v) \tag{2.62}$$

The local shear stress can be found through viscous shearing:

$$\tau_v(t) = \mu v_v(t)\frac{1}{h_{v,l}} = \mu\omega(t)r\frac{1}{h_{v,l}} \tag{2.63}$$

And the total torque from the valve plate can be obtained by integrating the torque contribution from the viscous shearing:

$$T_v(t) = \int_{r_1}^{r_2}\int_0^{2\pi}\tau_v(t)rd\theta dr = \int_{r_1}^{r_2}\int_0^{2\pi}\mu\omega(t)r^2\frac{1}{h_{v,l}}d\theta dr \tag{2.64}$$

Net torque and rotational speed dynamics Using the normal component of the net forces $(F_2 - F_1)$ exerted by a piston on the cylinder block and subtracting the

viscous torque losses from the shoes $T_{s,k}$, it is possible to obtain the torque contribution from each individual piston:

$$T_{p,k}(t) = (F_2(t) - F_1(t)) \sin(\varphi_{p,k}(t)) - T_{s,k}(t) \tag{2.65}$$

where F_1 and F_2 are given by Eq. (2.32) and Eq. (2.33) and $T_{s,k}$ is given by Eq. (2.61).

Summing the contributions across all of the pistons within a rotating group and applying the viscous torque losses from the valve plate, the total torque of the u-th rotating group T_u is obtained:

$$T_u(t) = \left[\sum_{k_1=1}^{n} T_{p,k}(t) \right] + T_v(t) \tag{2.66}$$

The rotational acceleration can then be determined, where J is the total rotational inertia of the rotating components with respect to the axis of the transformer shaft:

$$J\dot{\omega}_s(t) = T_1(t) + T_2(t) \tag{2.67}$$

2.4 Parameter Scaling

The results of the dynamic loss model described in the preceding section are strongly dependent on the geometrical parameters put into it. Therefore, since the objective of these studies are to explore the performance of a transformer with typical parameters within a system, it is necessary to have reasonable input parameters. Where possible, direct measurements of the parameters of existing hydraulic pumps and motors are made and used as inputs to the model.

When a study requires the analysis of units through a range of maximum displacements, it becomes necessary to develop scaling laws to relate each of the individual geometrical parameters to the maximum displacement of the unit. In order to enable the optimization procedures of the humanoid robot case studies of chapter 5 and 6, such scaling laws were developed for a range of hydraulic pump/motor maximum displacements.

A set of five scaling laws were developed by measuring the geometrical parameters of four Takako Micro Pumps with maximum displacements of 0.4 cc, 0.8 cc, 1.6 cc, and 3.15 cc. The parameters measured were the radial distance of the center piston from the center of the shaft R_p, the diameter of a piston d_p, the inner radius of the shoe land r_i, the outer radius of the shoe land r_o, and the distance from the plane of the end of a piston to the center of the shoe ball joint $L_{p,0}$. How these parameters depend on the maximum displacements were obtained through curve fittings. Linear or polynomial equations were used as the shapes dictated, as shown in figure 2.15. The measured values are tabulated in appendix B.

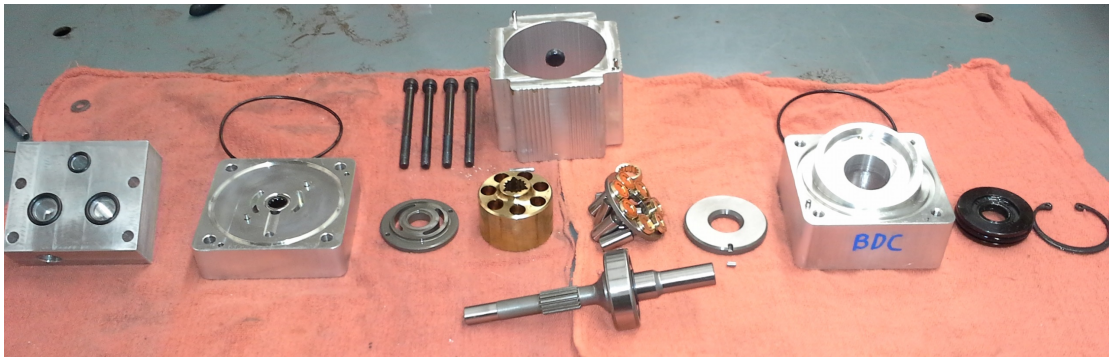

Figure 2.14: Takako 3.15 cc Micro Pump disassembled for parameter measurements

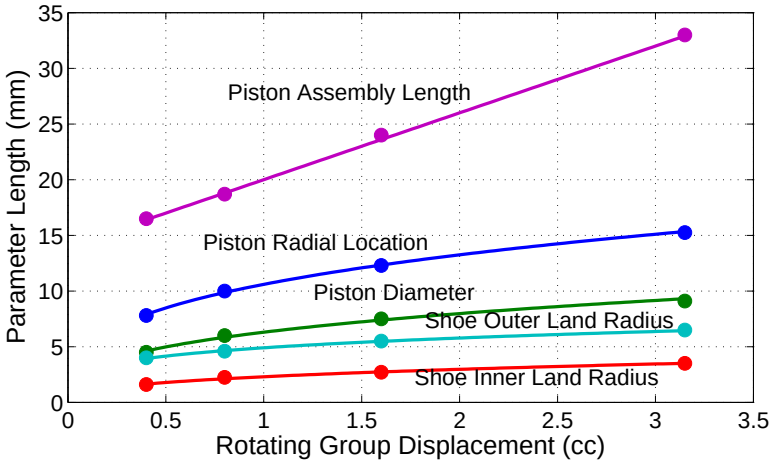

Figure 2.15: Geometrical parameter scaling laws

The scaling laws for the five measured parameters are:

$$\begin{aligned} R_p &= 0.0106 D_{max}^{.322} \\ d_p &= 0.0063 D_{max}^{.34} \\ r_i &= 0.0023 D_{max}^{.368} \\ r_o &= 0.0049 D_{max}^{.238} \\ L_{p,0} &= 0.006 D_{max} + 0.014 \end{aligned} \tag{2.68}$$

where D_{max} is the maximum displacement of the rotating group in cc/rev. It should be noted that these equations were generated from a range of $D_{max} \in (0.4cc, 3.15cc)$. It is likely that the trend would continue beyond the bounds, but the claim is unverified. Any results generated by a model utilizing parameters generated by these scaling laws outside of their bounds should be interpreted with an appropriately higher degree of uncertainty.

2.5 Map Generating Procedure

Efficiency maps are used throughout this thesis to characterize the performance of systems throughout their entire operating regions. They can be used to observe efficiency trends, visualize the boundaries of the operating region, and interpolate data between simulated points. This section describes the procedure, assumptions, and interpolation rules that have been used to generate such maps.

In order to generate performance maps, it is necessary to establish a rule for how a transformer system will achieve a given operating point. The rule used in this thesis was derived from an understanding of the typical relationship between fractional displacement of a hydraulic pump/motor and its efficiency.

If the operating point of a hydraulic pump/motor is considered to be characterized by the output pressure and flow rate or output torque and rotational velocity, then the output power for a given point is fixed. As the majority of mechanical losses within the hydraulic machine are viscous losses, the magnitude of mechanical losses tends to increase with speed. Therefore, as a unit operating at a smaller displacement generally must rotate faster to achieve a given output flow, there is a well-known trend that for

a given operating point the efficiency of a variable displacement hydraulic pump/motor monotonically increases as the fractional displacement of the unit increases. An example of this trend is shown in figure 2.16, where the efficiency of a 3.15 cc pump generating 30 cc/s of output flow at 20 MPa was simulated for the full range of its fractional displacement values using the loss model described in this chapter. In the simulation used to generate figure 2.16, the speed necessary to achieve the 30 cc/s of output flow was imposed for each fractional displacement. Therefore, the speed is not constant. It can be seen that the efficiency monotonically increases to a maximum at full displacement.

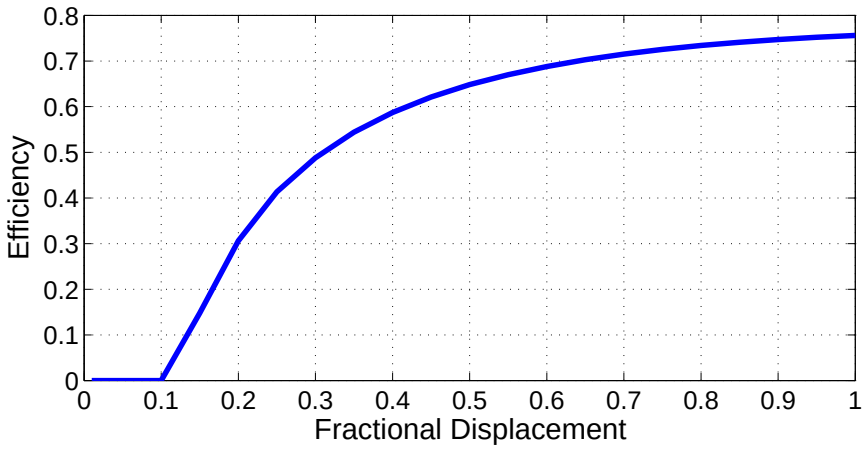

Figure 2.16: Impact of fractional displacement on the efficiency of a 3.15 cc pump

Although this trend is valid for a significant fraction of the operating region of a typical hydraulic pump/motor, it is important to note that there is a region where it would not hold. For a low flow operating point a unit at full displacement would need to operate at a correspondingly slow speed. If the speed was low enough, there would be insufficient hydrodynamic pressures built up to achieve full boundary lubrication within the bearing gaps of the machine, resulting in mixed lubrication operation with correspondingly excessive mechanical losses. For such an operating point, it would likely be more efficient to operate at a lower fractional displacement that requires higher speeds, avoiding the mixed lubrication regime.

Accurately capturing the transition point into the mixed lubrication regime requires a high fidelity numerical model that considers surface roughness, thermal deformation,

wear patterns, elastic deformation, elastohydrodynamic effects, and micromotion of the individual machine elements [36]. Such a model was not built or utilized for the studies of this thesis, and therefore the transition to mixed lubrication and corresponding violation of the trend of figure 2.16 was neglected.

Proceeding under the assumption that operating a hydraulic pump/motor at larger fractional displacements leads to higher efficiencies, it was assumed that it would be more efficient to operate a hydraulic transformer such that the displacements of its rotating groups would be as large as possible for the given operating point. Figure 2.17 shows the relationship between the efficiency and the fractional displacements of the units for a particular operating point. The plot shows the efficiency of a transformer consisting of two 3.15 cc units operating off of a 20 MPa rail maintaining an output pressure of 15 MPa and output flow rate of 100 cc/s where the fractional displacement of the second unit is varied from 0.2 to 1 and the fractional displacement of the first unit is varied such that the desired operating condition is achieved. The maximum efficiency was observed when the fractional displacements of the two rotating groups was largest, achieved by having one of the rotating groups at full displacement and adjusting the other to achieve the desired behavior.

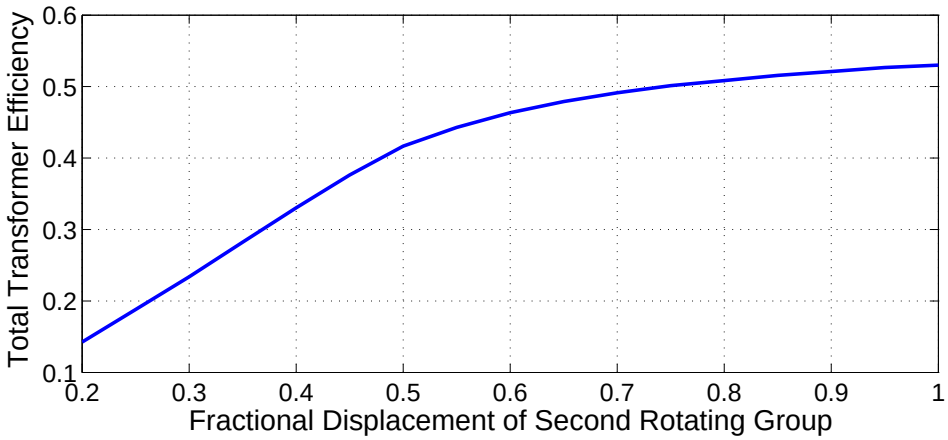

Figure 2.17: Total transformer efficiency as a function of the fractional displacement of the 2nd unit, where the pressure ratio is fixed at 0.75 and output flow rate is fixed at 100 cc/s

From this behavior, the rule used to dictate how a transformer would achieve a given

operating point was derived. The rule was that either one of the two units would always be operating at maximum displacement, and the other would be operating at whatever displacement was necessary to achieve the desired operating point. This rule assumes that it is always most efficient for a transformer to operate at as large of displacements as possible. As mentioned above, this neglects the fact that this trend is likely to be violated at sufficiently low flow rate operating conditions. Additionally, it is also possible that either the rotational speed of the transformer or the displacement of the rotating groups would be of importance during transient events where the quality of trajectory tracking capabilities could supersede efficiency performance. It is acknowledged that although the stated rule is sufficient for investigating steady state efficiency performance as undertaken in this thesis, an advanced transformer controller would likely occasionally deviate from it in order to improve demand tracking performance.

The stated rule was used in the generation of performance maps showing the steady state efficiencies and operating regions. The operating point of a transformer was always considered to be characterized by output flow rate and pressure in this thesis. The efficiency was defined as the ratio of net output power to net input power, where the power streams considered varied depending on whether the performance of the transformer itself or the system as a whole was being characterized. A complete discussion of the difference between unit and system efficiency and derivation of the corresponding equations can be found in section 3.3 and 3.4 respectively.

An example map is shown in figure 2.18. All of the maps shown in this thesis are generated in the manner described in this section. The grid of points shows the approximate distribution and density of discrete operating points at which data was collected. Data was collected either through the simulation model described in section 2.3 or through an experimental test bench on a prototype unit. The spaces between the discrete sampled points was filled in using 2D linear interpolation.

Points were generated for the entire possible operating range, considering the specified constraints of the transformer. Throughout this thesis the transformer was considered to have a maximum allowable shaft speed of 30 Hz and a maximum allowable pressure of 40 MPa. Code was written to automatically identifying the right-most point in each horizontal row of points, and remove interpolated data to the right of the boundary formed by connecting each of the right-most points. This was necessary, as

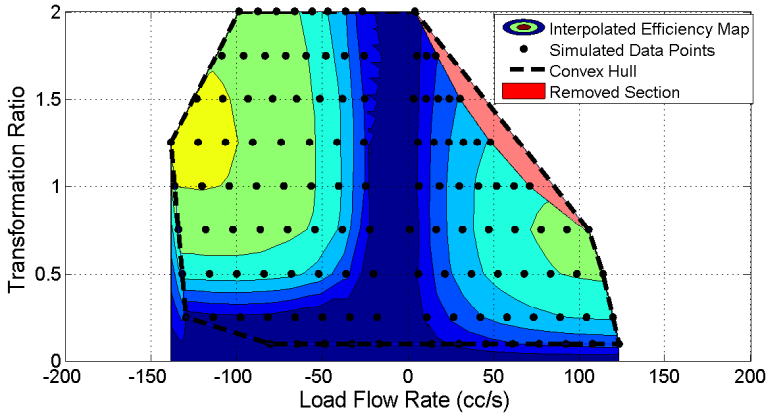

Figure 2.18: Example point dispersion and convex hull of map generating procedure

the initial process of interpolation filled in the entire convex hull of the discrete points, which would result in an incorrect operating boundary whenever the actual boundary was concave, as it tended to be on the right side of the boundary.

2.6 Experimental Parameter Identification

Bearing gap sizing through experimentation The sizes of the bearing gaps of the piston shoes and cylinder blocks are parameters that must be identified for a simulation, in the same manner as the parameters discussed in section 2.4. However, since the bearing gaps are generated in part by hydrodynamic forces during operation, they could not be directly measured by the equipment available for this investigation. Models exist in literature that can produce numerical results for gap sizes, such as a tribodynamic model by Lin [28] or the CASPAR tool under development by MaHa labs at Purdue [38], but their complexity and computationally expense exceed the allowance of this study.

The approach taken for this thesis was to identify reasonable gap sizes by comparing simulated performance results against actual experimental results of both an instrumented prototype hydraulic transformer and a smaller pump/motor unit. There were two parameters being tuned, the piston shoe gap h_s and the cylinder block gap h_v. The fitness of a particular pair of gap heights was assessed by its performance

in terms of how well the corresponding simulation matched the experimental data in two areas: Peak unit efficiency and general efficiency trends across the entire operating region. The tuned values were identified by exploring the simulated performance of transformers with gap pairs within the design space of shoe gap heights $h_s \in (2, 20)\ \mu m$ and valve plate gap heights $h_v \in (4, 40)\ \mu m$, where the ranges were determined by the maximum and minimum values found in literature.

Bearing Gap Behavior Assumption The piston shoe and cylinder block gaps were considered to be constant for a unit of a given size, independent of the local pressure or operating speed. This is a simplification, as both experimental [37] and numerical studies [28, 39] indicate that gap sizes fluctuate depending on the instantaneous local conditions of the bearing surfaces under consideration. The values given should therefore be interpreted as near-average values that capture the average magnitudes and trends of the losses associated with the gaps during steady state operation, and not accurate depictions of actual instantaneous behavior throughout the entire cycle.

Experimental results for 3.15 cc transformer Figure 2.19 shows the experimentally determined efficiency maps for the three unit configurations of the prototype hydraulic transformer used for this tuning effort. The maps shown are the standard against which the simulated results were compared. The efficiency shown is the ratio of total fluid power exiting the transformer to the total fluid power entering the transformer. A complete discussion of the transformer configurations and efficiency definitions are given in chapter 3. The transformer consisted of two rotating groups both with a maximum displacement of 3.15 cc and the tests were performed off of a 10.35 MPa [1500 PSI] pressure rail.

Gap Tuning Results for 3.15 cc simulated transformer Figure 2.20 shows the simulated efficiency maps for a pair of untuned gap heights. The values chosen were a shoe and valve plate gap height of 5 μm, which was taken as an arbitrary starting point near the smaller end of values observed in literature.

Comparing the untuned maps of figure 2.20 against the experimental maps of figure 2.19, several key discrepancies can be observed. First, there is a trend towards increasing efficiency as the load flow rate increases in the experimental maps, but the opposite is observed in the untuned simulation maps. For example, in the mode 1 section of the untuned figure 2.20 the region of highest efficiency for a transformation ratio of 1 is at

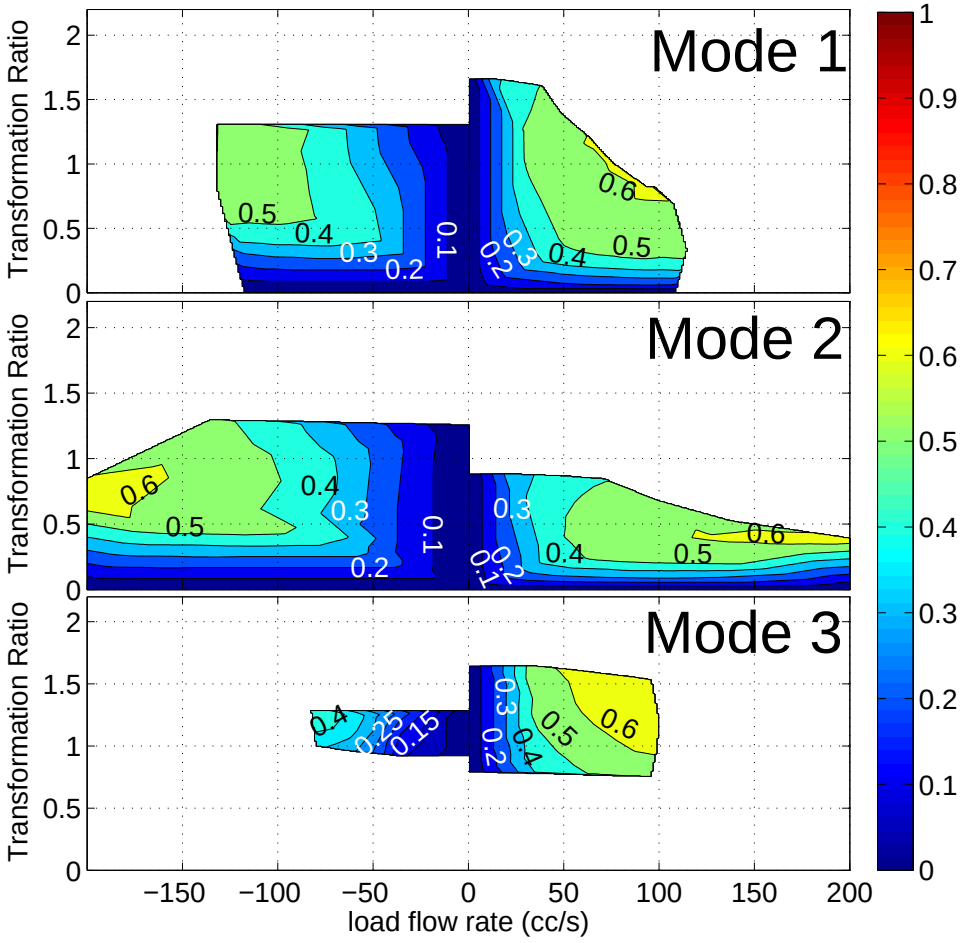

Figure 2.19: Experimental Efficiency Maps of Prototype Transformer

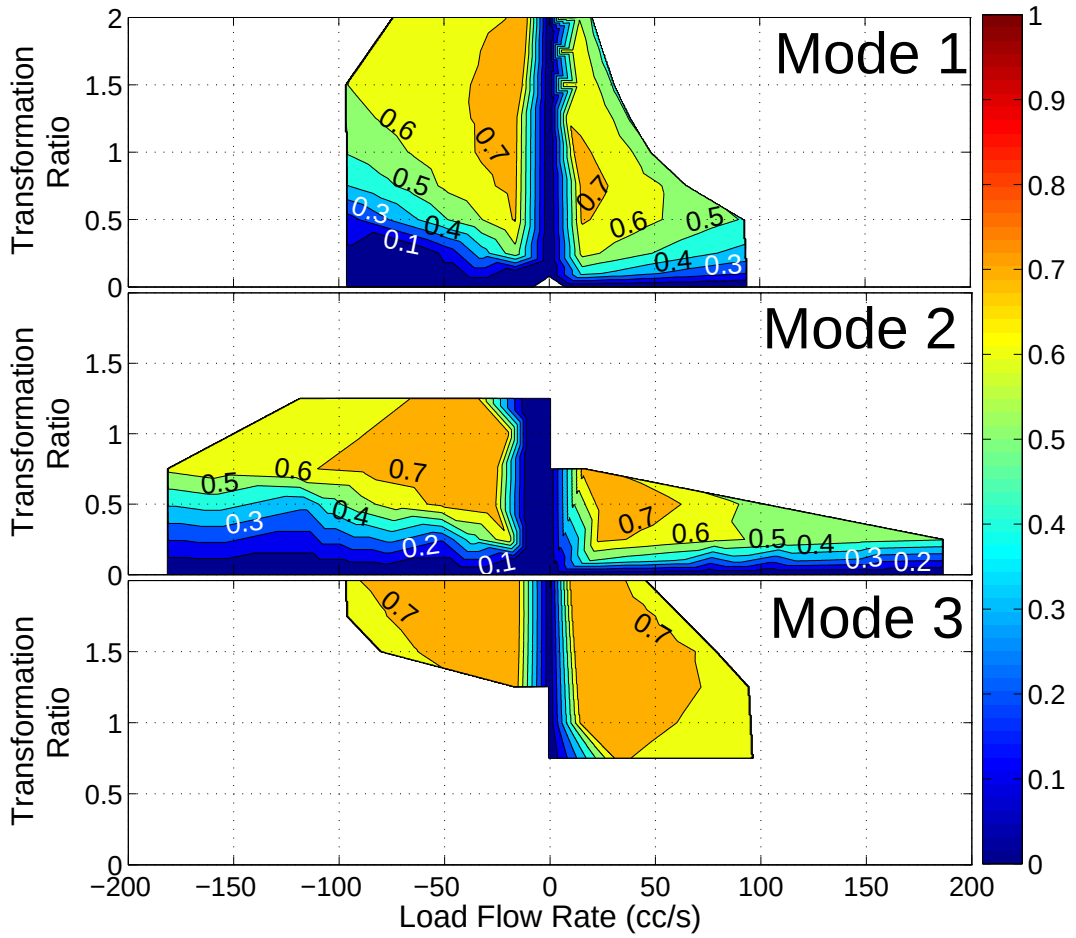

Figure 2.20: Simulated efficiency maps of a prototype transformer with untuned shoe and valve plate gaps of 5 μm

a flow rate of approximately 20 cc/s, and the efficiency decreases as the load flow rate increases from that point. This is in contrast to the mode 1 section of the experimental figure 2.19, where the maximum efficiency for a transformation ratio of 1 is located at the boundary where the load flow rate is at a maximum value of 75 cc/s, and the efficiency decreases as the load flow rate decreases from that point.

Additionally, the magnitudes of efficiency between the experimental figure 2.19 and untuned simulation 2.20 do not match well. The experimentally determined maximum efficiency for all three modes of the prototype transformer was slightly greater than 60%, whereas the maximum efficiency of all three modes of the simulated transformer was slightly above 70%.

The results of the untuned model indicate that it is necessary to tune the shoe and valve plate gap heights, such that the simulated efficiency trends and maximum values more closely matched what was experimentally observed. To do this, a search of the entire design space of reasonable gap heights was performed, where the shoe gap height was within the bounds $h_s \in (2, 20)\ \mu m$ and the valve plate gap was within the bounds $h_v \in (4, 40)\ \mu m$. The method was a simple coarse blind search of a grid of values where $h_s = [25101520]$ and $h_v = [410203040]$, followed by a finer search around the best performing gap pair. Figure 2.21 shows the simulated efficiency maps for the pair of tuned gap heights that resulted in the best match to the experimental data in terms of peak unit efficiency and the general loss trends across the entire operating region. The values identified were a shoe gap height of 13.8 μm and a valve plate gap height of 16.7 μm, for the 3.15 cc displacement rotating groups of the prototype transformer.

Experimental results 0.4 cc pump Numerical simulations from literature indicate that bearing gap sizes have a likely positive correlation with the maximum displacement of the unit's rotating group. It was therefore expected that the gap heights identified for a 3.15 cc rotating group would not be suitable for rotating groups with sufficiently different maximum displacements. To investigation this hypothesis a 0.4 cc hydraulic pump was experimentally characterized, and the shoe gap of 13.8 μm and valve gap of 16.7 μm were used to generate a performance map for a simulated 0.4 cc pump. The experimental efficiency map is shown in figure 2.22, and the simulated efficiency map is shown in figure 2.23.

The boundaries of the experimental map shown in figure 2.22 were dictated by

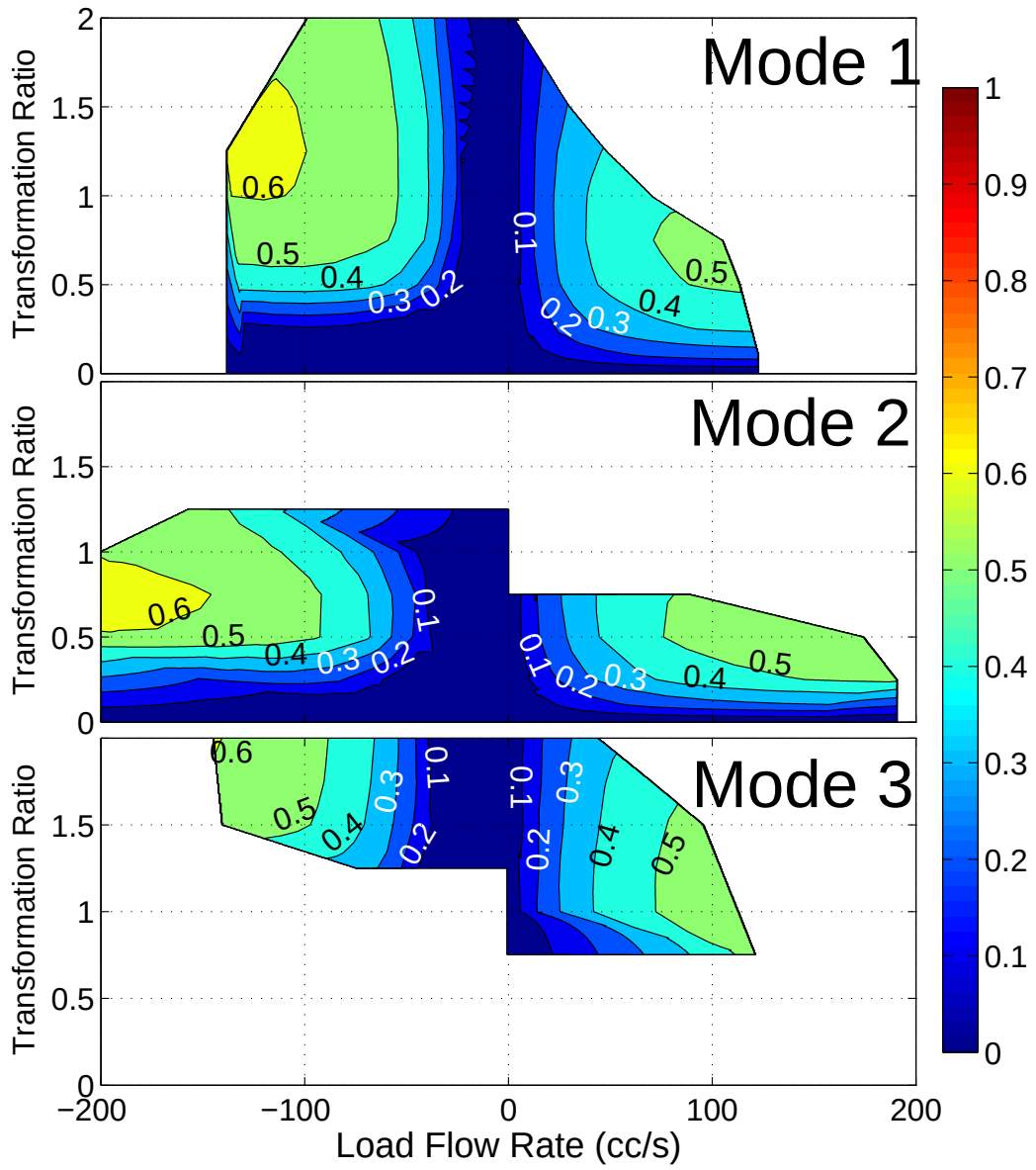

Figure 2.21: Simulated efficiency maps of a prototype transformer with tuned shoe and valve plate gaps of 13.8 and 16.7 μm

the machine's constraints. Steady state data for the area to the left of boundary A could not be obtained, as the machine would stall under those conditions. The machine could successfully pass through such a region in transient operation, but not steady state. The boundary B represents the maximum allowable pressure the unit could be operated at. Boundary C is the product of the maximum allowable rotational speed of the unit, which translates to a maximum output flow rate observed. The simulated map of figure 2.23 do not exhibit boundaries A, as the model does not capture the failure of hydrodynamic lubrication that causes stalling. The maximum allowable pressure was also relaxed for the simulation, and therefore the boundary B is not observed in figure 2.23.

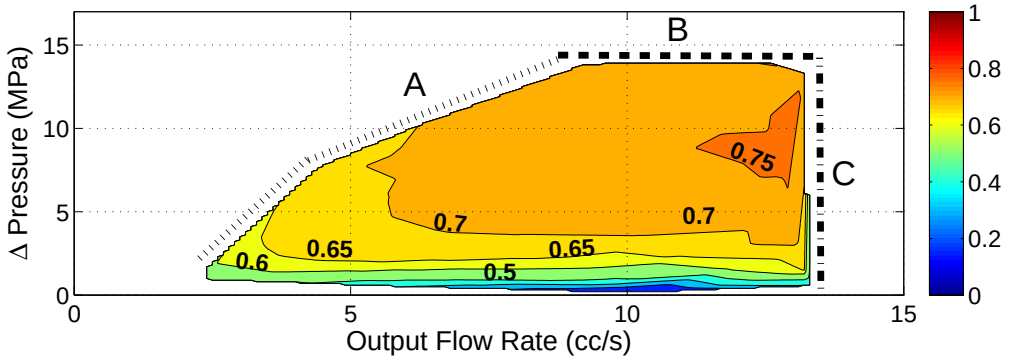

Figure 2.22: Experimental efficiency maps of a 0.4 cc hydraulic pump

The same blind search of reasonable gap values that was used to identify gaps for the 3.15 cc unit was performed for the 0.4 cc pump, and the values of $h_s = 9.1\ \mu m$ and $h_v = 10.6\ \mu m$ were identified as the parameters that resulted in the closest match between simulation and experimental results. The simulated map for the tuned values is given in figure 2.23.

Bearing Gap Scaling Law In the same manner as the physical parameters of section 2.4, it was necessary to develop a scaling law to enable simulations of rotating groups beyond the two sizes experimentally characterized. A polynomial equation was chosen to remain consistent with the form observed in the other parameter scaling trends, and the equation was fit to the data points from the 0.4 cc and 3.15 cc rotating groups.

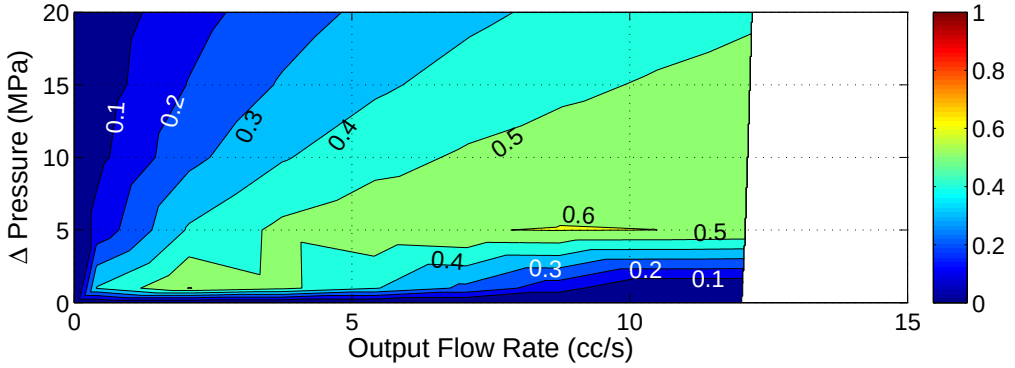

Figure 2.23: Simulated efficiency maps of a 0.4 cc hydraulic pump with untuned shoe and valve plate gaps of 13.8 μm and 16.7 μm respectively

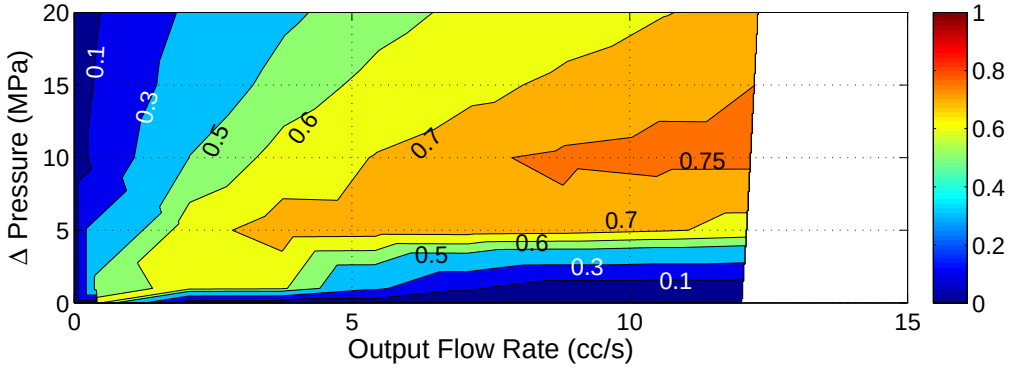

Figure 2.24: Simulated efficiency maps of a 0.4 cc hydraulic pump with tuned shoe and valve plate gaps of 9.1 μm and 10.6 μm respectively

The gap height scaling laws for piston shoe gap height h_s and valve plate gap height h_v as a function of a rotating groups maximum displacement D_{max} are:

$$h_s = \left(1.1 * 10^{-5}\right) D_{max}^{.202} \tag{2.69}$$

$$h_v = \left(1.3 * 10^{-5}\right) D_{max}^{.219} \tag{2.70}$$

2.7 Loss Distributions

Information on the distribution of each of the individual losses within a transformer can facilitate an understanding of the overall efficiency trends, of the type previously shown in 2.21. Although acquiring such information through experiment generally requires purpose-built test stands that can only investigate a restricted number of losses, the data for all the losses is readily available in simulation.

The loss distributions for the simulated prototype transformer described in section 2.6 have been plotted for three representative operating points, shown in figure 2.25. The points were chosen to illustrate the effect of both pressure and speed on the loss trends. The baseline point is with the transformer operating at 15 Hz rotational speed and a load line pressure of 10 MPa. The second point increases the speed to 30 Hz while keeping the pressure at 10 MPa, and the third point keeps the speed at 15 Hz while increasing the pressure to 30 MPa. The transformer is operating in mode 1, as described in chapter 3. All nine of the losses captured by the dynamic loss model of this chapter are shown.

Figure 2.25 shows that there can be significant variation in the distributions of losses within a transformer, based on its operating condition. Contact friction in the piston bore, viscous friction in the shoes and port plate, throttling in the piston orifices, and leakage in the port plate and piston shoes are all shown to have a meaningful impact, although their relative proportions of the total loss changes based on the imposed conditions. Couette and Poiseuille viscous friction and leakage through the piston bore are observed to be relatively small for the conditions explored.

By comparing the first and second operating conditions, where speed was varied from 15 Hz to 30 Hz, it can be seen that the contact friction in the piston bore, viscous

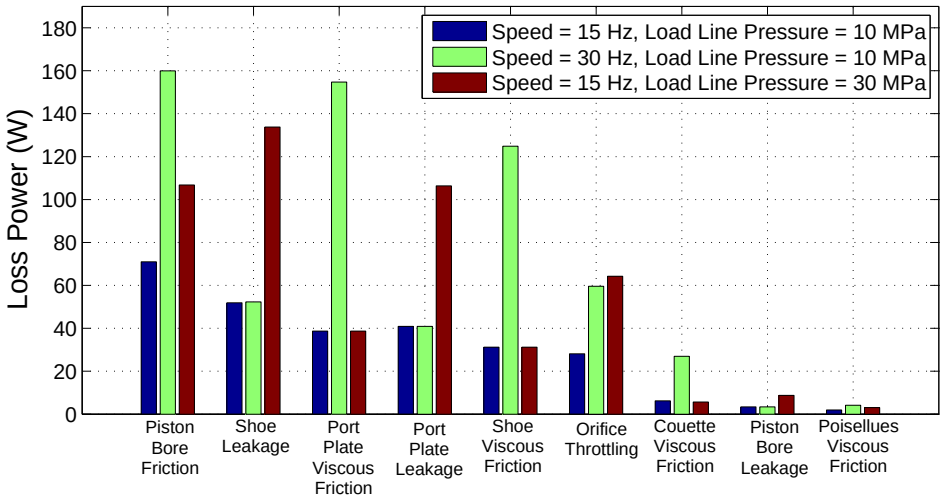

Figure 2.25: Simulated losses at three operating points for a transformer consisting of two 3.15cc rotating groups

drag in the port plate and shoes, throttling in the orifices, and friction from Couette flow are all a strong function of speed. This is expected, as velocity components can be observed in their loss equations as shown previously in this chapter. Leakage losses through the shoes and port plate were unaffected by the changes in speed.

By comparing the first and third operating conditions, where the load line pressure was varied from 10 MPa to 30 MPa, it can be seen that leakage through the piston bore, piston shoes, and port plate, as well as throttling in the piston orifices, are strongly dependent on pressure. This is expected, as the magnitude of the pressure differentials between the piston chambers and the case, and the ports and the case, drives the leakage flow. Contact friction in the piston bore is seen to be moderately dependent on the pressure, as increasing the pressure increases the contact forces. All four viscous friction losses are shown to be independent of pressure.

2.8 Chapter Summary

This chapter documented the mathematical underpinnings of a dynamic loss model of a hydraulic transformer. The model is intended as a tool to explore the performance of

transformers and their interaction with systems. The model, as well as the parameter identification and map generation procedures, are used for every simulation investigation throughout this thesis.

Chapter 3

Impact of the Configuration of a Hydraulic Transformer on System Efficiency

3.1 Chapter Overview

This chapter shows how the configuration of the hydraulic plumbing that connects a transformer to its surrounding impacts its performance. It is shown that the transformer itself can be installed in three unique configurations, and the system surrounding the transformer can be organized in two unique configurations, resulting in a total of six configurations by means of which a hydraulic transformer can be installed within a system.

The model described in chapter 2 is utilized to explore the efficiency performance and operating region of each configuration of the transformer unit itself, as well as a system that contains a transformer. It is shown that each configuration has its own unique performance map and operating region. Of interest is the exploration of three configurations called power split, which are capable of achieving greater system efficiencies than the maximum possible transformer efficiencies.

Prior work by Ho and Ahn [21] investigated the relationship between transformer

configuration and performance, but did not exhaustively consider all the possible configurations. Several papers gave qualitative discussions of a single power split configuration [40, 41], but neglected to model their behavior and therefore did not reveal their performance trends. This chapter thoroughly explores the performance of each configuration, and presents the results in maps that clearly show their unique efficiency trends.

The chapter concludes by acknowledging that it is possible to actively change the configuration of a transformer through the introduction of port switching valves. A hydraulic circuit capable of switching between all six configurations is presented, and a composite map showing the performance of such a system is shown.

3.2 Description of Hydraulic Transformer Configurations

A hydraulic transformer interfaces with three hydraulic lines; a line connected to a Common Pressure Rail, a line connected to the load, and a line connected to the tank of the hydraulic system. As a transformer has four ports, each of which could be connected to any of the three lines, there are 81 options for connecting the unit to the system. Of these options there are 57 that do not incorporate all three lines or have a single line connected to both ports of a single rotating group and therefore are not meaningful, as they are unable to achieve the transforming action that is the purpose of the unit. Examples of two non-meaningful configurations are shown in figure 3.1. The 24 remaining configurations can be grouped into 3 families of 8 each, where each family consists of reflections and rotations of the same configuration. Therefore, there are three unique, meaningful configurations for connecting a transformer to a system. These configuration are shown in figure 3.2.

Throughout this thesis the terms mode and configuration will be used interchangeably.

In addition to the various ways a transformer can be connected to the system, the system itself can be organized around the transformer in either a series or power split architecture. The transformer power split architecture is analogous to mechanical power split architectures that have been proposed for hydraulic hybrid vehicles [42]. Although the hydraulic transformer based power split architecture has been mentioned in literature [43], it has only been presented with qualitative discussions of the opportunity it

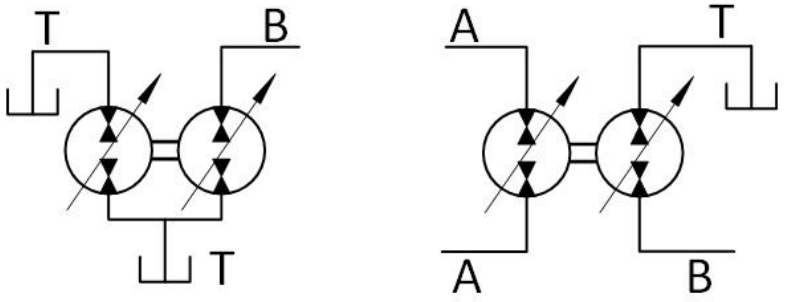

Figure 3.1: Examples of two non-meaningful transformer configurations

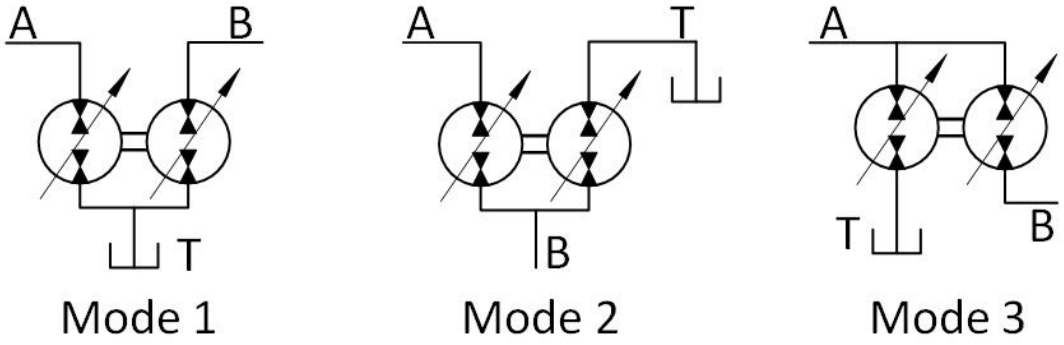

Figure 3.2: Three meaningful transformer unit configurations

presents to invert the direction of pressure drop across the load. This thesis presents the first detailed analysis of the efficiency performance of a system with such an architecture.

The series and power split architectures differ by the hydraulic connections of the load. In a series architecture, shown in figure 3.3, the non-transformer side of the load is connected to the tank line. This results in all of the fluid power flowing between the common pressure rail and the load to flow through the transformer. In a power split architecture, shown in figure 3.4, the non-transformer side of the load is connected to the rail line. This results in power flowing between the rail and the load along two parallel paths. One of the paths is through the transformer, where losses are incurred, and the other is through a simple line connection, which is nearly lossless.

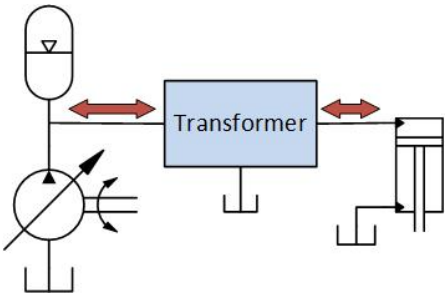

Figure 3.3: Series Architecture

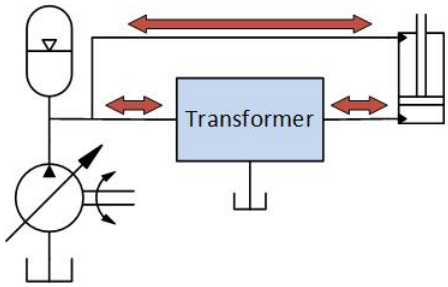

Figure 3.4: Power Split Architecture

Each of the three transformer configurations can be implemented in both the series and power split architecture, resulting in a total of six meaningful system configurations for a hydraulic transformer. These configurations are shown in figure 3.5.

3.3 Definition of Unit Efficiency

When evaluating the operation of a hydraulic transformer consideration can be given to either the efficiency of the unit itself or the efficiency of the combined transformer and actuator system. The difference is in what are defined as input and useful output power flows. This section gives the derivation for unit efficiency and the following section gives the definition of system efficiency.

When evaluating the steady state efficiency of a hydraulic transformer unit itself the only power flows of interest are the ones entering or exiting the unit directly. As

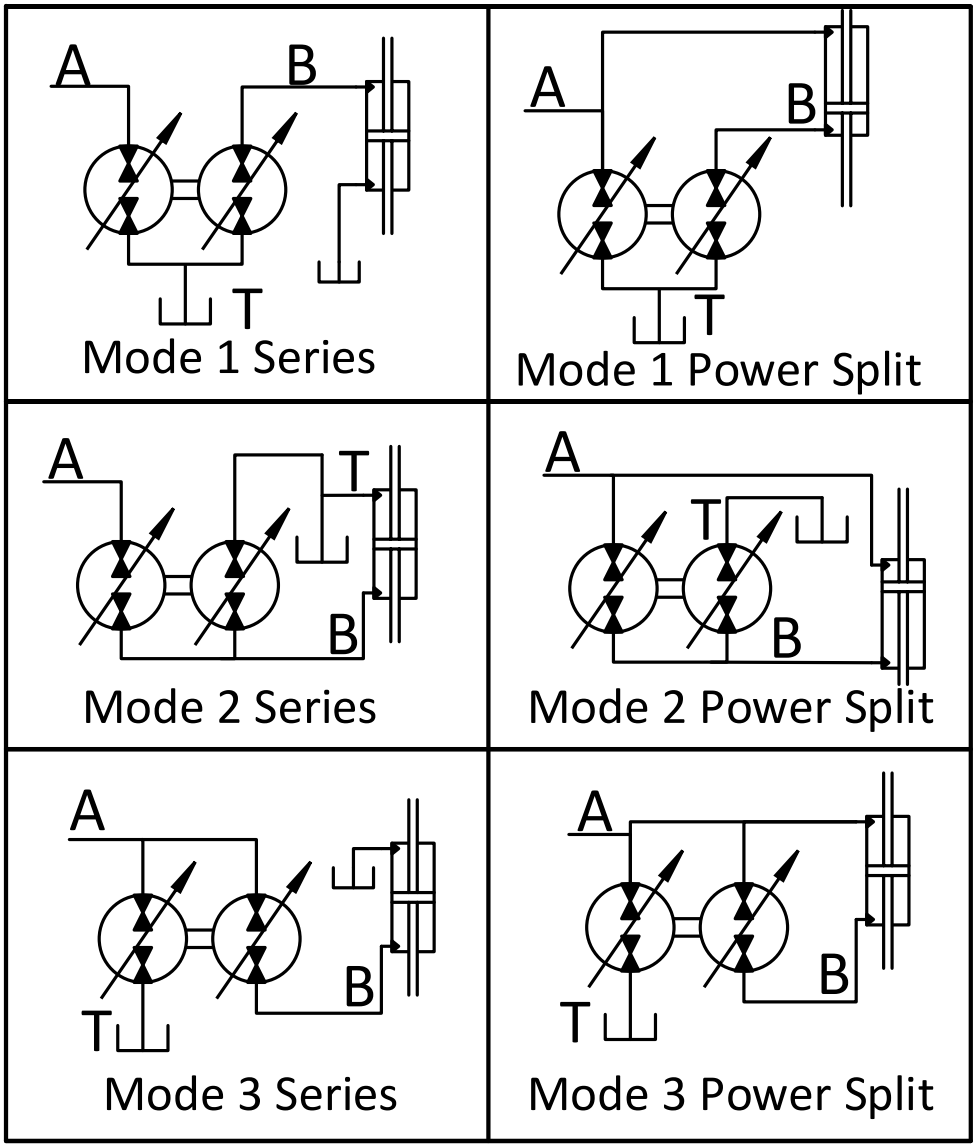

Figure 3.5: Six system configurations for distributing power with a hydraulic transformer from a common pressure rail

the mechanical components are entirely contained within the device with negligible mechanical power transfer out of the unit, the only power flows of interest are the quantities of fluid power flowing along the three connecting lines, as shown in figure 3.6. The thermal and acoustic power flows exiting the unit are considered to be losses, and are not included in the summation of useful power flowing out of the unit. The power flow of potential energy stored within the compressed fluid is not incorporated into the definitions of efficiency in this thesis, to remain consistent with industry, as observed in the hydraulic pump/motor efficiency definitions found in ISO Standard 4409.

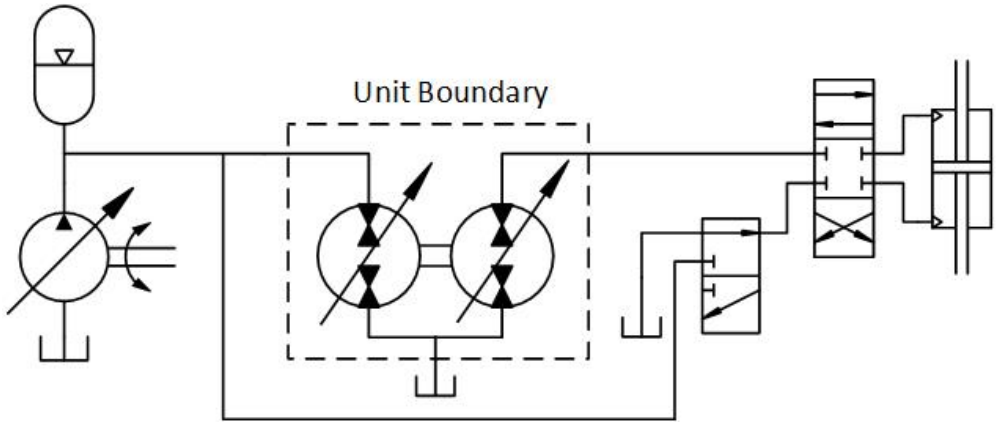

Figure 3.6: Boundary of Hydraulic Transformer Unit Within System

The fluid power of the P-th line can be obtained by the pressure P_P and volumetric flow rate Q_P of the line:

$$\mathcal{P}_{f,P}(t) = P_P(t)Q_P(t) \tag{3.1}$$

where Q_P is taken as positive if exiting the unit and P_P is gauge pressure referenced against ambient pressure. In order to evaluate the unit efficiency, it is necessary to determine both the total fluid power input $P_{f,i}$ and total fluid power output $P_{f,o}$ of the unit:

$$\begin{aligned}\mathcal{P}_{f,i}(t) =& C_{f,i}(P_A, Q_A, t)(P_A Q_A(t)) \\ &+ C_{f,i}(P_B, Q_B, t)(P_B(t)Q_B(t)) + C_{f,i}(P_T, Q_T, t)(P_T Q_T(t))\end{aligned} \tag{3.2}$$

$$\begin{aligned}\mathcal{P}_{f,o}(t) =& C_{f,o}(P_A, Q_A, t)(P_A Q_A(t)) \\ &+ C_{f,o}(P_B, Q_B, t)(P_B(t)Q_B(t)) + C_{f,o}(P_T, Q_T, t)(P_T Q_T(t))\end{aligned} \tag{3.3}$$

where $C_{f,i}(P_P, Q_P, t)$ and $C_{f,o}(P_P, Q_P, t)$ are indicator functions of the form:

$$C_{f,i}(P_P, Q_P, t) = \begin{cases} 1 & P_P(t)Q_P(t) < 0 \\ 0 & \text{else} \end{cases} \tag{3.4}$$

$$C_{f,o}(P_P, Q_P, t) = \begin{cases} 1 & P_P(t)Q_P(t) > 0 \\ 0 & \text{else} \end{cases} \tag{3.5}$$

The total unit steady state unit efficiency for a given operating point of a hydraulic transformer can then be written as:

$$\eta_t = \frac{\mathcal{P}_{f,o}(t)}{\mathcal{P}_{f,i}(t)} \tag{3.6}$$

where

$$\begin{aligned}\mathcal{P}_{f,o}(t) =& P_A Q_A(t) C_{f,i}(P_A, Q_A, t) \\ &+ P_B(t)Q_B(t)C_{f,i}(P_B, Q_B, t) + P_T Q_T(t) C_{f,i}(P_T, Q_T, t)\end{aligned} \tag{3.7}$$

and

$$\begin{aligned}\mathcal{P}_{f,i}(t) =& P_A Q_A(t) C_{f,o}(P_A, Q_A, t) \\ &+ P_B Q_B(t) C_{f,o}(P_B, Q_B, t) + P_T Q_T(t) C_{f,o}(P_T, Q_T, t)\end{aligned} \tag{3.8}$$

3.4 Definition of System Efficiency

When evaluating the efficiency of the system that has a transformer within it, the boundary is different than the boundary used for evaluating the efficiency of just the unit. As the hydraulic power distribution systems under consideration transform power from the common pressure rail to power of a linear actuator, the power flows of interest are the fluid power of the rail line, the low pressure tank line, and the mechanical power of the actuator, as shown in figure 3.7.

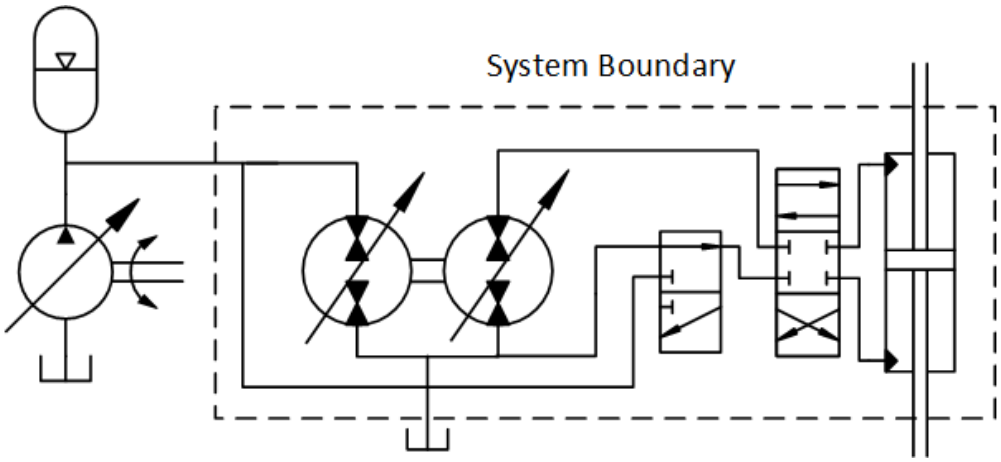

Figure 3.7: Boundary of Power Distributing System

The fluid power of the rail line and tank line can be obtained by their pressures and volumetric flow rates:

$$\mathcal{P}_{f,A}(t) = P_A Q_A(t) \tag{3.9}$$

$$\mathcal{P}_{f,T}(t) = P_T Q_T(t) \tag{3.10}$$

where the flow rates Q_A and Q_T are taken as positive if exiting the system and the line pressures P_A and P_T are gauge pressure referenced against ambient pressure. The mechanical power of the linear actuator P_a can be obtained as the force F_a acting by the actuator on the load, and it's and velocity v_a:

$$\mathcal{P}_a(t) = F_a(t) v_a(t) \tag{3.11}$$

Both the fluid power of the rail and the mechanical power of the actuator can be either positive or negative. For both quantities, a positive value represents energy flowing out of the system and a negative value represents energy flowing into the unit. Therefore, the total input power and total output power can be determined by:

$$\begin{aligned}\mathcal{P}_{t,i}(t) =& C_{f,i}(P_A, Q_A, t)(P_A Q_A(t)) \\ &+ C_{f,i}(P_T, Q_T, t)(P_T Q_T(t)) + C_{a,i}(F_a, v_a, t)(F_a(t) v_a(t))\end{aligned} \tag{3.12}$$

$$\begin{aligned}\mathcal{P}_{t,o}(t) =& C_{f,o}(P_A, Q_A, t)(P_A Q_A(t)) \\ &+ C_{f,o}(P_T, Q_T, t)(P_T Q_T(t)) + C_{a,o}(F_a, v_a, t)(F_a(t) v_a(t))\end{aligned} \tag{3.13}$$

where $C_{f,i}(P_T, Q_T)$ and $C_{f,o}(P_T, Q_T)$ are given by Eq (5.5) and (3.5) and $C_{a,i}(F_a, v_a, t)$ and $C_{a,o}(F_a, v_a, t)$ are indicator functions of the form:

$$C_{a,i}(F_a, v_a, t) = \begin{cases} 1 & F_a(t) v_a(t) < 0 \\ 0 & \text{else} \end{cases} \tag{3.14}$$

$$C_{a,o}(F_a, v_a, t) = \begin{cases} 1 & F_a(t) v_a(t) > 0 \\ 0 & \text{else} \end{cases} \tag{3.15}$$

The efficiency for a system in steady state operation, regardless of the method of power distribution, can then be written as:

$$\eta_t(t) = \frac{\mathcal{P}_{t,o}(t)}{\mathcal{P}_{t,i}(t)} \tag{3.16}$$

where

$$\begin{aligned}\mathcal{P}_{t,o}(t) =& C_{f,i}(P_A, Q_A, t)(P_A Q_A(t)) \\ &+ C_{f,i}(P_T, Q_T, t)(P_T Q_T(t)) + C_{a,i}(F_a, v_a, t)(F_a(t) v_a(t))\end{aligned} \tag{3.17}$$

and

$$\begin{aligned}\mathcal{P}_{t,i}(t) =& C_{f,o}(P_A, Q_A, t)(P_A(t) Q_A(t)) \\ &+ C_{f,o}(P_T, Q_T, t)(P_T Q_T(t)) + C_{a,o}(F_a, v_a, t)(F_a(t) v_a(t))\end{aligned} \tag{3.18}$$

If a hydraulic system designer considers the energy requirements necessary to maintain a certain operating condition of an actuator to be a quantity of interest for their

system, then the system efficiency is an appropriate metric but the unit efficiency is not. The system efficiency is directly related to the power the system required in order to achieve a certain actuator operating condition, which can then facilitate comparison against other technologies. This is in contrast to the unit efficiency, which only includes power flowing into and out of the transformer, and does not have a one-to-one mapping to the system performance. The unit efficiency still has significant value in facilitating understanding of the transformer operation, as well as being a useful tool for a machine designer seeking to improve the performance of the unit, but should not be used to compare various system architectures.

With the definitions of efficiency given above, it is possible for a transformer to have an efficiency of zero but still be performing a useful function. This instance can occur in quadrant two and four, where the transformer is absorbing power from an actuator with the nominal objective of regenerating it back into the rail. If leakage losses within the rotating group that is attached to the rail are greater than the flow being regenerated back into the rail, then there is no useful power flowing out of the system or the unit, resulting in an efficiency of zero. There is still value in the ability to control the operating behavior of the regenerating load in this scenario, so these regions should not be discarded when evaluating the total system operating region.

Throughout this thesis the pressure of the tank line is assumed to be ambient pressure, but such operation is not a requirement. The tank line could operate at a raised pressure as a low pressure rail line. The efficiency and performance implications of such operation is not investigated in this thesis.

3.5 Description of the Transformer and System Under Analysis in this Chapter

To facilitate understanding of the performance and operating regions of the various transformer configurations, the dynamic loss model described in chapter 2 was utilized to generate a set of maps. Each of the maps in this chapter were generated using the process described in section 2.5.

The maps shown in the sections 3.6 and 3.8 were generated for a transformer with geometrical parameters identical to a prototype transformer consisting of two 3.15 cc

variable displacement rotating groups. A set of the most significant parameters for the transformer are given in table 5.1, and the complete list of parameters are given in appendix A. The system parameters are given in table 3.2.

Table 3.1: Hydraulic transformer size parameters and constraints

Parameter or Constraint	Value
Maximum Displacement of Rotating Group 1	3.15 cc
Maximum Displacement of Rotating Group 2	3.15 cc
Number of Pistons per Rotating Group	7
Maximum Swashplate Angle	13 degrees
Maximum allowable rotation speed	30 Hz
Maximum allowable output pressure	40 MPa

Table 3.2: System parameters

Parameter	Value
Rail line pressure	20 MPa
Tank line pressure	0 MPa
Actuator Style	Double rod cylinder actuator

As the objective of this investigation was to explore the efficiency trends and operating region of a hydraulic transformer distribution architecture and enable comparison against other hydraulic power distribution technologies, a set of model simplifications were made. All modeled valves, pipes, and actuators were considered to be lossless, performing their function without impinging losses on the system. This eliminates the need to make assumptions about a large number of design variables with non-obvious solutions, such as valve sizes, fitting orientations, and actuator sealing styles, reducing the model complexity. Modeling such ancillary features as ideal also facilitate a more direct comparison of the trends of power distribution technologies themselves.

Additionally, all of the efficiency values shown in the maps in the following section are solved for steady state operation. This is a simplification, as any actual trajectory would contain transient operation. Transition operation would require unbalanced net torque between the two rotating groups of the transformer, in order to accelerate or decelerate the unit. The unbalanced torque would be achieved by setting the variable rotating groups to slightly different displacements than what would be required to achieve steady

state. Such an adjustment could either increase or decrease the instantaneous losses, depending on the nature of the adjustment. Additionally, consideration would have to be given to kinetic potential energy stored within the rotating group. The steady state simplification was considered acceptable for the investigation of this chapter as evaluating the impact of transient behavior requires assumptions about the trajectory being implemented, and this investigation is a generalized examination of the entire operating regions of various transformer configurations.

3.6 Efficiency Performance and Operating Regions of the Three Unit Configurations

Understanding of the characteristics of each of the three unit configurations aids in the understanding of the performance of the six system configurations.

Each of the three transformer unit configurations has a unique operating region and trends for efficiency within that region. Figure 3.2 shows the schematics of the three configurations, and figure 3.8 shows the corresponding performance of a unit in that configuration. The efficiency values of figure 3.8 are unit efficiency, as derived in section 3.3.

The operating regions of figure 3.8 are shown in terms of the fluid power flowing into or out of the transformer through the line that would be connected to a load in a system. A given operating point is characterized by the output flow rate and the pressure transformation ratio λ, where the pressure transformation ratio is defined as the ratio of the pressure in the load line P_B to the pressure in the rail line P_A, both relative to the tank pressure. Therefore a transformation ratio of greater than one is considered to be boosting the pressure and a transformation ratio of less than one is considered to be bucking the pressure.

$$\lambda(t) = \frac{P_B(t)}{P_A} \tag{3.19}$$

In figure 3.8, a positive flow rate on the x-axis equates to fluid exiting the transformer along the load line and a negative flow rate equates to fluid entering the transformer along the load line. The boundaries of the operating region were defined by the flow

rates achieved within the rotational speed limits of the device. A complete discussion of the assumptions and methods for generating figure 3.8 are given in section 2.5.

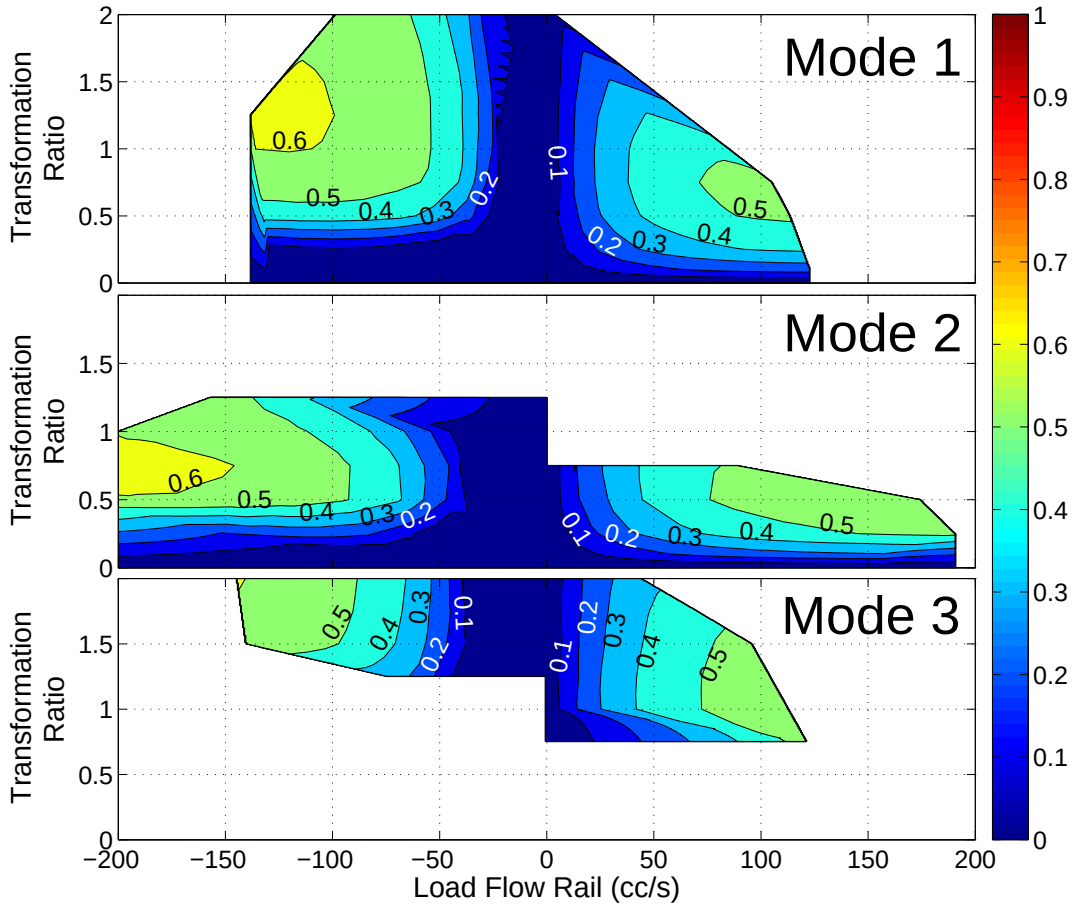

Figure 3.8: Efficiency maps and operating regions of three transformer unit configurations operating off of a 20 MPa rail pressure, corresponding to three configurations shown in Figure 3.2

3.7 Discussion of Three Unit Configurations

Figure 3.8 shows that each mode has a unique operating region and efficiency trends. These characteristics can be understood through a simple ideal analysis of the unit.

For an ideal hydraulic pump/motor operating at steady state, the relationship between torque $T_{P/M}$, the pressure drop ΔP across the unit, and the instantaneous displacement D can be written as:

$$T_{P/M}(t) = \frac{\Delta P(t) D(t)}{2\pi} \tag{3.20}$$

where both the pressure drop ΔP and the displacement value D can be either positive or negative. The sign convention for torque is positive in the clockwise direction when viewing the shaft of the machine along its axis from the direction that does not penetrate the machine. Which direction of pressure drop and displacement is considered positive is arbitrary, as long as it aligns with the torque convention and equation 3.20 is respected.

Considering that a transformer consists of two hydraulic pump/motors connected on a shaft, and applying a torque balance, the equation for the ideal (no mechanical loss) relationship between the pressure drop across the two units in steady state can be written by equating the torque on the common shaft:

$$\Delta P_1 D_1 = \Delta P_2 D_2 \tag{3.21}$$

where both the pressure drop ΔP and the displacement value D can be either positive or negative. Note that the conventional way of defining the sign of torque of an individual unit, as described above, results in the torques of the individual machine having opposite signs when combined. For example, equal positive torques on two units assembled face-to-face will result in a net torque of zero.

By replacing the pressure drop term with the respective associated ports of each configuration, as shown in figure 3.2, we can arrive at the relationship between the three port pressures. For mode 1 (Tank shared configuration):

$$(P_A - P_T) D_1 = (P_B - P_T) D_2 \tag{3.22}$$

For mode 2 (Load shared configuration):

$$(P_A - P_B) D_1 = (P_B - P_T) D_2 \tag{3.23}$$

And for mode 3 (Pressure rail shared configuration):

$$(P_A - P_T)D_1 = (P_B - P_A)D_2 \tag{3.24}$$

Taking the tank pressure P_T as zero and rearranging to solve for the transformation ratio λ as given in equation (3.19), the relationship between the rail pressure P_A and output pressure P_B for a given ratio of displacements can be written for mode 1 as:

$$\frac{D_1}{D_2} = \frac{P_B}{P_A} = \lambda \tag{3.25}$$

For mode 2:

$$\frac{D_1}{D_1 + D_2} = \frac{P_B}{P_A} = \lambda \tag{3.26}$$

And for mode 3:

$$\frac{D_1 + D_2}{D_2} = \frac{P_B}{P_A} = \lambda \tag{3.27}$$

As discussed in section 2.5, a hydraulic pump/motor operating a given flow rate is often most efficient when at maximum displacement. Assuming that the two individual units are most efficient at maximum displacement, it can be expected that a transformer operating at a given load flow rate will be most efficient when both of its units are at maximum displacement. For a transformer where $\left|\frac{D_{1,max}}{D_{2,max}}\right| = 1$, such as the one simulated in this section, the transformation ratio where the maximum efficiency is expected to occur for ideal steady state behavior can be found for mode 1 as:

$$\lambda_{\eta,max} = 1 \tag{3.28}$$

For mode 2:

$$\lambda_{\eta,max} = \frac{1}{2} \tag{3.29}$$

And for mode 3:

$$\lambda_{\eta,max} = 2 \tag{3.30}$$

For non-ideal operation, where losses are modeled, it is expected that the actual transformation ratio for maximum efficiency $\lambda_{\eta,max}$ would be slightly offset from the ideal value. For quadrant one, where the output flow is positive, it is expected that $\lambda_{\eta,max}$ would be slightly lower than the ideal value, as torque losses within the unit would decrease the actual output pressure P_B that would be generated when both units are at maximum displacement. Conversely, in quadrant two where the load flow rate is negative, the $\lambda_{\eta,max}$ would be slightly higher than the ideal value. This is because torque losses would require a slightly larger load pressure P_B in order to regenerate back into fixed pressure of the rail.

These trends are observed in the simulated model, as shown in figure 3.8. From this it can be concluded that each mode has a range of transformation ratios in which it outperforms the other two modes, in terms of efficiency. If the transformation ratio is around one, mode 1 is the most efficient. If the transformation ratio is sufficiently below one, conventionally called bucking, mode 2 is the most efficient. If the transformation ratio is sufficiently above one, conventionally called boosting, mode 3 is the most efficient. The actual transition points at which each mode is preferred will vary depending on the design of the transformer and the current operating conditions.

The relationships between efficiency and transformation ratio noted in this section apply to a transformer with units of equal displacement. The transformation ratios at which the maximum efficiency is observed would shift up or down if a transformer was designed with units of unequal displacements. The process of optimizing the displacements of a transformer for a given duty cycle is discussed in chapter 5.

In addition to efficiency considerations it can be observed that mode 2 is capable of achieving much higher load flow rates than the other two configurations. This trend can be understood by noting that both of the rotating groups of the mode 2 configuration are connected to the load line, as observed in the corresponding schematic of figure 3.2. Therefore both rotating groups contribute their flow rate to the load line. As the boundary of the operating region is determined by the operation of the unit while rotating at the maximum allowable speed, and the fluid displaced per revolution to or from the load line is twice as much for mode 2 than the other two configurations, it can be expected that the maximum flow rate of mode 2 would be approximately twice as much as mode 1 or mode 3. This trend is observed in figure 3.8. This ability to boost

load flow rate has significant value in extending the operating region of a traditional hydraulic transformer.

3.8 Efficiency Performance and Operating Regions of the Six System Configurations

In a similar manner as the three unit configurations, each of the six system configurations has a unique operating region and trends for efficiency within that region. Figure 3.9 shows the steady state efficiency performance of the six meaningful configurations for a transformer consisting of two 3.15 cc axial piston pump/motors, and figure 3.5 shows the schematics of the corresponding systems. In contrast to the unit configuration section, the efficiency values of figure 3.9 are the system efficiency, as derived in section 3.4. The performance was simulated using the model described in chapter 2, with the parameters given in appendix A. The maps were generated using the procedure described in section 2.5.

The operating region of figure 3.9 are shown in terms of the fluid power flowing into or out of the transformer through the line that is connected to the systems load. A given operating point is characterized by the output flow rate and the pressure drop across the load. These quantities were chosen to enable comparison against the unit performance maps, and because the flow rate and pressure drop across an ideal actuator has a direct linear relationship with the force and velocity of the actuator, which would be the quantities of interest for characterizing the systems behavior. A positive flow rate equates to fluid exiting the transformer along the load line and a negative flow rate equates to fluid entering the transformer along the load line.

The transformation ratio λ that has been traditionally used to describe the relationship between the load pressure P_B and the rail pressure P_A for the operation of a unit is not used to discuss the behavior of the system. This is because the introduction of the power split modes of operation confound the relationship between the load pressure P_B and the actual pressure drop ΔP across the load. For example, if the system is configured in mode one power split, and the transformation ratio is one, then then $P_B = P_A$. Since the load is connected to the rail in power split configurations, then the actual load pressure drop would be zero in this scenario. To avoid confusion the system operating

region is described with the load pressure drop ΔP, which can be achieved through different transformation ratios, depending on the configuration. The load pressure drop can either be the difference between the load pressure P_B and the tank pressure P_T, or the load pressure P_B and the rail pressure P_A, depending on whether the unit is in a series or power split mode respectively.

As with the definition of efficiency for a unit, it is also possible to have a system efficiency of zero but still having the system performing a useful function. This can occur when the transformer is absorbing input power from the actuator, but due to losses the system is unable to regenerate a positive quantity of energy back into the rail. There is still value in the ability to control the operating behavior of the regenerating load in this scenario, so these regions should not be discarded when evaluating the total system operating region.

3.9 Discussion of Six System Configurations

By comparing the system configuration results in figure 3.9 against the unit performance results of figure fig:unitEta, it can be observed that the three series configurations have the same performance maps as the three unit configurations. This can be understood by examining the corresponding schematics in figure 3.5. It can be seen that all of the power must pass through the transformer while being transferred between the rail and the load. As the load and lines have been simulated as lossless, the transformer is the only component impinging losses on the system. Therefore, as all of the power must pass through the transformer, its efficiency characterizes the efficiency of the system when in series configuration.

When examining the performance of the power split configurations in figure 3.9, it can be observed that their efficiency trends are substantially different than the corresponding unit performance trends of figure 3.8. Most noteworthy is the fact that mode 1 and mode 2 in power split configuration achieve higher system efficiencies than the highest observed unit efficiencies for their corresponding modes.

To understand how a system can achieve higher efficiency than the transformer component controlling it, an example power flow diagram is given in figure 3.10. The diagram shows a power split configuration operating at -100 cc/s flow rate Q_B and -16

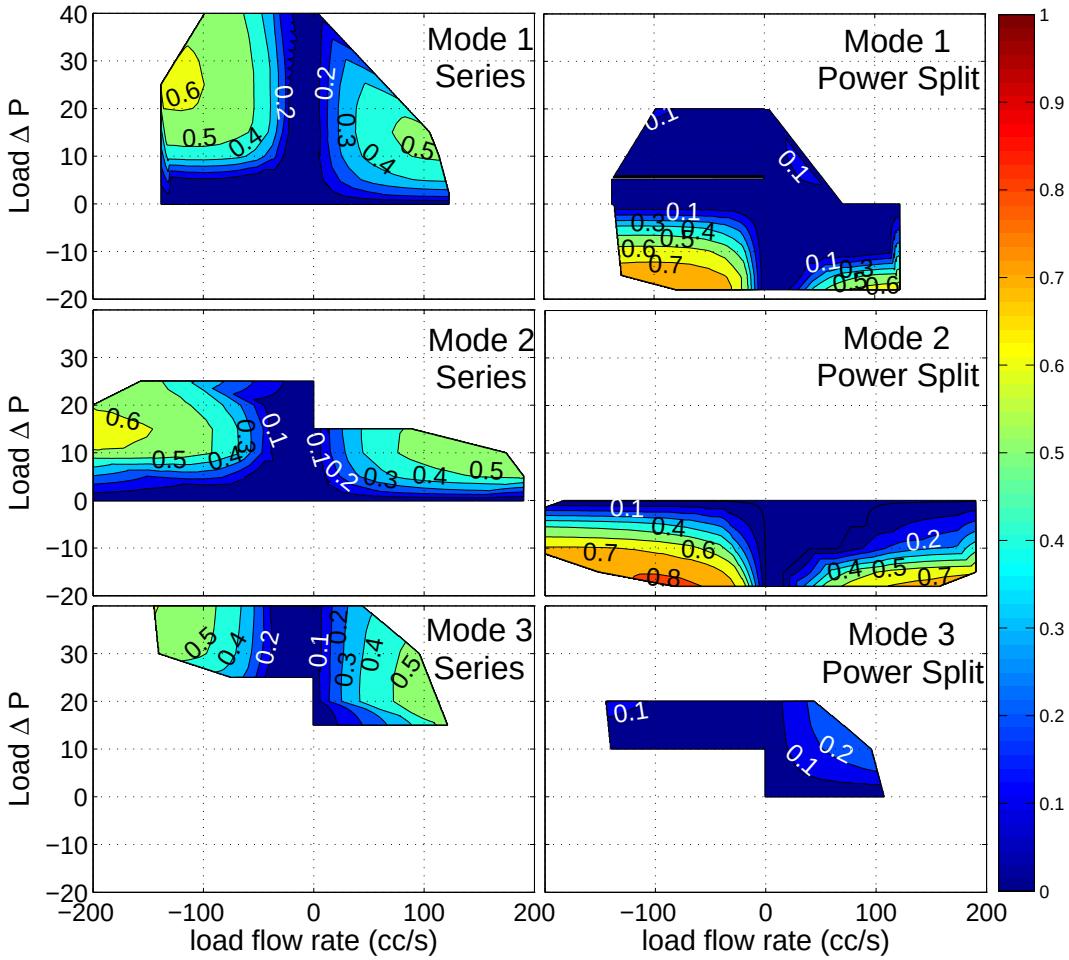

Figure 3.9: Efficiency maps and operating regions of six system configurations operating off of a 20 MPa pressure rail, corresponding to the six configurations shown in Figure 3.5

MPa pressure drop ΔP across the load. It can be seen that nearly an order of magnitude more power passes through the parallel rail line than through the transformer itself, with the two functions of the transformer being to control the load behavior and recover a portion of the unused power from the fluid passing through the load.

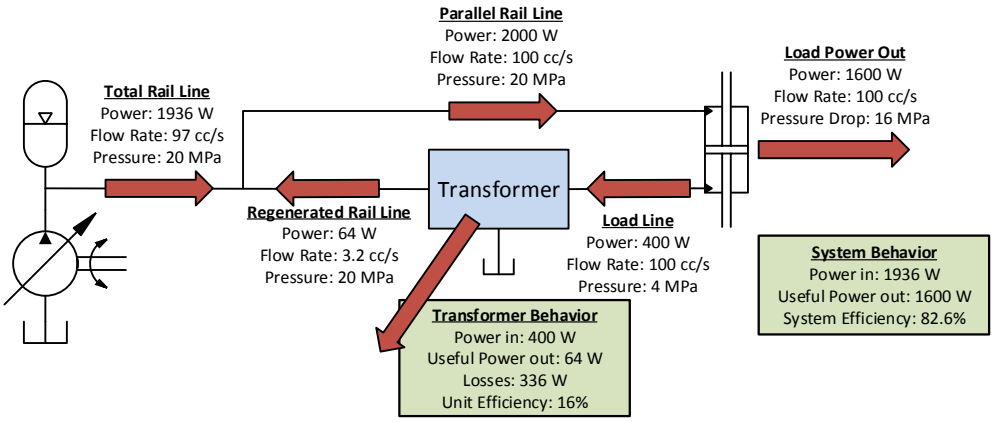

Figure 3.10: Example of how a power split configuration can achieve higher system efficiency than unit efficiency

It can be observed that the majority of the power flowing between the rail and the load actually flows through the connecting hydraulic line, which is considered to be lossless in this case study and is nearly lossless in practice. The significant pressure drop across the load in this operating condition removes most of the power from the fluid. Therefore, when the fluid is absorbed into the transformer, the magnitude of power is small. In these conditions the efficiency of the transformer itself is very low, however since the magnitude of power is small, the losses that are ultimately impinged upon the system are also small. Since a large amount of power is being output from the system through the load but only a small amount of losses are incurred in the transformer, the total system efficiency is high.

This demonstrates a key finding: When operating in a power split configuration, there is not a direct mapping of the transformer efficiency to the system efficiency. In particular, a transformer-controlled system can achieve a system efficiency that is greater than the maximum efficiency possible by the transformer itself through a power split configuration. This is achieved by passing most of the power through a parallel

path to the transformer, while positioning the transformer downstream of the load such that it can still achieve the control objectives that make it necessary.

The maximum efficiency of the power split configuration is achieved when the pressure drop across the load equals the rail pressure, requiring a load pressure P_B of zero for the transformer load line. In such a situation, all of the useful power is flowing through the nearly lossless line parallel to the transformer, and the transformer itself is only impinging minor losses on the system while managing the flow of ambient pressure oil.

With respect to load flow rate trends, mode 2 in shown to achieve maximum values nearly twice as high as mode 1 or mode 3 in both series and power split configurations. This can be understood by the same reasoning as the flow rate trend observed in the unit configuration discussion of section 3.7, where it was noted that connected the load line to both rotating groups allows a transformer to absorb or output greater volumetric flow rates. The system operating regions shown in figure 3.9 indicate that the fluid flow rate trends of a transformer unit extend to the system itself.

3.10 Generating a Composite Map from System Maps

An important detail is that the actual physical hydraulic transformer does not change between configurations, and switching between the six options is only a matter of changing how the porting is connected. Therefore switching between various configurations during operation can be achieved by the introduction of hydraulic valves. One possible circuit capable of achieving all six configurations is shown in figure 3.11. The addition of two 3/2 valves, labelled as valve 1 and 2 in figure 3.11, allows for switching between modes 1, 2, and 3. The addition of another 3/2 valve connected to the load, labelled valve 3, allows for switching between series and power split configurations. The addition of a 4/2 valve, labelled valve 4, allows for the pressure and flow rate relationship between the load and the transformer to be inverted. The action of switching between transformer configurations during operation is hereafter called port switching.

Table 3.3 gives the states of the valves shown in figure 3.11 necessary to achieve each configuration. A default state corresponds to the flow path indicated by the current state of the corresponding 3/2 valve in figure 3.11. An activated state corresponds to

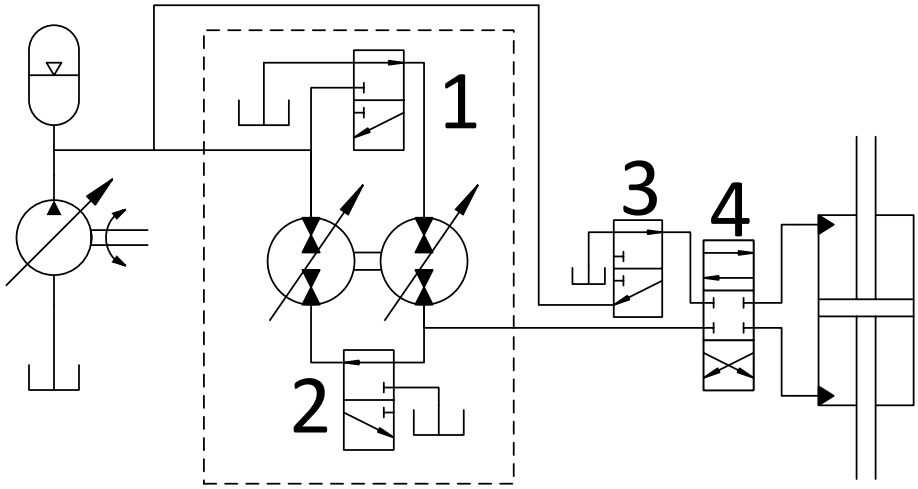

Figure 3.11: Hydraulic circuit capable of switching between all six system configurations - valves shown in default position

the alternate flow path of the corresponding 3/2 valve. For example, the default state of valve 1 connects the second rotating group to the tank line, whereas the activated state connects the rotating group to the pressure rail. Valve 4 can be in either of its non-blocked states for any configuration, as it only inverts the pressure and flow rate sign relationships between the transformer and the load, and does not play a role in defining the current configuration.

Table 3.3: Port switch valve states for all six configurations

Configuration	**Valve 1**	**Valve 2**	**Valve 3**	**Valve 4**
Mode 1 Series	Default	Default	Default	Either
Mode 1 Power Split	Default	Default	Activated	Either
Mode 2 Series	Default	Activated	Default	Either
Mode 2 Power Split	Default	Activated	Activated	Either
Mode 3 Series	Activated	Default	Default	Either
Mode 3 Power Split	Activated	Default	Activated	Either

Assuming that efficient operation is one of the primary concerns of a hydraulic system designer, it is reasonable to assume that the valves would be controlled such that the transformer is in the most efficient configuration for any particular operating

point. A composite map can be generated to show the combined operating regions of all six configurations, where the configuration with the maximum efficiency for each point is selected for each operating point. An example composite map is shown in figure 3.12, having been generated using the six configuration maps of a prototype transformer.

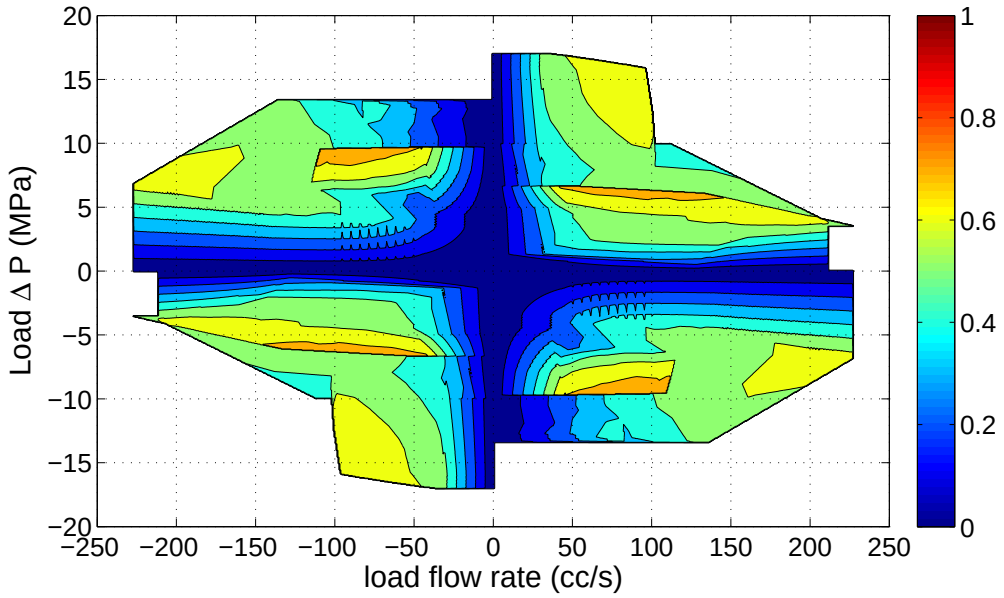

Figure 3.12: Composite efficiency map of highest efficiency possible across all six configurations for an example transformer

Composite efficiency maps, such as figure 3.12, are useful for understanding the total possible operating region and efficiency trends of a port switching transformer, but do not show how the behavior is achieved. Additionally, the efficiency maps do not display information as to which configuration should be implemented for a given operating point, which is a necessary input to the actual operation of a port switching transformer. In order to present such information, a figure which is hereafter called a 'porting map' is introduced. The porting map contains information as to which of the six configurations has the highest efficiency for a given operating point. An example porting map is shown in figure 3.13, which is for the same transformer as is characterized in the efficiency map of figure 3.12. The information contained with a porting map can be combined with the valve state information in table 3.3 to generate a lookup table

that specifies what valve states should be implemented to achieve the greatest possible steady state efficiency for a input load pressure drop and flow rate demand. This type of lookup table is implemented in chapter 4 during the experimental investigation of port switching behavior.

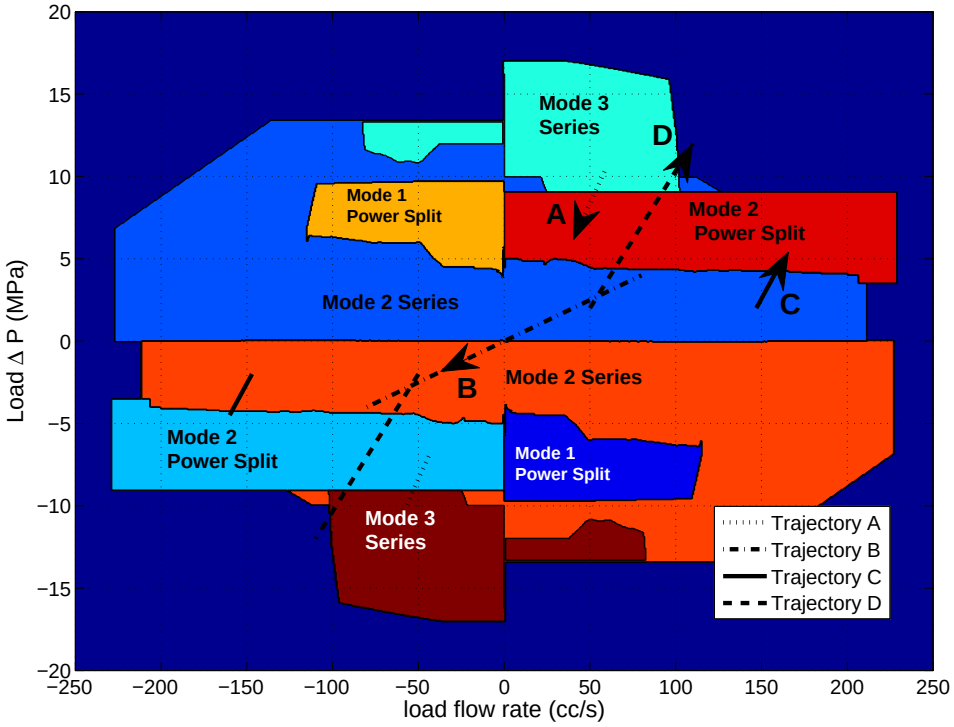

Figure 3.13: A 'porting map' showing which configuration has the highest steady state efficiency for a given load flow rate and pressure drop

3.11 Chapter Summary

This chapter explored the performance of each of the six configurations by means of which a hydraulic transformer can be connected to a system. Simulation results exploring the efficiency performance and operating regions of each configuration were

presented. A central result of the investigation was the demonstration that each configuration had unique performance maps and could generally outperform the other configurations for a particular region of operation.

Definitions of efficiency for just the transformer unit itself as well as the actuator and transformer system as a whole were derived. Results of the power split configurations revealed that the efficiency of the system does not always have a directly proportional relationship to the efficiency of the unit at a given operating point. The power split configuration, which can distribute the majority of the hydraulic power to the actuator through a nearly lossless hydraulic line parallel to the transformer, is able to achieve higher system efficiencies than what has been demonstrated with standard configurations in prior literature, such as in [44].

The final section discussed the potential of switching between configurations during operation, depending on which configuration would be most appropriate for the current instantaneous conditions of the transformer. A circuit capable of achieving such port switching behavior is presented, and the information tool called a porting map is introduced to shown which configuration is capable of achieving the highest efficiency for a given load flow rate and pressure drop. Chapter 4 investigates the behavior of the circuit on a prototype transformer, with an emphasis on exploring the transition events between configurations. Chapter 5 and 6 present case studies that optimize the design of a port switching transformer and explore its performance in driving the leg joints of a humanoid robot.

Chapter 4

Port Switching Experimental Implementation

4.1 Chapter Overview

The investigation of the six possible system configurations in chapter 3 clearly demonstrated the ability to increase the size of the operating region and to improve the efficiency performance of a hydraulic transformer by including valves that allow it to switch between configurations during operation. The action of actively switching the transformer configuration by means of valves will hereafter be called port switching, and a transformer combined with the necessary valves will be called a port switching transformer.

The objective of this chapter is the exploration of the characteristics of the transition events between different system configurations. This investigation was motivated by the fact that simulation model of chapter 2 indicated that there would be sharp changes in the shaft speed of the transformer during transition, including reversals of direction. To explore the transition events a test bench was set up with a prototype transformer, instrumentation, and valves necessary to achieve port switching and observe the behavior of the unit during transition.

A series of experiments was performed in which the prototype transformer crossed the boundaries between configurations that are neighbors on the porting map, the generation of which is described in section 2.5. A picture of the experimental setup is

given in figure 4.1 and a schematic is shown in figure 4.2. The experimental setup utilized the same valve scheme that was presented in section 3.10 that is capable of achieving all six transformer configurations as well as inverting the flow rate direction relationship between the transformer and the load. The pressure rail was held at 10 MPa throughout the experiments of this chapter. A needle valve was used to load the system, and the pressure drop across the load was determined by pressure transducers both upstream and downstream of the load. A complete list of the instrumentation and valve components is given in appendix C.

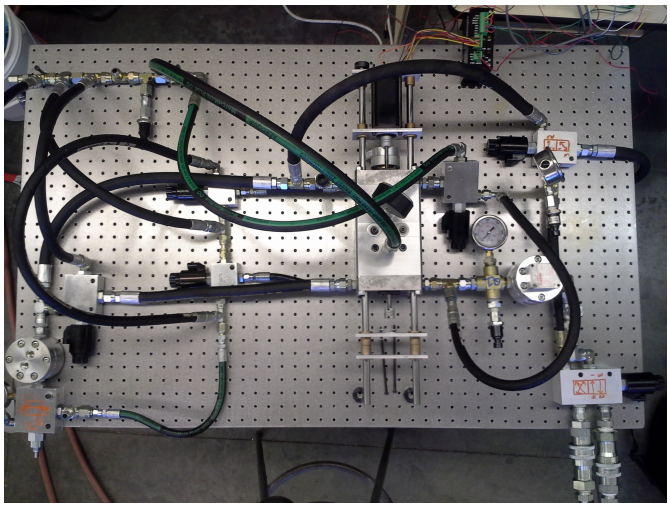

Figure 4.1: Experimental test bench used for investigating transition events

4.2 Control Approach

As it was necessary to have closed-loop control, a controller was designed, but this investigation was not intended to focus on the performance of the controller. The timescale of the response to the transition effect is strongly dependent on the bandwidth of the swashplates, which is in turn dependent on the design of the actuation method for the swashplates. As this was a prototype, the swashplate actuators were not optimized, and the timescales of the transition events are not representative of what a commercial machine could achieve.

The control method used in this chapter is shown in figure 4.3. The approach

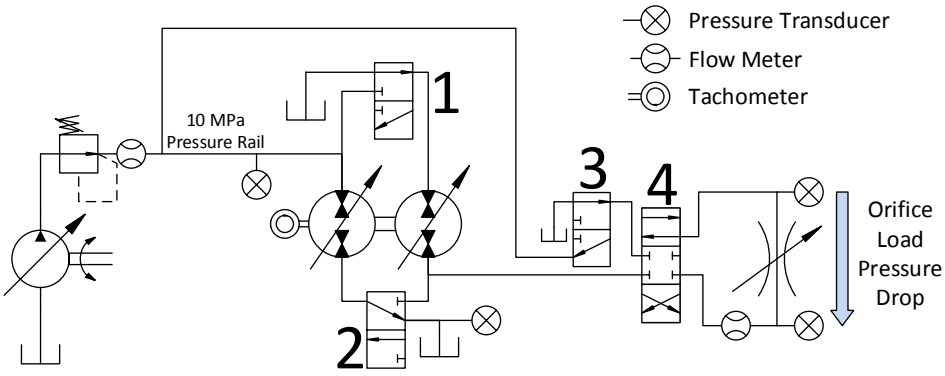

Figure 4.2: Hydraulic circuit used for investigating port switching behavior

can be considered to have three elements that determine the displacement commands for the rotating groups, the frequency and direction commands for the stepper motors controlling displacement, and a set of digital signals controlling the valve states that determines what configuration the transformer is in.

First Control Element: κ Controller κ is a single dummy variable that is bounded by $\kappa \in (0, 2)$ and maps to two positive command variables u_1 and u_2 that state the desired displacement of the two rotating groups of the transformer. Therefore the first element of this simple control scheme is a proportional-integral controller that implicitly determines the instantaneous value of κ based on the combined instantaneous error and error history of the desired pressure drop across the orifice load as compared to the actual pressure drop across the orifice load. The relationship between the κ term and the displacement commands is:

$$u_1(\kappa, t) = \begin{cases} \kappa(t) & \kappa(t) < 1 \\ 1 & \kappa(t) \geq 1 \end{cases} \tag{4.1}$$

$$u_2(\kappa, t) = \begin{cases} 1 & \kappa(t) < 1 \\ 2 - \kappa(t) & \kappa(t) \geq 1 \end{cases} \tag{4.2}$$

Conceptually, the κ controller always holds either one of the two displacement commands at maximum displacement, while the other command is adjusted to achieve a

displacement ratio that results in the desired pressure drop across the orifice load. Refer to section 2.5 for a complete discussion of the motivation and assumptions of such a control approach. It should be noted that this controller will not result in either of the rotating groups going over-center. This is not a necessary limitation, and a different controller could operate the machine in this regime.

Second Control Element: Two Displacement Controllers The second section of the control approach includes two proportional-integral controllers that determine the behavior of the two stepper motors that control the rotating group displacements. The inputs for the two PI controllers are the u_1 and u_2 commands determined by the κ controller. The controller outputs are a frequency and a direction command for each of the two stepper motors based on the instantaneous error and error history between the desired displacement and actual displacement of the rotating groups, as determined by the integrated travel of the stepper motors.

Third Control Element: Valve State Commands through Port Map The third element of the control approach is the determination of the valve state commands that dictate which configuration the transformer system is in. The four valve commands are a function of the desired load pressure drop command and measured instantaneous flow rate, and are obtained from a lookup table that contains the information displayed in the porting map shown in figure 4.5. This element of the controller ensures that the valves are set such that the transformer system is operating in whichever configuration was characterized as the most efficient for the current operating point. The specific valve settings to achieve each mode shown in figure 4.5, for the particular machine under consideration, was previously given in table 3.3. The action taken to switch a valve varies depending on the valve's design, but for the valves used in this experiment, switching was achieved by increasing the current through a solenoid that created a strong magnetic field in a manner that resulted the valves mechanical components switching states.

It should be noted that this controller is purely reactive, meaning that it contains no feedforward elements. A more advanced controller would have a feedforward element that anticipates the characteristics of the events caused by transition between transformer configurations, and takes action to minimize spikes or dips.

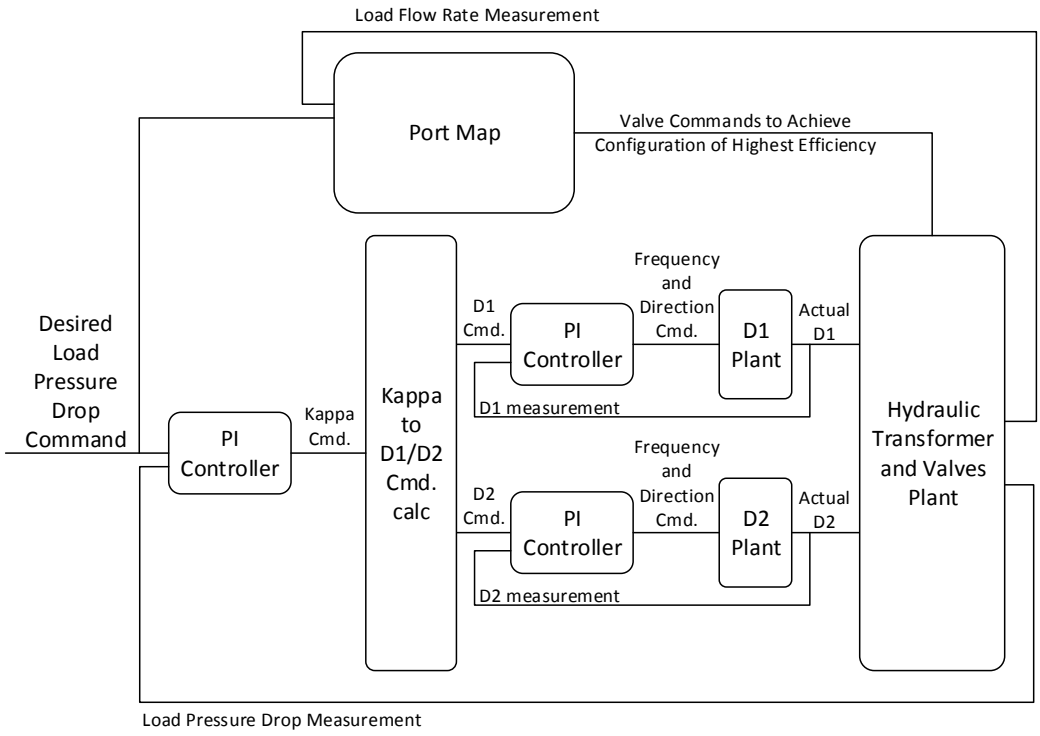

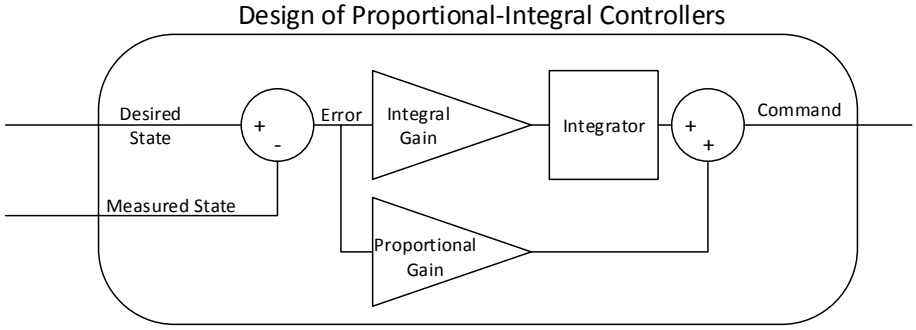

Figure 4.3: Control approach used for port switching investigation

4.3 Generation of the Porting Map

It was of interest to investigate the transitions between configurations that would likely occur during practice. To determine which transition events could occur, it was necessary to experimentally characterize the prototype transformer and generate its porting map. The concept of a porting map is described in section 3.10, and the process of obtaining a set of steady state operating points and combining them into a composite performance map is described in section 2.5, where the only difference for this study is that the steady state values were obtained experimentally and not through simulation. This effort did not utilize the controller described in section 4.2, as the unit is characterized by the collection of a set of steady state operating points whose acquisition did not require the use of a feedback controller.

A porting map shows the regions where each configuration was most efficient throughout the entire transformer operating region. Therefore such a map can be used to determine which configurations are neighbors on the porting map. From this, a set of trajectories was selected that would prompt transitions between neighboring configurations on the port map for the prototype transformer. The efficiency map for the prototype transformer and the accompanying porting map are shown in figure 4.4 and 4.5 respectively. For a complete discussion of how the maps were generated and their interpretation, refer to section 2.5. Lines A through D show the trajectories that were experimentally explored during this investigation. Due to limitations in the experimental setup it was not possible to create an over-running load, and therefore the regenerative quadrants 2 and 4 were not investigated. Trajectories A, C, and D were all performed in the first quadrant of operation, however, if the four-way valve shown in figure 4.2 was activated the same behavior would be observed in the third quadrant. This is illustrated in figures 4.4 and 4.5 by the lines in the third quadrant showing what trajectories would be traced out if the four-way valve was activated.

4.4 Port Switching Transition Event Results

Figure 4.5 shows the trajectories investigated in this chapter overlaid on the porting map for the prototype transformer used in this study. The trajectories visually indicate which transition events will be explored. All of the trajectories ramp from one level of

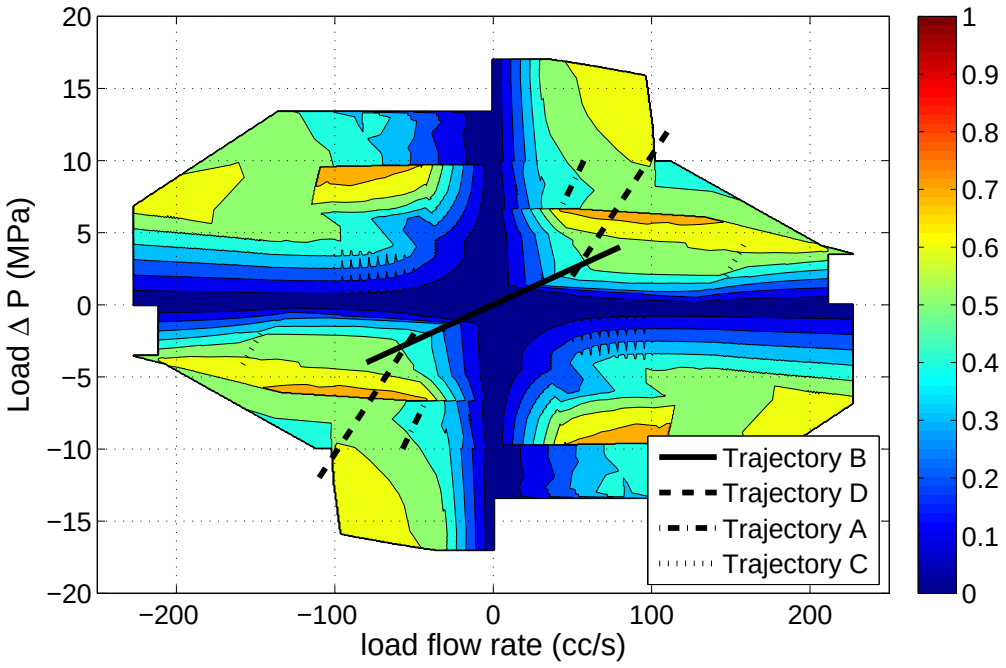

Figure 4.4: Composite efficiency map of the prototype transformer, with lines A - D showing approximate trajectories explored in this chapter

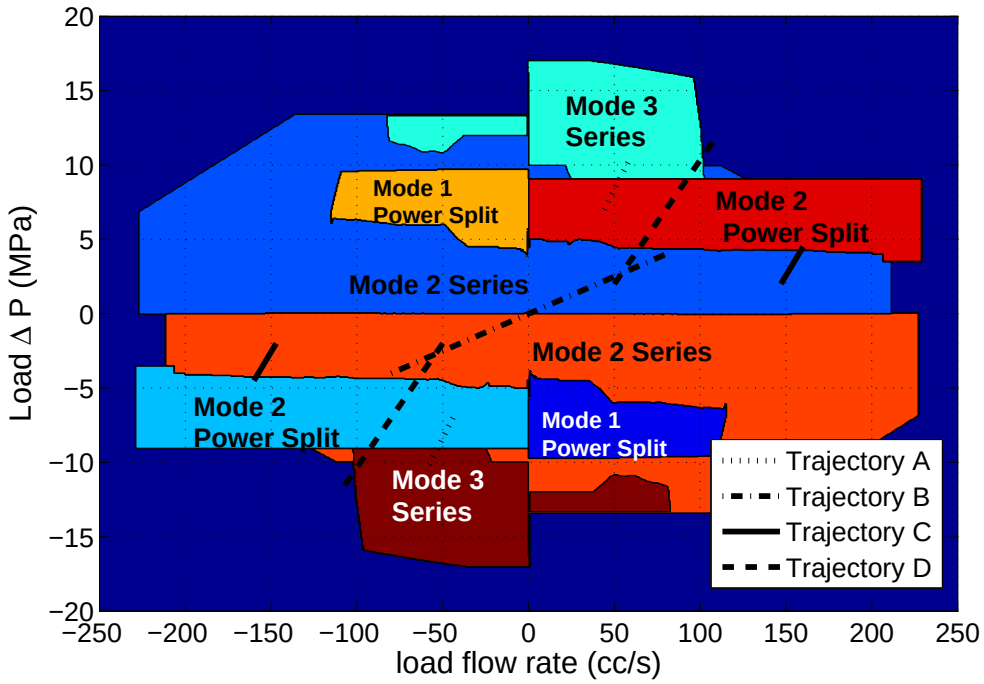

Figure 4.5: Porting map of the prototype transformer, showing which configuration is most efficient for each operating region. Lines A - D show approximate trajectories explored in this chapter

load pressure drop to another load pressure drop. The transition between configurations occurs during the ramps when the controller described in section 4.2 observes from the current load pressure drop command and measured flow rate that the relevant port map boundary has been crossed and correspondingly switches the valve states.

Note that each trajectory is shown twice, with one of the instances containing a directional arrow. There are two instances because a simple four-way valve can flip the sign of both the pressure drop and flow rate across the load connected to the transformer. Therefore, any of the trajectories explored in this section can be meaningfully said to characterize the events of both instances shown in 4.5. The presence and direction of the arrows indicate which trajectories are plotted in figures 4.6 through 4.9.

Figures 4.6 through 4.9 all take the same form. Subplot 1 shows the relationship between the desired load pressure drop given to the controller and the actual pressure drop across the load achieved by the system. Subplot 2 shows the transformer shaft speed. Subplots 3 and 4 show the relationship between the desired displacement command sent to each of the swashplate subsystem controllers and the actual displacement achieved by the subsystems. The shaded regions illustrate what configuration the system is in, as indicated in each plot.

It should be noted that the characteristics of these transition events are strongly dependant on the attributes of the system itself. Throughout this chapter the load is an orifice with very small energy storage capacity in the compressibility of the load line. The results seen here are different than what would be observed if an accumulator was attached to the load line, or if the load was an actuator of some type. The following section 4.5 contains a discussion of the implications of the system type on the characteristics of the transition events.

Trajectory A: Figure 4.6 shows the transition between mode 3 series configuration and the mode 2 power split configuration, illustrated by line A on figure 4.5. Valves 1, 2, and 3 must switch during this transition, as given in table 3.3. The sensitivity of performance to the relative timing of the valve switching was not characterized, and would be dependent upon the design of the machine. The trajectory starts at 10.35 MPa and ramps down to 7 MPa over the course of 20 seconds, with the transition between configurations occurring at approximately 8.2 MPa. As a result of the change of configuration the transformer shaft speed changes from 100 rad/s to -60 rad/s, with

the change taking approximately 0.2 seconds.

The change from a series to a power split configuration results in a sudden drastic dip in the pressure drop observed by the orifice load. The pressure drop across the orifice load is a function of the flow rate through it, and since the flow rate is directly proportional to the transformer speed, the dip in the pressure drop is an expected result of the transformer speed change. The pressure recovers to be within 95% of the desired value within 0.3 seconds. As the direction of rotation changes, there is necessarily an instant where the pressure drop across the load is zero.

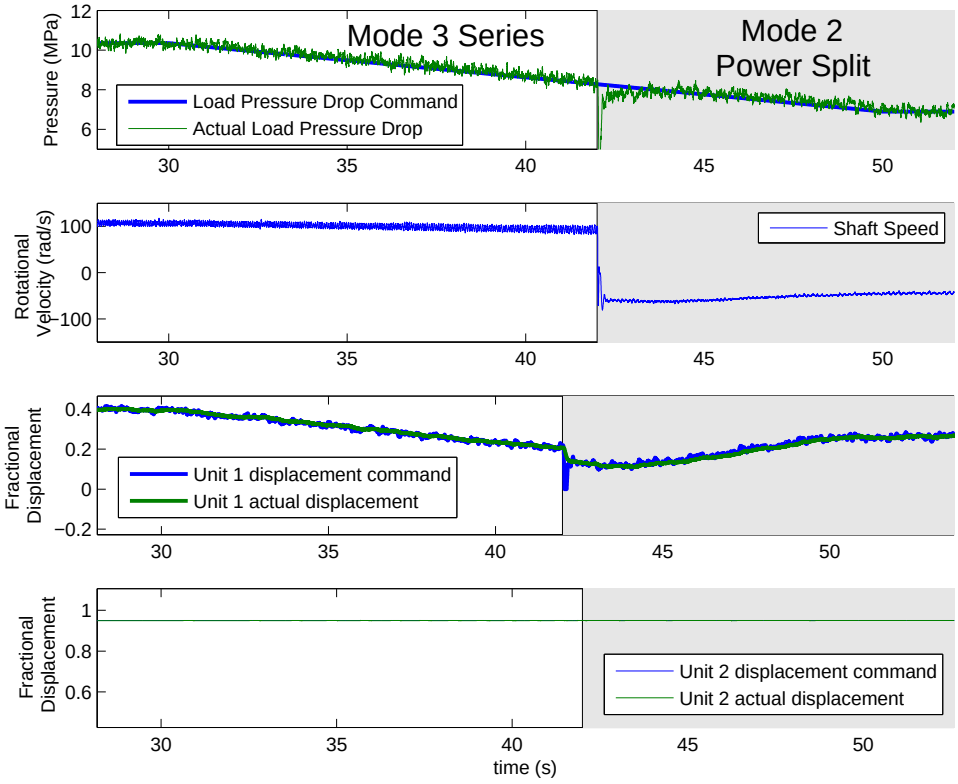

Figure 4.6: Transition event between mode 3 series configuration and mode 2 power split configuration, corresponding to line A on figure 4.5

Trajectory B: Figure 4.7 shows the transition event where the trajectory passes through the origin of the porting map, illustrated by line B on figure 4.5. The trajectory

starts at a load pressure drop of 4 MPa with a load flow rate of 40 cc/s and ramps down to a load pressure drop of -4 MPa with a load flow rate of -40 cc/s. Note that both the pressure drop and flow rate signs switch to negative at the same point, result in a positive product during the entire trajectory. This indicates that the load is always consuming power, not regenerating it.

The transition through the origin is achieved entirely within the mode 2 series configuration, with no switching to different modes. The displacement of unit 1 is lowered until the measured pressure drop across the orifice load is zero, then the four-way valve of figure 4.2 is inverted to its second position. This reverses the direction of fluid flow and pressure drop across the load, and the displacement of unit 1 is raised to continue tracking the trajectory. As the transition event did not prompt a large change in transformer speed, and the valve transition occurred when the load flow rate was approximately zero, no spike or dip in the pressure drop across the load was observed.

Trajectory C: Figure 4.8 shows the transition between mode 2 series configuration and the mode 2 power split configuration, illustrated by line C on figure 4.5. Only valve 3 must switch states during this transition, as given in table 3.3. The trajectory starts at 3.8 MPa and ramps up to 6 MPa over the course of 20 seconds, with the transition between configurations occurring at approximately 4.4 MPa. As a result of the change of configuration the transformer shaft speed changes from 200 rad/s to -100 rad/s, with the change taking approximately 70 milliseconds.

Similarly to what was seen in trajectory A, the change from a series to a power split configuration and resulting change in direction of rotation of the transformer prompts a sudden and brief dip in pressure drop observed by the load, as a result of the change in flow rate of the load line. The pressure drop decreases to approximately atmospheric pressure, but recovers to 95% of the desired value in 0.14 seconds.

Trajectory D: Figure 4.9 shows the trajectory illustrated by line D on figure 4.5, except where the mode 2 power split region was replaced by mode 1 series configuration. This was done to explore a ramp through the three series configurations, covering a large pressure range. The system starts in mode 2 series, transitions into mode 1 series, and then transitions into mode 3 series. The trajectory starts at a load pressure drop of 2 MPa, and then ramps up to 14 MPa with the transitions occurring at 5 MPa and 8.3 MPa. Valve 2 must switch states during the first step of this trajectory, and valve 1

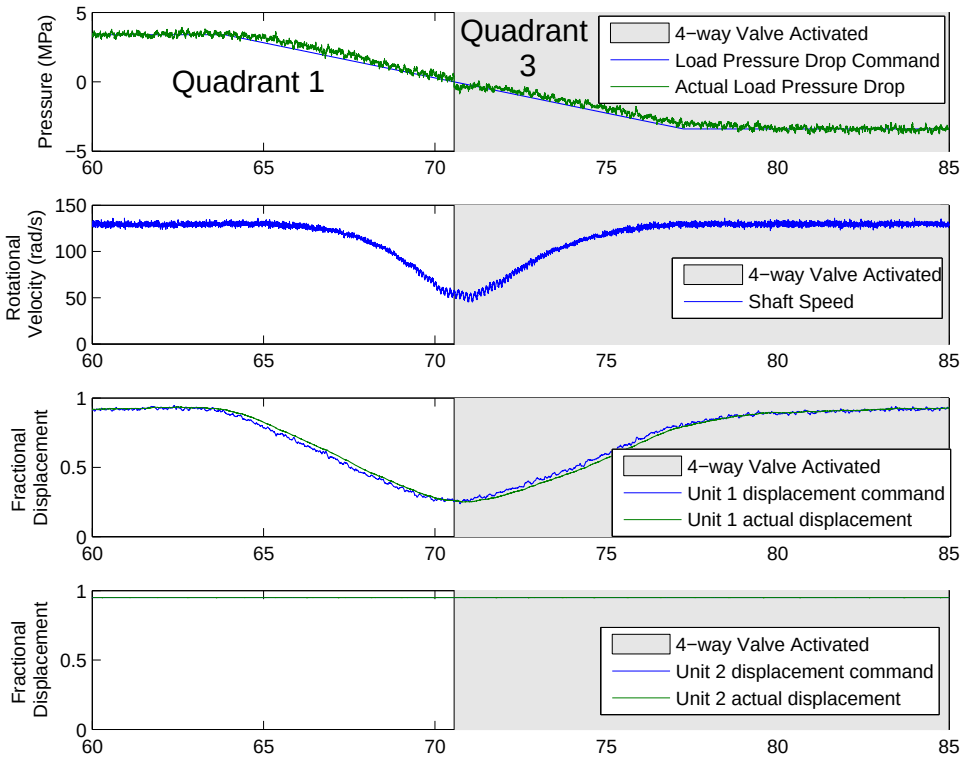

Figure 4.7: Transition event through the origin, corresponding to line B on figure 4.5

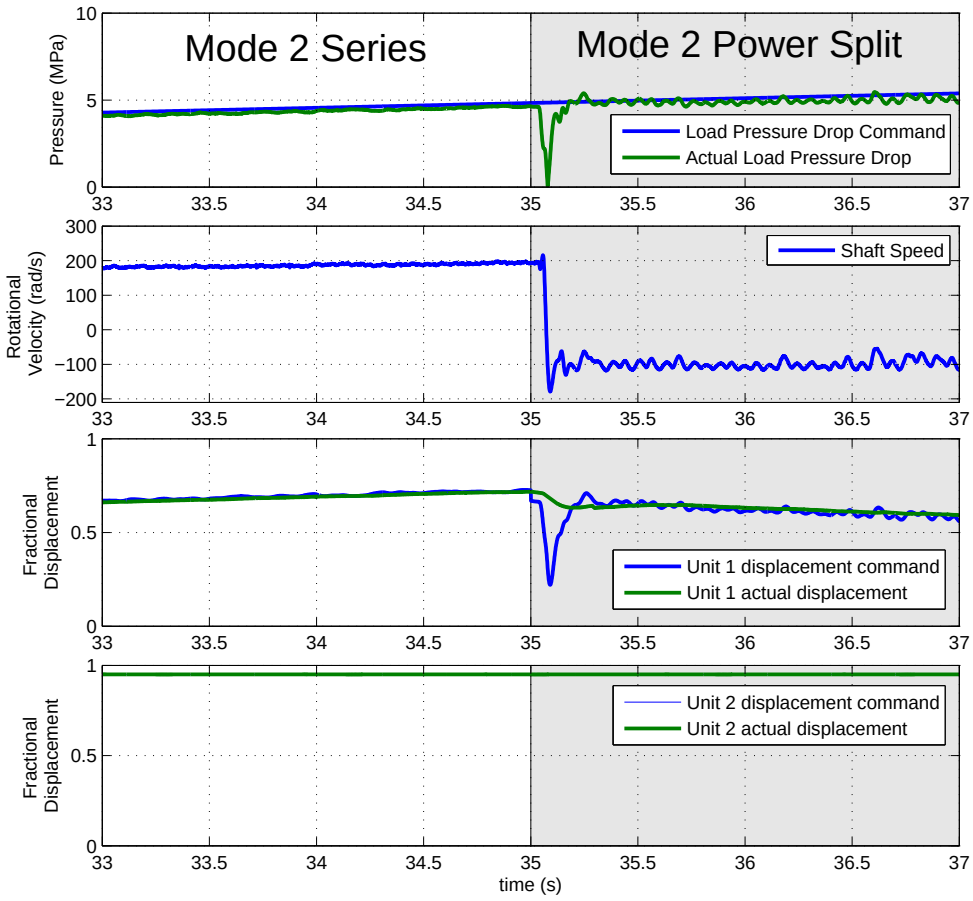

Figure 4.8: Transition event between mode 2 series configuration and mode 2 power split configuration, corresponding to line C on figure 4.5

must switch states during the second step of this trajectory, as given in table 3.3.

It can be seen that the transition events of this trajectory experience a very small and brief dip in the pressure drop observed across the load followed by a large spike. Additionally, there is a large spike in the shaft speed of the transformer with no change in direction of rotation, in contrast to the load pressure drop dips and change of direction of shaft rotation that were observed in trajectories A and C. This can be understood by examining the changes in fluidic connections resulting from each transition's valve switch. As the behavior of this trajectory serves as a good platform for understanding the system characteristics, it will be examined closely in the following discussion section.

4.5 Discussion of Port Switching Transition Events

The trajectories shown clearly demonstrate that it is possible to switch between various configurations of a hydraulic transformer during operation through the use of valves. This has significant value, as it allows a traditional transformer to operate in the configuration that is most suitable for whatever objective it is trying to achieve at any given moment, most often but not limited to the maximization of efficiency.

The four trajectories that are shown were repeatable, and could be performed consistently without having the transformer stop rotating, an effect conventionally called stalling. Many transition events could not be explored successfully, however, with the basic controller used in this investigation. A transition was typically unsuccessful if the current displacement settings during the transition would result in the transformer stalling once the new configuration had been engaged and new pressures exposed to the ports. Once the transformer stalled, the loss of hydrodynamic lubrication throughout the rotating groups would often make it such that the torque moments of the pistons were insufficient to overcome the large static friction and resume motion.

As stated earlier in this chapter, the characteristics of the transition events are a strong function of the physical nature of the system and the control approach. In this study the load is an orifice with negligible energy storage capacity in the load line, and the controller is a simple proportional-integral controller with no feedforward behavior. The implications of such system features can be understood by examining trajectory D more closely. Figure 4.10 shows trajectory D magnified on the transition event between

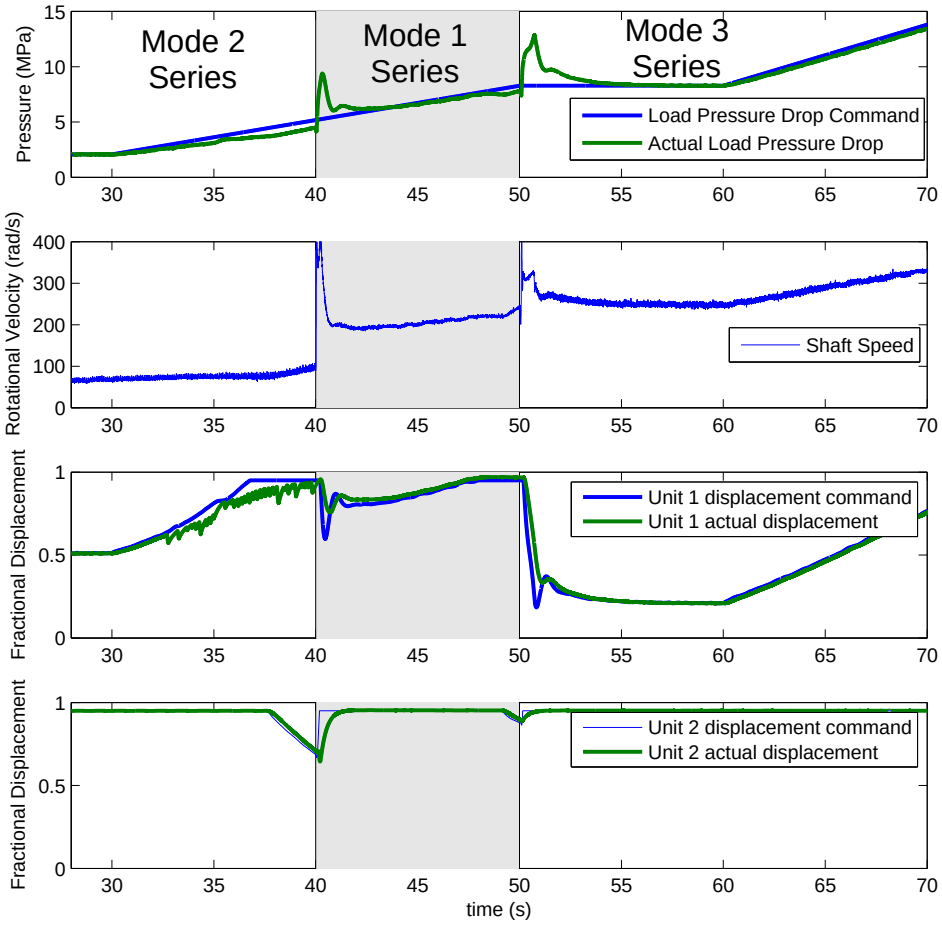

Figure 4.9: Transition events between mode 2 series configuration, mode 1 series configuration, and mode 2 power split configuration, corresponding to line D on figure 4.5

the mode 2 series and mode 1 series configurations.

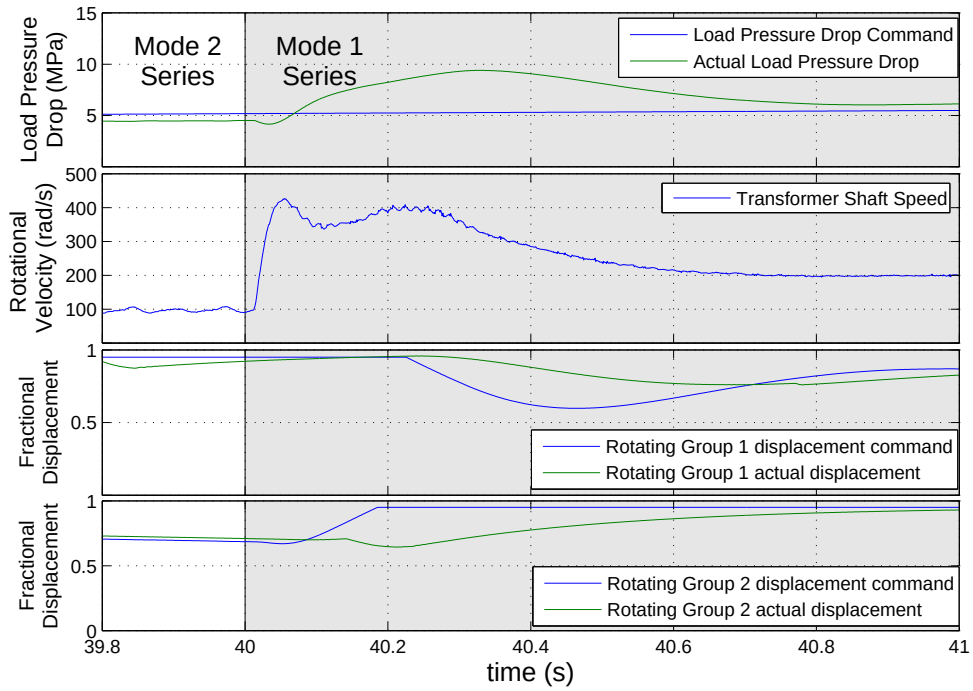

Figure 4.10: Transition event between mode 2 series configuration and mode 1 series configuration

The transition from mode 2 series to mode 1 series is achieved by changing valve two from its activated state to its default state, as seen in figure 3.11 and stated in table 3.3. The valve switch results in the output port of the first rotating group rapidly changing from a fluidic connection with the load line to a connection with the tank line. Such a change results in the first rotating group no longer contributing to the output load flow rate generated by the transformer, as well as the pistons on the output half of the first rotating group becoming exposed to tank pressure and therefore decreasing their resistive contribution to the transformer's torque balance. The sudden decrease in flow rate results in a dip in the pressure drop observed across the orifice load, but the effect is very brief as the unloading of the pistons results in a net torque that quickly accelerates the rotation speed of the transformer and increases the flow rate past the levels prior to the switch. As the system is loaded by an orifice, the increase in flow rate results in an increase in pressure beyond the level desired by the trajectory, and

the controller correspondingly reacts to adjust the displacements until the torque of the machine is balanced at an output pressure that achieves the desired pressure drop across the load.

The characteristics of the transition response described above depends on system and load attributes. As the load used in these experiments was always an orifice, the pressure drop across the load was a function of the instantaneous flow rate through it. This dependency caused the fluctuations in pressure observed in figure 4.10. The first small dip in load pressure drop observed between 40.0 s and 40.05 s was a combined result of the changed fluidic connections of the ports and inertia of the transformer rotating group. The second larger increase in load pressure drop, lasting until approximately 40.8 s, was due to the new torque balance of the transformer, as the controller responded to the transition event by reducing the displacement of unit 1. The response characteristics would be different for a situation where the load pressure drop was a less strong function of the instantaneous load flow rate. For example, such a situation could be achieved either by replacing the orifice with a loaded actuator. An ideal actuator would have a pressure drop entirely dependent on the imposed forces, completely decoupled from its instantaneous velocity. In such a situation there would be no fluctuations in pressure during the transition. The load flow rate would still fluctuate, as the non-zero net torque of the transformer produced by changing the connection of a port from the load line to the tank line would have to be absorbed within the transformer itself through viscous losses until the controller was able to adjust the unit displacements to appropriate levels. The pressure drop across an actual actuator in practice is a typically a strong function of the imposed forces and a moderate function of the velocity of the actuator, meaning that the response would likely be a combination of what was experimentally observed and what was described above for an ideal actuator.

There are several general options that could be investigated as potential routes to mitigating or eliminating the spikes in pressure during transition. If the load on the system is of the type that has a flow rate dependant pressure drop, such as an orifice or machine with viscous drag loss contributions, the transition spikes could be dampened by the introduction of an accumulator as a fluid and energy storage device on the transformer load line. The accumulator would serve to decrease fluctuations in the load line pressure, analogously to a low pass filter, by passively absorbing fluid from the line

if pressure increased or ejecting fluid into the line if pressure decreased. This behavior would partially decouple the flow rate through the load from the load line flow rate of the transformer, partially isolating the load from spikes and dips in the transformer states. Such a change would potentially come at a cost of less responsive control, as the system would be made less stiff.

Another option that could benefit any type of system is to develop some type of feedforward controller that anticipates transition events and moves the unit displacements into a configuration that facilitates a smoother jump, temporarily superseding the controller that normally keeps the displacements in a position to maximize efficiency.

A third option is in the design of the swashplate actuators. The valve switching that produces the change in configuration occurs on timescales of tens of milliseconds. If the swashplate actuation occurs on a similar timescale, it would be possible to adjust the displacements during the valve transition, resulting in a much smoother event. It would be necessary to pair this with a feedforward controller that knows the adjustment that must take place during the transition, as the development of an error signal to drive a simple closed loop control would only occur after the valve transition, and the intention would be to have such action taking at the same time the valve transition.

A fourth option for mitigating the transition spikes and dips would be to design a custom valve that plays a more involved role in the configuration transition itself. The valves used in the investigation of this chapter were simple directional valves whose function was to quickly transition between different fluid routing options with no effects beyond the transition. As an example, it would be possible to design a valve that temporarily throttles the output flow slightly immediately after a transition, in a manner that negates a pressure spike that would otherwise happen. Such an approach would depend on the transition spikes being of predictable shape and magnitude.

4.6 Chapter Summary

This chapter explored the performance of a prototype transformer in transitioning between various configurations while tracking a pressure ramp trajectory. A set of trajectories were identified that could be performed reliably, but a number of transition events were found to be impossible with the current experimental setup and basic controller, as

the machine would stall during the transition and be unable to recover. It was suggested that a more advanced controller could anticipate the transition event and prepare the transformer by adjusting the displacements of the units such that the device would not stall during the switch.

All of the transition events that involved changing the porting connections of the transformer were observed to have pressure and speed spikes and dips immediately after the valve positions were switched. It was suggested that a more advanced controller, faster displacement actuators, or custom valves could reduce the magnitude of the spikes. It was shown that the transformer was capable of rapidly changing its speed during transitions, including events that changed the direction of rotation, due to the relatively small rotational inertia of the machine.

This chapter confirmed that a port switching transformer can be realized in practice. The confirmation has value in validating the use of composite efficiency maps to evaluate the potential of a transformer, as such maps implicitly assume that the base transformer would be capable of switching its configuration. Chapter 5 and 6 present case studies that take the analysis of a port switching transformer further, presenting the optimization and performance of such a machine in a case study of hydraulic power distribution within a humanoid robot.

Chapter 5

Optimal Sizing: Humanoid Robot Case Study

5.1 Chapter Overview

Increasing the efficiency of a power distribution system decreases the energy consumption necessary to achieve the desired behavior of the system. Therefore, in a hydraulic transformer based power distribution system, it is desirable to minimize the losses in the transformer. The efficiency of a hydraulic transformer at a given operating condition is strongly dependent on the fraction of maximum displacement that the two internal rotating groups must be at in order to achieve the specified performance. This presents an opportunity to optimize the size of the rotating groups to maximize efficiency for a particular application. There has yet to be an investigation of the performance of a transformer with unequally sized rotating groups, as existing literature only considers units consisting of rotating groups of equal size. The two design parameters varied in this study were the maximum displacements of the two rotating groups, and the following results will show the efficiency of a given set of trajectories as those two parameters are varied.

The leg actuators of a humanoid robot were chosen as a case study due to the highly varying pressure and flow requirements of their actuators and the availability of a duty cycle through human gait data. Optimal displacement sizes were identified by an initial coarse search of a large region, refined by a gradient search once the general shape of

the design space was known. Optimal maximum displacements were identified for the hip, knee, and ankle actuators of the humanoid robot. Optimal sizes varied significantly across the three actuators, with both the knee and ankle optimal solutions departing significantly from rotating groups of equal sizes.

5.2 Motivation for Investigating Optimal Rotating Group Sizes

The efficiency of a variable displacement hydraulic pump/motor operating at a particular flow and pressure is dependent on both the maximum displacement of the unit as well as the fraction of the maximum displacement necessary to achieve the desired outputs. Figure 5.1 shows a representative relationship between the size of a hydraulic pump/motor and its maximum efficiency, and figure 5.2 shows the effect of varying the displacement fraction on the efficiency of a hydraulic pump/motor. Both plots are for a pump discharging hydraulic oil at 30 cc/s at a pressure of 20.7 MPa [3000 psi] and were generated using the dynamic loss model described in chapter 2.

Figure 5.1 shows a monotonic trend of decreasing maximum efficiency as the maximum displacement of a hydraulic pump/motor is decreased. Figure 5.2 shows a monotonic trend of decreasing efficiency as fractional displacement is decreased. These two trends result in a tradeoff, where increasing the size of a rotating group would tend to increase its efficiency in general, but would often result in the unit operating at a lower displacement fraction for a particular operating point, decreasing the local efficiency. The interaction of these two trends for the two rotating groups of a hydraulic transformer is complex, and the result is non-obvious. Current hydraulic literature has not investigated optimal sizing of a transformer.

In addition to investigating the relationship between efficiency trends, a study on transformer sizes would explore the impact of unequal rotating group displacements. This question is motivated by the fact that a main objective of a transformer is to transform hydraulic pressure and flow variables, which is achieved by unequal displacement ratios. If there is prior knowledge of the duty cycle a transformer will be subjected to, there is an opportunity to design the sizes of the rotating groups such that they are near full displacement in operating regions that pass the greatest quantity of energy

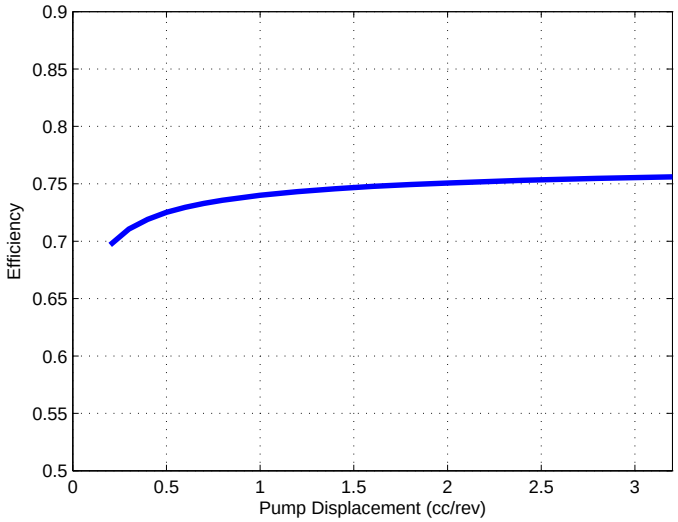

Figure 5.1: Relationship between maximum efficiency of a hydraulic pump and its total displacement

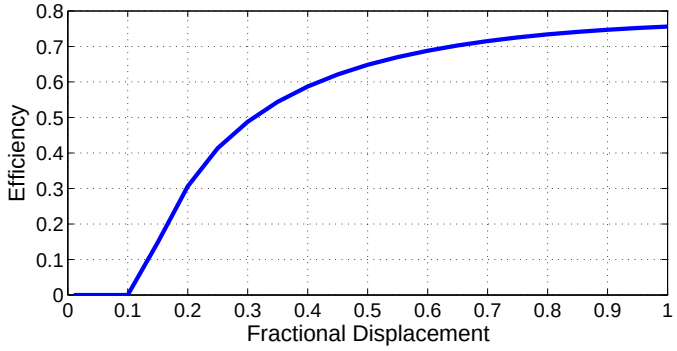

Figure 5.2: Impact of fractional displacement on the efficiency of a 3.15 cc hydraulic pump

over the course of the cycle, increasing the weighted average efficiency for that duty cycle.

5.3 Description of a Humanoid Robot System and Duty Cycle

In order to size the rotating groups of a transformer, it is necessary to have some knowledge of the system and the duty cycle that the machine is being optimized for. As discussed in chapter 1, an application is more likely to be suited for a hydraulic transformer power distribution architecture if it consists of multiple linear actuators that require highly varying pressure trajectories over a typical duty cycle. The system chosen as a case study to demonstrate the optimization method is a humanoid robot, where linear actuators are used to drive the hip, knee, and ankle joints of the robot. Figure 5.3 shows an example of such a hydraulically actuated robot.

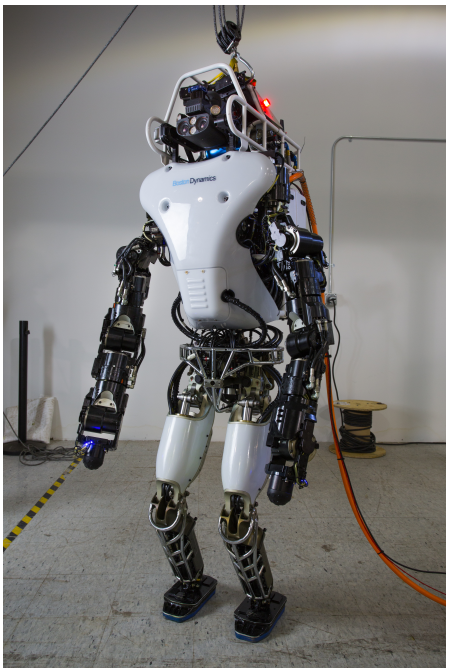

Figure 5.3: Example of a hydraulic humanoid robot

Figure 5.4 shows the hydraulic circuit used in this case study. The system consists

of a hydraulic pump that serves as a prime mover, the linear actuators that control the joints, and the hydraulic transformers and associated valves. Note that an assumption was made for this case study that the rail pressure would be constant at 20 MPa. This is a restrictive assumption, as efficiency performance could be improved by allowing the rail pressure to vary depending on the instantaneous operating conditions of the transformer and actuator systems, in a manner similar to existing load sensing architectures. Due to the computational intensity of adding another dimension to the design space of the study, a variable pressure rail was not analyzed in this thesis. A discussion of the potential improvements of allowing the rail pressure to vary is given in section 5.8.

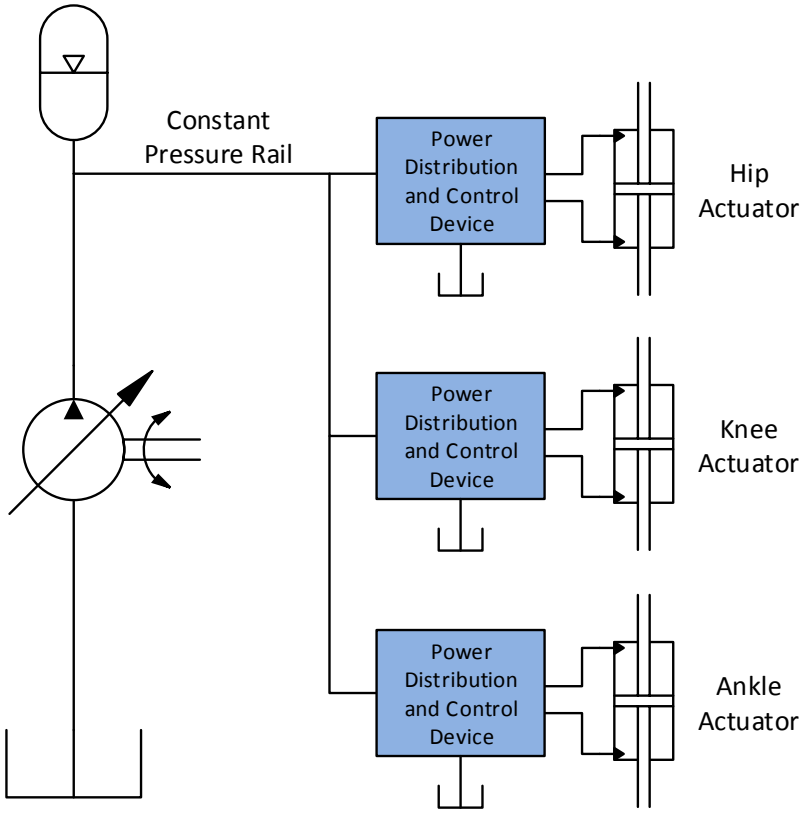

Figure 5.4: Schematic of common pressure rail hydraulic power distribution system

The linear mechanical power output of the actuator was changed into the rotational

mechanical power required by the joints by a mechanism of similar design to a hydraulic ankle-foot orthosis currently under investigation at the University of Minnesta [45]. The approach was modified to a single double-sided actuator to allow the system to absorb an overrunning load. A mechanical-hydraulic schematic of the design modelled in this case study is shown in figure 5.5. The mechanism was chosen for its constant mechanical advantage regardless of rotation angle, compactness, and simplicity.

Duty cycles for the hip, knee, and ankle joints of the humanoid robot were obtained from human angular kinematic data for a typical walking gait, shown in figure 5.6. The angular kinematic data was in the form of the required torque and angular velocity throughout the cycle. As the mechanism shown in figure 5.5 transforms linear mechanical power to rotational mechanical power, it was possible to obtain the force and velocity trajectories of the hydraulic actuator that would be necessary to achieve the torque and angular velocities demanded by the duty cycle.

$$F_a(t) = \frac{T_a(t)}{r_d} \tag{5.1}$$

$$v_a(t) = \omega_a(t) r_d \tag{5.2}$$

where r_d is the radius of the disk that serves as a moment arm for the mechanism, as seen in figure 5.5. As will be discussed more completely in section 5.5, the mechanism is underconstrained, and therefore both the disk radius r_d and the cross-sectional area of the actuator were free variables that could be adjusted to change the shape of the required fluid power trajectory. As this investigation did not consider the form factor of the solution, it was only necessary to vary one of the two free variables to manipulate the shape of the power trajectory. Therefore, the disk radius r_d was fixed at 5 mm for the simulations in this thesis.

The equations (5.1) and (5.2) assume no mechanical losses and no volumetric losses, respectively. This assumption of ideal power transformation within the joint mechanism was made in order to isolate the results of the study to the impact of a hydraulic transformer on the efficiency of power distribution. This assumption is in line with the assumption of ideal hydraulic lines, valves, and actuators as already described. Focusing on the performance of a power distribution technology alone eliminates the

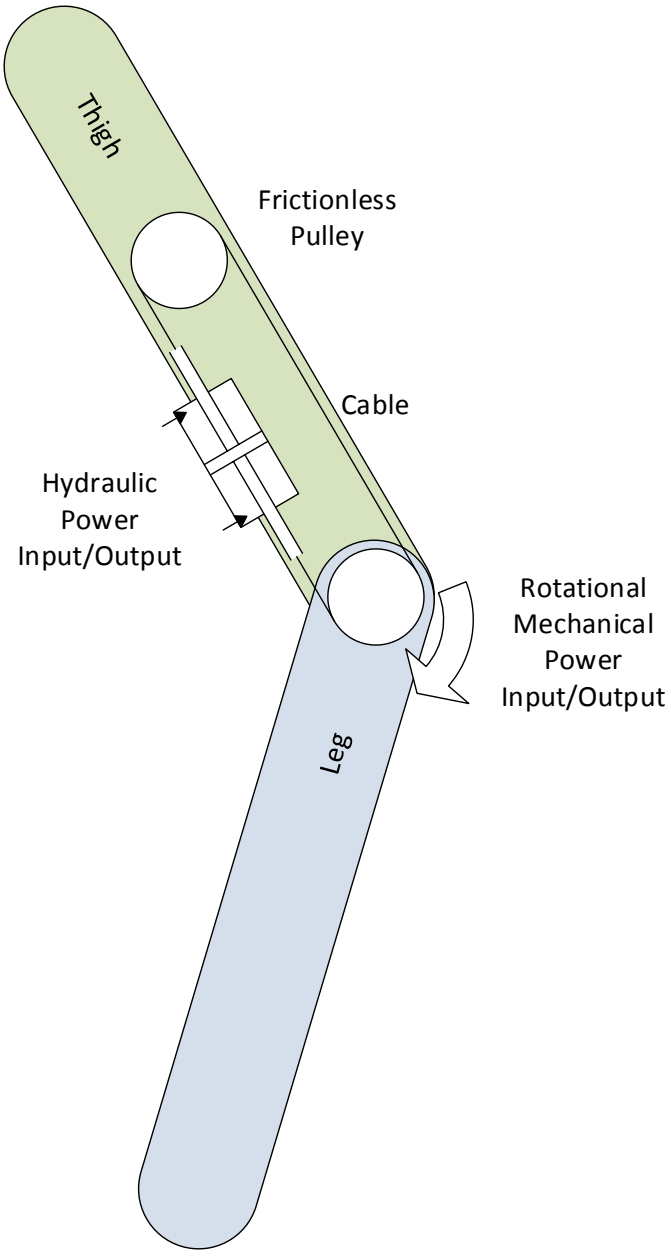

Figure 5.5: Hydromechanical actuator for humanoid robot joints

need to make a large number of design assumptions that can hinder fair comparison against other competing technologies.

Figure 5.6 shows the torque and angular velocity profiles used in this case study [46]. Figure 5.7 shows the force and velocity requirements of linear actuators covering those duty cycles through the mechanism shown in figure 5.5.

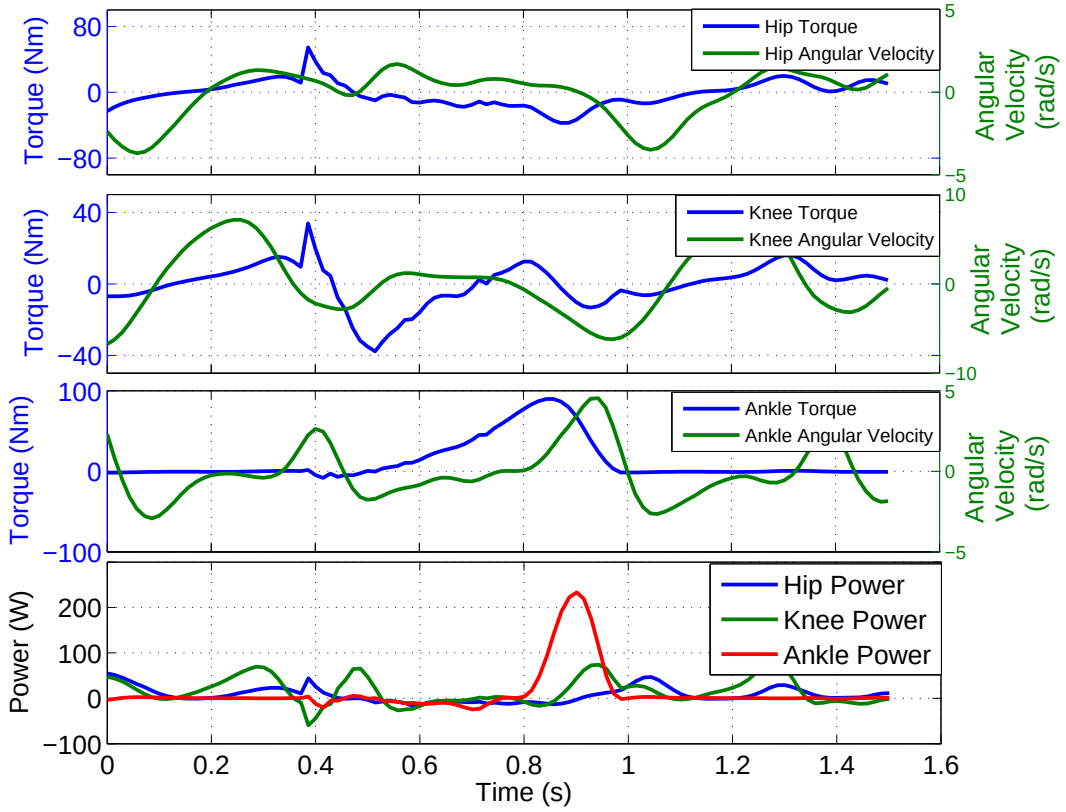

Figure 5.6: Torque and rotational velocity demand profiles for hip, knee, and ankle joint of humanoid robot

There are three features of the humanoid robot trajectories show above that suggest them as a good potential application for power distribution through hydraulic transformers. The first feature is that the required torque varies significantly through the cycle, usually with a clear peak at a single point and the majority of the operation at torque levels much different than the peak. If the system mostly cycles between its peak and being off, then the system can be designed to efficiently operate at those two

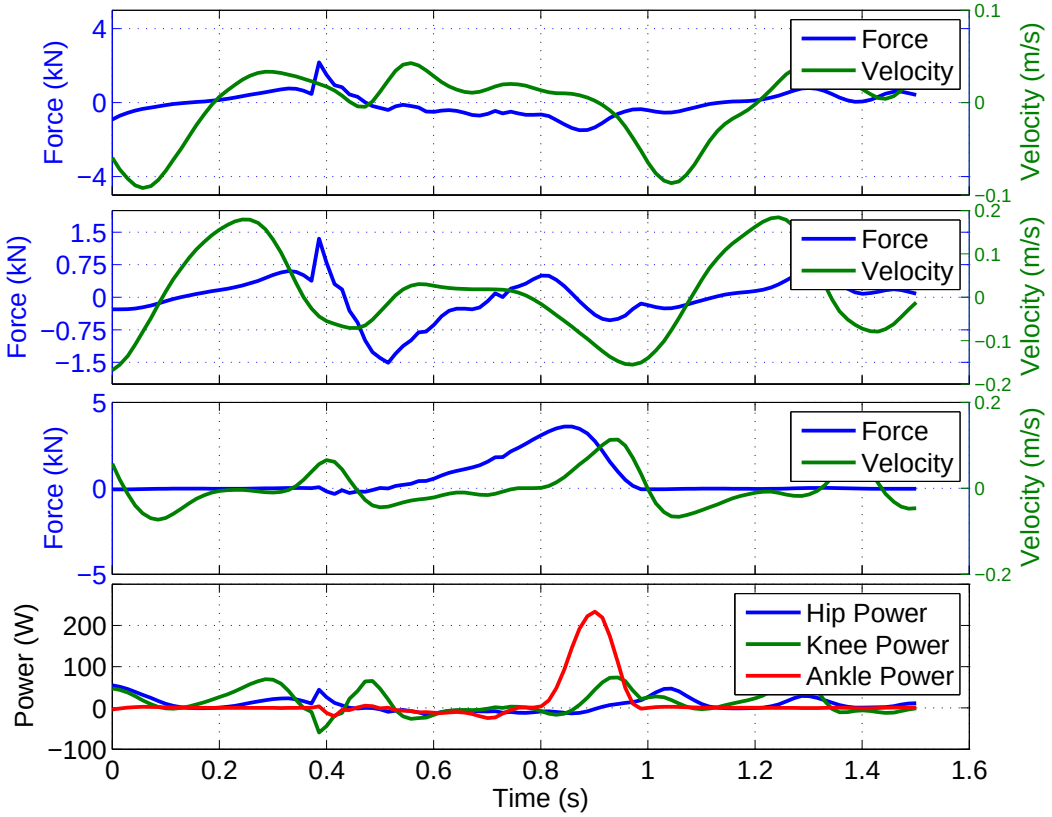

Figure 5.7: Force and velocity demand profiles for hip, knee, and ankle joint of humanoid robot

points, and the ability to transformer efficiently between the points would not be of much values.

Secondly, the velocity peaks and torque peaks are not aligned in these trajectories. If they are, then the majority of the energy transfer will occur at and near the peaks, and efficient off-peak operation will not be of significant value.

Thirdly, there are opportunities for regenerating energy back into the system from the load. Traditional control approaches with throttling valves could not capture this potential energy. This makes a transformer approach, which can regenerate energy back into the rail, more attractive from the standpoint of total system efficiency across the entire trajectory.

5.4 Evaluating Total System Efficiency of a Trajectory for a Given Performance Map

The evaluation of the total system efficiency for a trajectory is similar to the derivation for the efficiency of a single point of operation as given in section 3.4, but with a few important differences. In order to properly capture the characteristics of the humanoid robot system under study, the fluid and mechanical power flows must be treated differently.

The net fluid power is determined over the trajectory, and the result is applied either to power input or power output depending on the sign of the result. This is to represent the energy storage ability of an accumulator connected to the rail line, as shown in figure 5.8. The ability to store energy allows a system to store useful output fluid power to directly offset required input fluid power at a different point in time, making a summed treatment of the power flows reflective of the total efficiency of the system over a span of time. This assumes that the capacity of the accumulator is sufficient to store the maximum value of regenerated energy for the duty cycle.

In contrast, there is no meaningful energy storage in the mechanical domain. To reflect this the integrated mechanical power streams are not summed, and are applied to the power input and power output values as their signs dictate.

As with the single point efficiency, the useful power flows are the fluid power of the common pressure rail and the mechanical power of the actuator, as shown in figure 5.8.

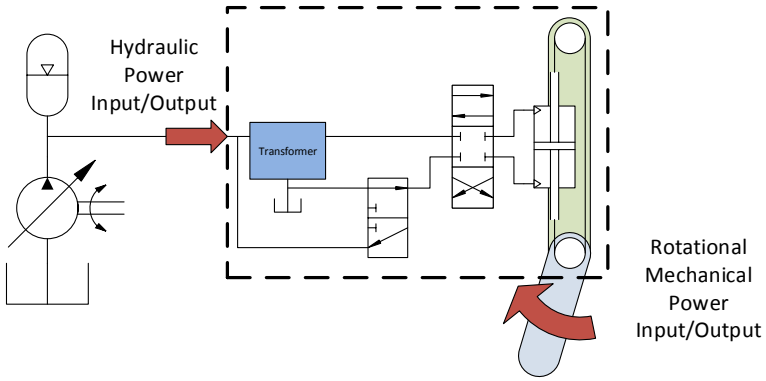

Figure 5.8: Power boundaries for humanoid robot joint actuator

For this case study, the mechanism described in section 5.3 is assumed to transform the mechanical power of the actuator from the linear domain to the rotational domain, with the mechanical power of the system then being the rotational power. To prepare for handling the integrated power flows in the manner discussed above, the power flows must be separated into input and output power flows for each domain.

The instantaneous input fluid power $\mathcal{P}_{f,i}$ of the common pressure rail and the instantaneous input mechanical actuator power $\mathcal{P}_{a,i}$ are given by:

$$\mathcal{P}_{f,i}(t) = P_A Q_A(t) C_{f,i}(P_A, Q_A, t) \tag{5.3}$$

$$\mathcal{P}_{a,i}(t) = T_a(t)\omega_a(t) C_{a,i}(T_a, \omega_a, t) \tag{5.4}$$

where $C_{a,i}(t)$ and $C_{f,i}(t)$ are indicator functions of the form:

$$C_{f,i}(P_A, Q_A, t) = \begin{cases} 1 & P_A Q_A(t) < 0 \\ 0 & \text{else} \end{cases} \tag{5.5}$$

$$C_{a,i}(T_a, \omega_a, t) = \begin{cases} 1 & T_a(t)\omega_a(t) < 0 \\ 0 & \text{else} \end{cases} \tag{5.6}$$

The instantaneous output fluid power $\mathcal{P}_{f,o}$ of the common pressure rail and the instantaneous output mechanical actuator power $\mathcal{P}_{a,o}$ are given by:

$$\mathcal{P}_{f,o}(t) = P_A Q_A(t) C_{f,o}(P_A, Q_A, t) \tag{5.7}$$

$$\mathcal{P}_{a,o}(t) = T_a(t)\omega_a(t) C_{a,o}(T_a, \omega_a, t) \tag{5.8}$$

where $C_{a,o}(P_A, Q_A, t)$ and $C_{f,o}(T_a, \omega_a, t)$ are indicator functions of the form:

$$C_{f,o}(P_A, Q_A, t) = \begin{cases} 1 & P_A Q_A(t) > 0 \\ 0 & \text{else} \end{cases} \tag{5.9}$$

$$C_{a,o}(T_a, \omega_a, t) = \begin{cases} 1 & T_a(t)\omega_a(t) > 0 \\ 0 & \text{else} \end{cases} \tag{5.10}$$

The total input energy $\mathcal{E}_{t,i}$ can then be determined as the summation of the integrated mechanical input power $\mathcal{P}_{a,i}$ and the net integrated fluid power (therefore, energy) if the net fluid energy is entering the system:

$$\mathcal{E}_{t,i} = \left[\int_{t_1}^{t_2} \mathcal{P}_{f,o}(t)dt + \int_{t_1}^{t_2} \mathcal{P}_{f,i}(t)dt \right] C_{t,i} + \int_{t_1}^{t_2} \mathcal{P}_{a,i}(t)dt \tag{5.11}$$

where $C_{t,i}$ is an indicator function that captures whether or not the net fluid power is entering the system:

$$C_{t,i} = \begin{cases} 1 & \left[\int_{t_1}^{t_2} \mathcal{P}_{f,o}(t)dt + \int_{t_1}^{t_2} \mathcal{P}_{f,i}(t)dt \right] < 0 \\ 0 & \text{else} \end{cases} \tag{5.12}$$

In a similar fashion, the total output energy $\mathcal{E}_{t,o}$ can be determined as the summation of the integrated mechanical output power $\mathcal{P}_{a,o}$ and the net integrated fluid power if the net fluid energy is exiting the system:

$$\mathcal{E}_{t,o} = \left[\int_{t_1}^{t_2} \mathcal{P}_{f,o}(t)dt + \int_{t_1}^{t_2} \mathcal{P}_{f,i}(t)dt \right] C_{t,o} + \int_{t_1}^{t_2} \mathcal{P}_{a,o}(t)dt \tag{5.13}$$

where $C_{t,o}$ is an indicator function that captures whether or not the net fluid power is exiting the system:

$$C_{t,o} = \begin{cases} 1 & \left[\int_{t_1}^{t_2} \mathcal{P}_{f,o}(t)dt + \int_{t_1}^{t_2} \mathcal{P}_{f,i}(t)dt\right] > 0 \\ 0 & \text{else} \end{cases} \tag{5.14}$$

The total system efficiency η_t for a given trajectory implemented in the humanoid robot of this case study can then be determined as the fraction of the total output energy with respect to the total input energy:

$$\eta_t = \frac{\mathcal{E}_{t,o}}{\mathcal{E}_{t,i}} = \frac{\left[\int_{t_1}^{t_2} \mathcal{P}_{f,o}(t)dt + \int_{t_1}^{t_2} \mathcal{P}_{f,i}(t)dt\right] C_{t,o} + \int_{t_1}^{t_2} \mathcal{P}_{a,o}(t)dt}{\left[\int_{t_1}^{t_2} \mathcal{P}_{f,o}(t)dt + \int_{t_1}^{t_2} \mathcal{P}_{f,i}(t)dt\right] C_{t,i} + \int_{t_1}^{t_2} \mathcal{P}_{a,i}(t)dt} \tag{5.15}$$

5.5 Method for Evaluating a Point Within the Design Space

In order to find the optimal combination of $D_{1,max}$ and $D_{2,max}$ for a hydraulic transformer submitted to a specific duty cycle, it is necessary to be able to evaluate the performance of a transformer with those design variables. The performance was evaluated in terms of the total weighted system efficiency η_t, which is the overall reward function that is to be maximized. The specification of a single objective function implicitly neglected other potential criteria for evaluating a transformer, such as total mass or cost of manufacture. This was done such that the study could focus on exploring the maximum potential energy savings, after which a multi-objective analysis could be implemented to investigate whether the value of such gains are greater than any costs incurred to achieve them.

Throughout this case study it was assumed that the transformer being optimized was a port switching transformer that could freely switch between the six configurations discussed in chapter 3 depending on which configuration would be the most efficient for the current operating conditions. Therefore, in order to evaluate the performance of a particular trajectory as implemented on a transformer designed with a $D_{1,max}$ and $D_{2,max}$ combination it was necessary to generate composite maps that described the operating region and efficiency performance of the system under consideration. The

loss model described in chapter 2 and the map generating methods and assumptions described in section 2.5 were utilized to generate the composite maps. An example composite map for a transformer with $D_{1,max} = D_{2,max} = 0.4cc$ is shown in figure 5.9.

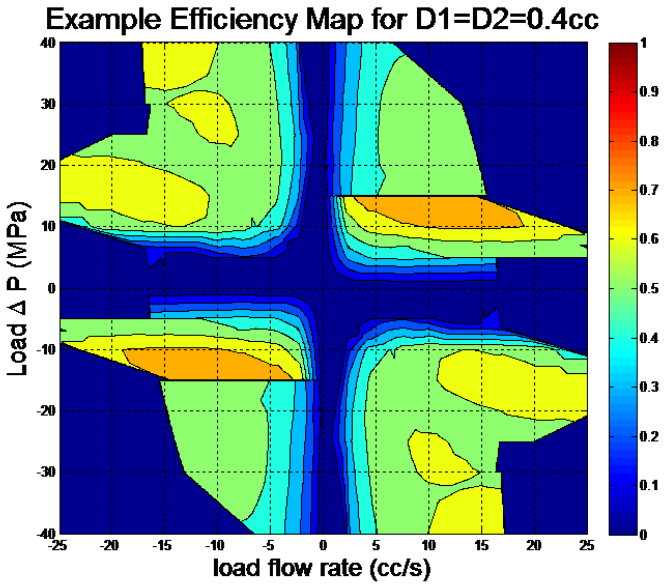

Figure 5.9: Example of a composite efficiency map for a transformer with $D_{1,max} = D_{2,max} = 0.4cc$ operating off of a 1500 psi rail

In order to use the composite efficiency maps to evaluate the system efficiency for the duty cycle under consideration, it was necessary to determine what pressure and flow rate trajectory would be traced out on the composite maps. Therefore it was necessary to convert the force and linear velocity demands of the actuator, shown in figure 5.7, into pressure drop and flow rate requirements. The pressure drop ΔP_a required to achieve a given force F_a for a double-rod actuator is given by:

$$\Delta P_a(t) = \frac{F_a(t)}{A_a} \tag{5.16}$$

And the flow rate Q_a required to move the actuator at the desired linear velocity v_a is given by:

$$Q_a(t) = A_a v_a(t) \tag{5.17}$$

where A_a is the cross-sectional area of the actuators working chamber. The system is underconstrained with one available degree of freedom, meaning that the variable A_a can be taken as a free design variable that can be varied to transform the shape of the pressure and flow rate trajectory used to meet the required force and velocity trajectory. The variation in trajectory shape as a function of actuator cross-sectional area is demonstrated in figure 5.10 for three example area values. The three areas generate three different trajectories that meet the same force and velocity requirements of the actuator. In this study $A_a \in [0, \infty)$ to reflect the option of customizing an actuator for this application if an appropriately sized one was not commercially available.

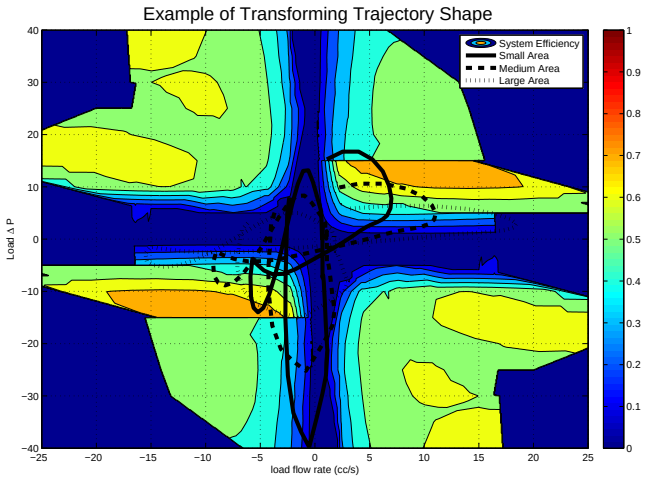

Figure 5.10: Example of transforming the shape of the power demand trajectory with three different actuator cross-sectional areas

The performance assessment assumed that the actuator would have an optimized cross-sectional area A_a such that the shape of the inscribed trajectory resulted in the maximum possible efficiency out of all possible trajectory shapes, as inscribed on the efficiency map of the particular transformer unit under consideration. The method for calculating η_t is given in section 5.4. The single variable optimization of A_a can be achieved by any of a standard suite of robust optimization tools such as a Golden Section search, Newton-Rhapson method, or a sufficiently fine blind search. The method implemented for this analysis was an initial coarse blind search that set the bounds for a precise Golden Section search.

The process of identifying the maximum efficiency η_t for a given size transformer was repeated for a coarse search where the displacements ranged from 0.2 cc to 0.8 cc in 0.1 cc intervals, for a total of 49 points. The results of the coarse search were plotted for the hip, knee, and ankle actuators, as shown in figures 5.11 through 5.13. The coarse search indicated that for each of the three design spaces there would likely be only a single optimal point, not multiple local optimums that would make searching difficult. A gradient search using a first order Taylor series approximation was then implemented, with the initial guess at the location of the maximum identified by the coarse search.

5.6 Results for D_1 D_2 Design Space Exploration for Hip, Knee, and Ankle Actuators

Figures 5.11 through 5.13 show the results of exploration of the design space where the maximum displacements of a hydraulic transformer were independently varied. The values represented are the efficiency of a system of the specified displacements, undergoing a trajectory of the given shape, where the size of the actuator within the system was optimized for each point. The rail pressure was always considered to be constant at 20 MPa. The maps were generated by a simulation using the model described in chapter 2, with the parameters given in appendix A, except where superseded by the scaling laws described in section 2.4.

It should be noted that the scaling laws described in 2.4 that generated the physical parameters of the units were created by measuring the dimensions of hydraulic pump/motors varying between 0.4 cc and 3.2 cc displacements. The regions explored in figure 5.11 through 5.13 extend down to 0.2 cc. The observed scaling trends were extended down to the smaller size, but the nominal optimal points should be interpreted in light of the unverified scaling laws that generated the results. The trends discussed in the following section do not change if the transformers with units smaller than 0.4 cc are discarded. Sizes smaller than 0.2 cc were considered to be too small to defensibly extend the scaling trends to, and therefore transformers with rotating groups smaller than 0.2 cc were not modeled.

Figure 5.11 shows the design space for the hip joint actuator. The optimal size for maximizing the total efficiency of the hip trajectory within the design space investigated

was found to be when $D_{1,max} = D_{2,max} = 0.2cc$.

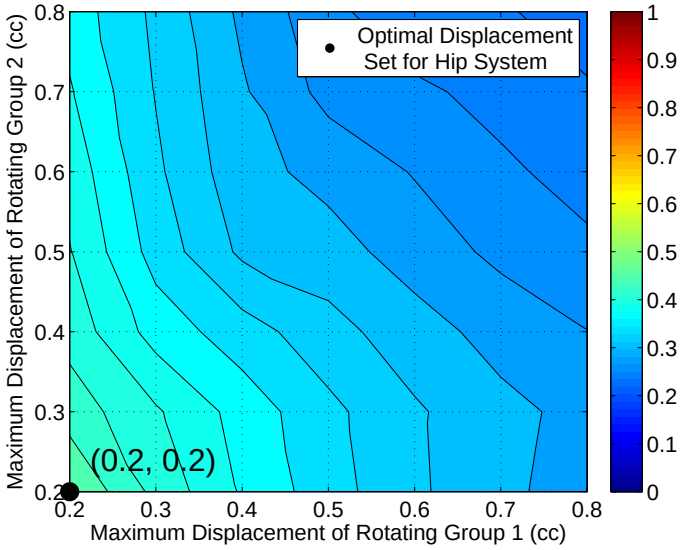

Figure 5.11: Total trajectory efficiency η_t for the hip duty cycle within the $D_{1,max}D_{2,max}$ design space

Figure 5.12 shows the design space for the knee joint actuator. The optimal size for maximizing the total efficiency of the knee trajectory within the design space investigated was found to be when $D_{1,max} = 0.2cc$ and $D_{2,max} = 0.284cc$.

Figure 5.13 shows the design space for the ankle joint actuator. The optimal size for maximizing the total efficiency of the ankle trajectory within the design space investigated was found to be when $D_{1,max} = 0.2cc$ and $D_{2,max} = 0.47cc$.

Figure 5.14 shows the load pressure drop and flow rate trajectories traced out over the optimal composite efficiency maps identified by the sizing efforts of this study. It can be seen that the size and shape of each transformer's operating region is different, due to the differences in the displacements of the rotating groups that they are composed of.

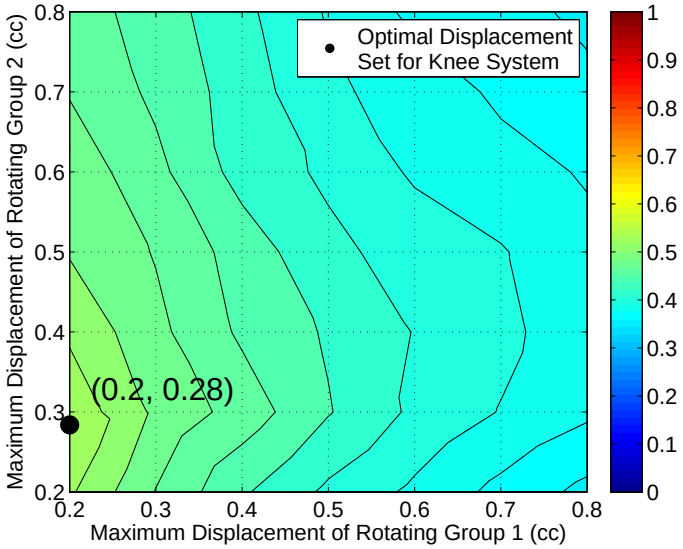

Figure 5.12: Total trajectory efficiency η_t for the knee duty cycle within the $D_{1,max}D_{2,max}$ design space

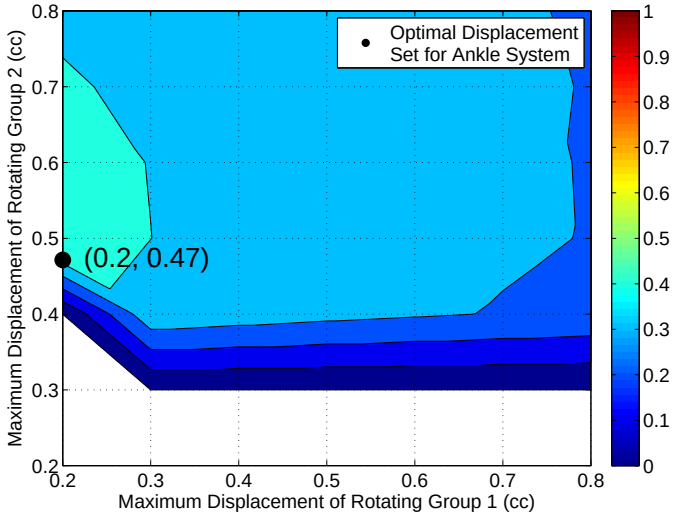

Figure 5.13: Total trajectory efficiency η_t for the ankle duty cycle within the $D_{1,max}D_{2,max}$ design space

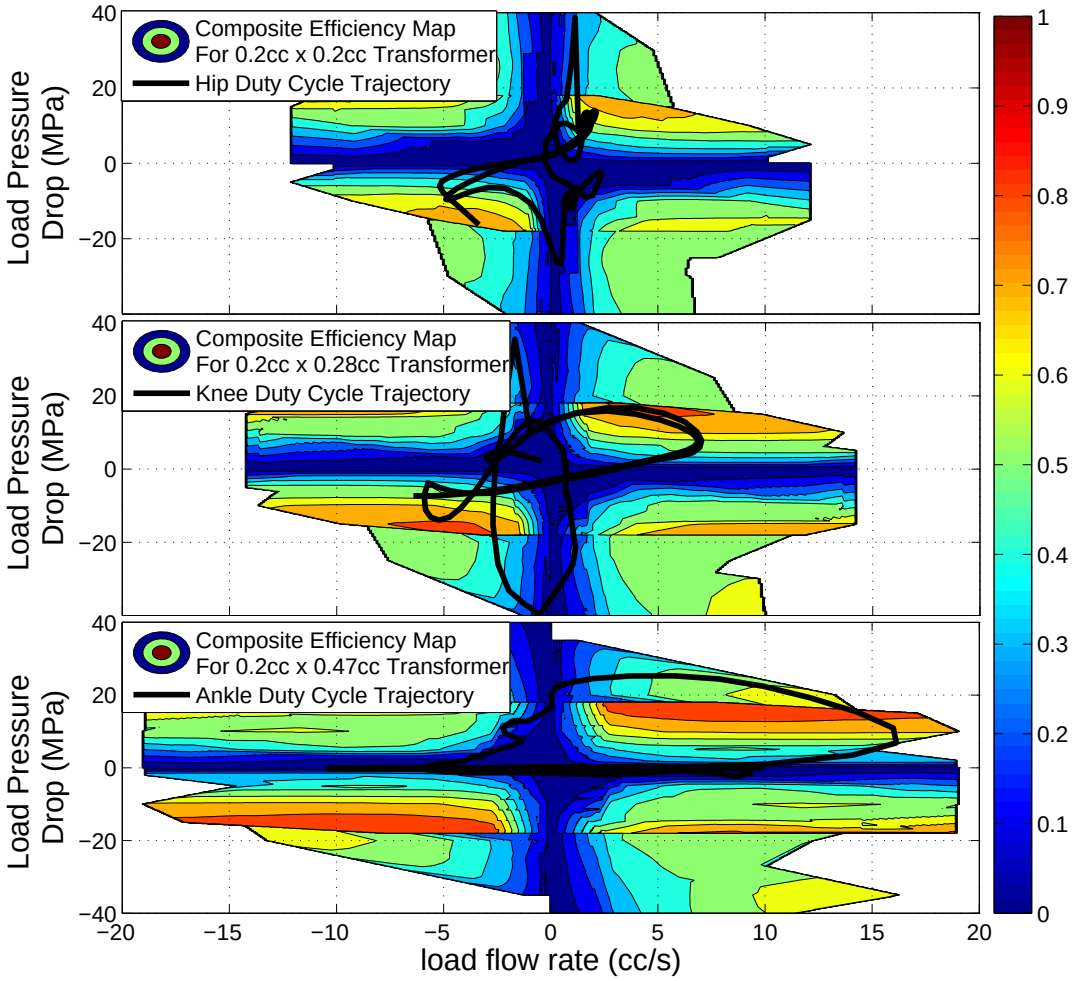

Figure 5.14: Duty cycle trajectories for hip, knee, and ankle systems overlaid on the optimal composite efficiency maps

5.7 Discussion of Results of D_1 D_2 Design Space Exploration

Across the three duty cycles investigated there was a clear trend towards small units being able to achieve higher total system efficiencies across a given duty cycle. This is applicable towards understanding the interaction of the two trends discussed in section 5.2. The first trend was the tendency of the maximum efficiency of axial piston hydraulic pump/motor rotating groups to increasing as their maximum displacement increased. The second trend was the tendency of the efficiency of achieving a given operating point for an axial piston hydraulic pump/motors to as their fractional displacement decreased. The results of this case study indicate that a higher total efficiency across a trajectory can be achieved by having a transformer with smaller rotating groups tending to operate at larger fractions of their displacement, in contrast to larger rotating groups tending to operate at smaller fractions of their displacement.

Despite the general trend towards transformers with smaller rotating groups achieving higher efficiencies, the most efficient transformer was not always the smallest option. In figure 5.12 it can be observed that a transformer with rotating groups $[D_1 = 0.2cc, D_2 = .284cc]$ had a greater efficiency than a physically smaller transformer with $[D_1 = 0.2cc, D_2 = .2cc]$.

Table 5.1 compares the efficiency of the optimal design against the efficiency of the most efficient design with equal displacements. This is meant to characterize the potential efficiency improvements offered by this optimization procedure, in contrast to an optimization procedure exploring only a restricted domain of equal displacement units.

Table 5.1: Comparison of full vs restricted optimization

	Full optimization efficiency	Restricted optimization efficiency
Hip System	46.0 %	46.0 %
Knee System	54.1 %	52.3 %
Ankle System	42.8 %	35.2 %

The results shown in table 5.1 indicate that the value of such an optimization procedure varies depending on the particular duty cycle under consideration. The ankle

actuator exhibited a significant increase in efficiency from the effort, whereas the knee actuator had only minor gains and the hip actuator saw no improvement at all.

The figure 5.13 displaying the design space of the ankle joint has an efficiency of zero for transformers designed with the displacement of their second unit being 0.3 cc or less. This is representative of the fact that the operating regions generated by transformers of that size were unable to fully circumscribe the required trajectory in any shape, and therefore were considered to be unable to meet the duty cycles. As one of the ports of the second rotating group is always connected to the load, it has a stronger relationship than the first rotating group to the capabilities of the transformer to produce or absorb fluid flow along the load line. This stronger relationship explains the asymmetrical distribution of transformers unable to circumscribe the ankle trajectory.

It should be noted that the gradual decrease in efficiency down to an efficiency of zero observed in figure 5.13 is likely not the actual shape of the design space, and is a visual byproduct of the coarse grid search used to initially explore the region. It is more likely that the transition from the relatively high efficiency region to the zero efficiency region is much sharper. It would be expected that the efficiency does taper down slightly prior to becoming zero. As the operating region of the transformer is reduced, the range of actuator cross-sectional areas that generate trajectory shapes that are inscribed within the boundary is also reduced. The limiting of possible options for actuator areas would restrict the optimizing process described in section 5.5. At a location immediately on the boundary there would only be a single possible actuator area that generates a feasible trajectory on the relevant transformer map. As the objective of this case study was to identify the optimal maximum displacements, and the observation described here does not effect that, the location and shape of the boundary was not directly investigated and only noted in this discussion.

5.8 Example of Efficiency Improvement Potential of a Variable Pressure Rail

Throughout this thesis the pressure of the common rail has been assumed to be constant. This is not necessary, as the pressure of the rail could be allowed to vary in a manner similar to load sensing systems. This additional degree of freedom would lead to more

efficient operation. For example, in the humanoid robot case study under consideration in this chapter, there are periods of time when the pressure drops demanded by all three actuators are much lower than the chosen distribution pressure of 20 MPa. Such operating regions require the transformers to operate at low displacements and relatively high leakage rates, resulting in inefficient operation.

Examining the composite efficient maps for port switching transformers, such as shown in figure 5.14, it can be seen that the most efficient region tends to be slightly below the rail pressure. Therefore it is reasonable to guess that an optimized distribution pressure would tend to be slightly greater than the pressure level associated with the greatest rate of instantaneous power transformer amongst the system loads.

In an effort to characterize the potential efficiency improvements of allowing the rail pressure to vary, a single instant of the humanoid robot operation was simulated for a rail pressure other than the 20 MPa used in the study, and the efficient results for the systems operating under the two rail pressures were compared. .

The point chosen for comparison was 0.2 seconds into the gait. At this point in time the hip, knee, and ankle actuators demand pressure drops of 2.57 MPa, 4.41 MPa, and 1.69 MPa respectively, much less than the rail pressure. A new rail pressure of 5.3 MPa was chosen for the comparison simulation. This rail pressure was not optimized, but rather arbitrarily chosen as 120% of the maximum demanded pressure drop as a simple demonstration of potential. Due to the high computational costs associated with adding another dimension to be optimized, the value of a variable rail was only explored in this single non-optimized comparison

Table 5.2 summarizes the efficiency performance of all three actuators for the two rail pressures. The most efficient mode of operation was found to be mode 2 power split for both the hip and the knee, and mode 2 series for the ankle. It can be seen that lowering the rail pressure dramatically improved the hip and ankle efficiency, and had a less drastic but still impressive impact on the knee efficiency.

It should be noted that the results shown in table 5.2 should not interpreted as potential efficiency improvements for the entire trajectory, for two reasons. First, the point simulated was chosen as a point where the greatest benefit from an alternative rail pressure would likely be realized, as all three actuators had low pressure drop demands at that instant. Secondly, the areas where the greatest efficiency improvements would

Table 5.2: Efficiency comparison of 20 MPa rail against a 5.3 MPa rail

	Pressure Drop Demand	Flow Rate Demand	Efficiency with 20 MPa rail	Efficiency with 5.3 MPa rail
Hip Actuator System	2.57 MPa	0.35 cc/s	6.0%	48.9%
Knee Actuator System	4.41 MPa	5.9 cc/s	44.7%	77.7%
Ankle Actuator System	1.69 MPa	0.89 cc/s	2.0%	43.3%

be seen would tend to be periods of low pressure operation, which are typically associated with lower power operation. Low power operation has a correspondingly smaller contribution towards total trajectory efficiency. For both of these reasons, extending the results of table 5.2 to the entire trajectory would significantly overestimate the potential of a variable rail system.

5.9 Chapter Summary

This chapter presented a method for optimizing the maximum displacements of the two rotating groups of a transformer to maximize efficiency for a given duty cycle, and presented efficiency results of such an optimization in a humanoid robot case study. Torque and rotational velocity demand trajectories for the hip, knee, and ankle joints of a human during on cycle of a walking gait were presented. A mechanism and equations for obtaining pressure and flow rate requirements for an actuator to drive such a cycle were given.

An optimally sized transformer was obtained for each of the hip, knee, and ankle joints of the humanoid robot. The following observations were made:

- In all three cases it was observed that it was generally more efficient to have a smaller transformer, however the most efficient transformer was not always the smallest possible transformer.
- The size ratio of the two rotating groups for each joint varied significantly, ranging

from a 1:1 ratio in the transformer for the hip actuator to a 1:2.36 ratio in the transformer for the ankle actuator.

- The maximum efficiency improvement of a non-equal rotating group over an equally-sized rotating group was a change from 35.2% to 42.8% in the transformer for the ankle. The minimum improvement was in the transformer for the hip, which had an optimal sizing of equal displacements, and therefore saw no improvement.

- Allowing the rail pressure to vary was shown to lead to dramatic improvements in efficiency performance at times when all system actuators demand low pressure drops, although characterization of the value in terms of total trajectory improvement of a variable rail is left for future work.

It can be concluded that optimizing the sizes of the rotating groups of a transformer can have a moderate impact on the efficiency performance of a system that includes the machine. Chapter 6 uses the same human walking gait duty cycle to compare the power distributing performance of the optimized transformers against traditional throttling valve architectures.

Chapter 6

Comparison of Distribution Efficiency in a Humanoid Robot Case Study

6.1 Chapter Overview

The objective of this case study is to compare the efficiency of hydraulic transformers against traditional throttling valves as a means of distributing power to a system of hydraulic actuators. A throttling valve architecture is chosen as a comparison due to their ubiquity, which stems from their simplicity, small size, and good control performance. The energy saving potential of hydraulic transformer power distribution as compared to a throttling valve architecture is often mentioned in existing literature, but this case study is the first presentation of a complete side by side analysis.

The loss model described in chapter 2 is used to evaluate the transformer performance, and the equations to model the throttling valve performance are derived within this chapter in section 6.3. The efficiency for the total cycle is considered to be the ratio of the total mechanical energy output by the actuator to the net fluid energy taken from the rail to achieve the desired behavior. Determining the efficiency in such a manner for an entire realistic duty cycle is useful for evaluating the performance of a technology, as a machine will often cover a wide range of operating points during a

trajectory, and a complete analysis can appropriately weigh the impact of varying local performance. This is particularly important for duty cycles such as a humanoid robot, which spend a significant portion of their time deviating from the region of highest efficiency, and therefore can place higher value on a wide region of efficient operation than a comparable machine that operates primarily in one condition.

6.2 Objectives and Methods of Distribution Efficiency Comparison

This case study compares the efficiency of hydraulic transformers against traditional throttling valves as a means of distributing power to a system of hydraulic actuators driving the leg joints of a humanoid robot. Both distribution methods are implemented through a common pressure rail architecture, as such an approach allows for a single large prime mover to supply power to entire system. A schematic of the system is given in figure 6.1, which illustrates the interchangeability of the power distribution and control devices. The system and duty cycle used is the humanoid robot described in section 5.3.

As with the rest of the studies in this thesis, there were a number of model simplifications made in order to focus on the trends of the power distribution technologies under consideration. All modelled valves, pipes, and actuators were considered to be lossless, performing their function without impinging losses on the system. Additionally the prime mover and accumulator were assumed to have sufficient bandwidth and capacity to track the hydraulic oil flow rate demand while maintaining a common pressure in the distribution rail. These simplifications were made in order to eliminate the need to make assumptions about a large number of design variables with non-obvious solutions, such as valve sizes, fitting orientations, and actuator sealing styles. Modeling such ancillary features as ideal facilitate a more direct comparison of the trends of the power distribution technologies themselves.

As the two distribution technologies are being evaluated on a system level, not a unit level, the system efficiency equation (5.15) derived in section 5.4 is used. The power inputs and outputs of the rail fluid power and the actuator mechanical power are the same for both technologies, and therefore the same equation is used to evaluate

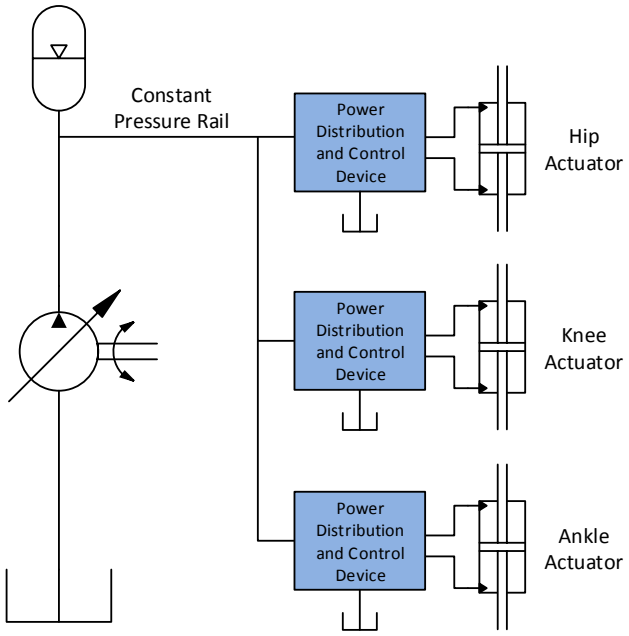

Figure 6.1: Schematic of hydraulic common pressure rail power distribution system with generic power distribution and control devices

both approaches.

The parameters of both technologies were optimized to maximize their efficiency for the duty cycle they would be operating in. For the transformer the optimization results were the ones arrived at by the case study of chapter 5, and are repeated here in table 6.1 for reference. For the throttling valve architecture the actuators were sized such that the maximum pressure seen throughout the duty cycle was exactly the rail pressure, the process for which is given in the following section.

Table 6.1: Optimal rotating group sizes

	$D_{1,max}$	$D_{2,max}$
Transformer for Hip System	0.20 cc	0.20 cc
Transformer for Knee System	0.20 cc	0.28 cc
Transformer for Ankle System	0.20 cc	0.47 cc

6.3 Description of Throttling Valve Architecture

The hydraulic transformer is compared against a throttling valve architecture due to the widespread use of servovalves as a means of distributing power to and controlling systems of linear actuators. The valves are chosen for their simplicity, robustness, small form factor, and good control performance. They can be found in popular demonstrations of robotics such as Boston Dynamics' BigDog [47], shown in figure 6.2.

The throttling valves modeled in this case study are 4-way servo-proportional valves, as shown in figure 6.3. The valves create a fluidic connection between the rail and the load, and perform their control function by reducing the pressure of the fluid from the constant pressure of the rail to whatever pressure is required by the actuator at that point in the cycle. The rail is assumed to be at a constant pressure for the throttling valve distribution architecture. The reduction in pressure is achieved by actively controlling the size of a throttling orifice that the fluid passes through. The dynamics of the valves are not modeled in this case study.

There are two important differences between the throttling valve approach and a hydraulic transformer approach. First, throttling valves do not have any means by which to boost the fluid pressure above the rail pressure, whereas a transformer can achieve this function. Secondly, due to the inability of the valves to raise the fluid

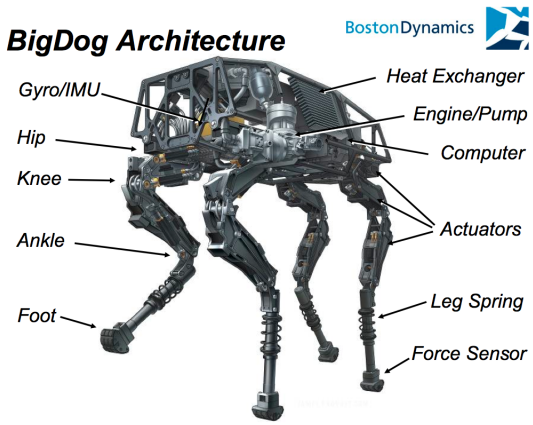

Figure 6.2: Boston Scientific's BigDog robot, as an example of a mobile robot using a throttling valve architecture to control a system of linear actuators

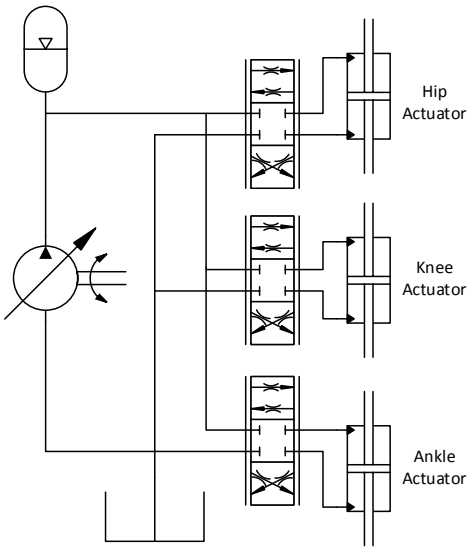

Figure 6.3: Throttling valve power distribution architecture

pressure, they are unable to regenerate flow into the rail when there is mechanical power input through the actuator. In this scenario the potential input energy is not recovered and additional power is wasted by the necessity to provide fluid from the rail.

In order to facilitate a comparison of efficiency between distribution technologies, it was assumed that the valves have sufficient bandwidth to track the given duty cycles. The only losses considered are the reductions in pressure necessary to modify the rail pressure to the demanded load pressure. Leakage losses through the valve spools are not considered.

In order to remain consistent and provide a fair comparison against a transformer, the cross-sectional area of the three actuators in the throttling architecture were also sized to maximize the total efficiency across their duty cycle. As shown in equations (5.16) and (5.17), for a given required force and velocity the larger the cylinder the lower the pressure and higher the flow rate. For a throttling valve the exact required fluid volume must come from the rail, supplied at pressure P_A and reduced to pressure P_B. The result is that the most efficient actuator is the one with the smallest cross-sectional area A_t that is able to meet the maximum force requirement F_{max} of the duty cycle.

$$A_t = \frac{F_{max}}{P_A} \tag{6.1}$$

As any motion of the actuator in the throttling architecture is achieved by an equal volumetric flow rate from the rail, and the rail is always held at pressure P_A, the fluid power delivered to and from the system can be obtained by:

$$\mathcal{P}_{f,i}(t) = P_A Q_a(t) \tag{6.2}$$

$$\mathcal{P}_{f,0} = 0 \tag{6.3}$$

where the fluid power output of the system is always zero due to the inability of throttling valves to regenerate into the rail. The flow rate Q_a required by the actuator can be determined from the absolute value of the required velocity v_a and cross-sectional

area:

$$Q_a(t) = |v_a(t)|A_t \tag{6.4}$$

The mechanical power flow associated with the actuator are the same as derived in section 5.4, repeated here for reference:

$$\mathcal{P}_{a,i}(t) = T_A(t)\omega_a(t)C_{a,i}(t) \tag{6.5}$$

$$\mathcal{P}_{a,o}(t) = T_A(t)\omega_a(t)C_{a,o}(t) \tag{6.6}$$

where $C_{a,i}$ and $C_{a,o}$ are indicator functions given by equations 5.6 and 5.10 respectively.

The fluid power and mechanical power flows can then be used to derive the total efficiency in the same manner as in section 5.4, the result of which is repeated here for convenience:

$$\eta_t = \frac{\mathcal{E}_{t,o}}{\mathcal{E}_{t,i}} = \frac{\left[\int_{t_1}^{t_2} \mathcal{P}_{f,o}(t)dt + \int_{t_1}^{t_2} \mathcal{P}_{f,i}(t)dt\right] C_{t,o} + \int_{t_1}^{t_2} \mathcal{P}_{a,o}(t)dt}{\left[\int_{t_1}^{t_2} \mathcal{P}_{f,o}(t)dt + \int_{t_1}^{t_2} \mathcal{P}_{f,i}(t)dt\right] C_{t,i} + \int_{t_1}^{t_2} \mathcal{P}_{a,i}(t)dt} \tag{6.7}$$

where $C_{t,i}$ and $C_{t,o}$ are indicator functions given by equations (5.12) and (5.14) respectively.

6.4 Power Trajectory Comparison and Efficiency Results

This section gives the simulated performance of both hydraulic transformers and throttling valves in the application of delivering power to the hip, knee, and ankle actuators of a humanoid robot. The transformer performance was simulated using the model described in chapter 2. The throttling valve performance was modeled using the description given in section 6.3. The duty cycle for the humanoid robot was the torque and rotational velocity of the hip, knee, and ankles of a 57 kg human performing a single step within a walking gait.

The rail pressure for both systems was 20 MPa, as it is a standard in the industry and the majority of off-the-shelf hydraulic components are rated to operate at that pressure. As the transformer boosts the load pressure above the 20 MPa of the rail, the

load line and actuator would have to be able to withstand higher pressures, but the rest of the circuit could be designed for standard pressures. The complete parameters of the hydraulic transformers for each joint are given in appendix A, except where superseded by the parameter scaling laws of chapter 2.

Figures 6.4 through 6.6 show the power profiles, pressure profiles, and duty cycles for each of the three joint actuators of the humanoid robot. The actuator power profile represents the actual mechanical power required or supplied by the joint throughout the cycle. The hydraulic transformer and throttle valve power profiles represents the simulated fluid power delivered to each system through the common pressure rail in order to have them achieve the demanded actuator operation. The pressure profiles show the required pressure drop across the actuator necessary to achieve the instantaneous torque demand, and the duty cycle is the same as show previously repeated here for convenience.

For the mechanical power a positive value represents power flowing out of the system and a negative value represents the system absorbing power from an overrunning load. For both the transformer and the throttling valve profiles positive values represent fluid power flowing into the system and negative values represent fluid power being regenerated into the rail. The shaded portion of the graph highlight the regions where the load power is negative, nominally regenerating power back into the system.

Table 6.2 shows the total efficiency of each of the joint trajectories for both of the power distributing approaches. The efficiency values were determined using equation (5.15) of section 5.4. The total system efficiency of all three joints combined are also given, where the values were also determined using equation (5.15), but where each power flow term was the summation of the power flows from all three joints.

Table 6.3 gives the mechanical energy requirement of each of the joints for one complete cycle, where a cycle equates to one step of a typical human walking gait. The mechanical energy requirement of the joint can be considered the baseline for comparison, as it is the energy that would be consumed by a idealized lossless power distribution architecture. Also given are the quantities of energy consumed during one full cycle by both the transformer architecture and the throttling architectures for each of joints.

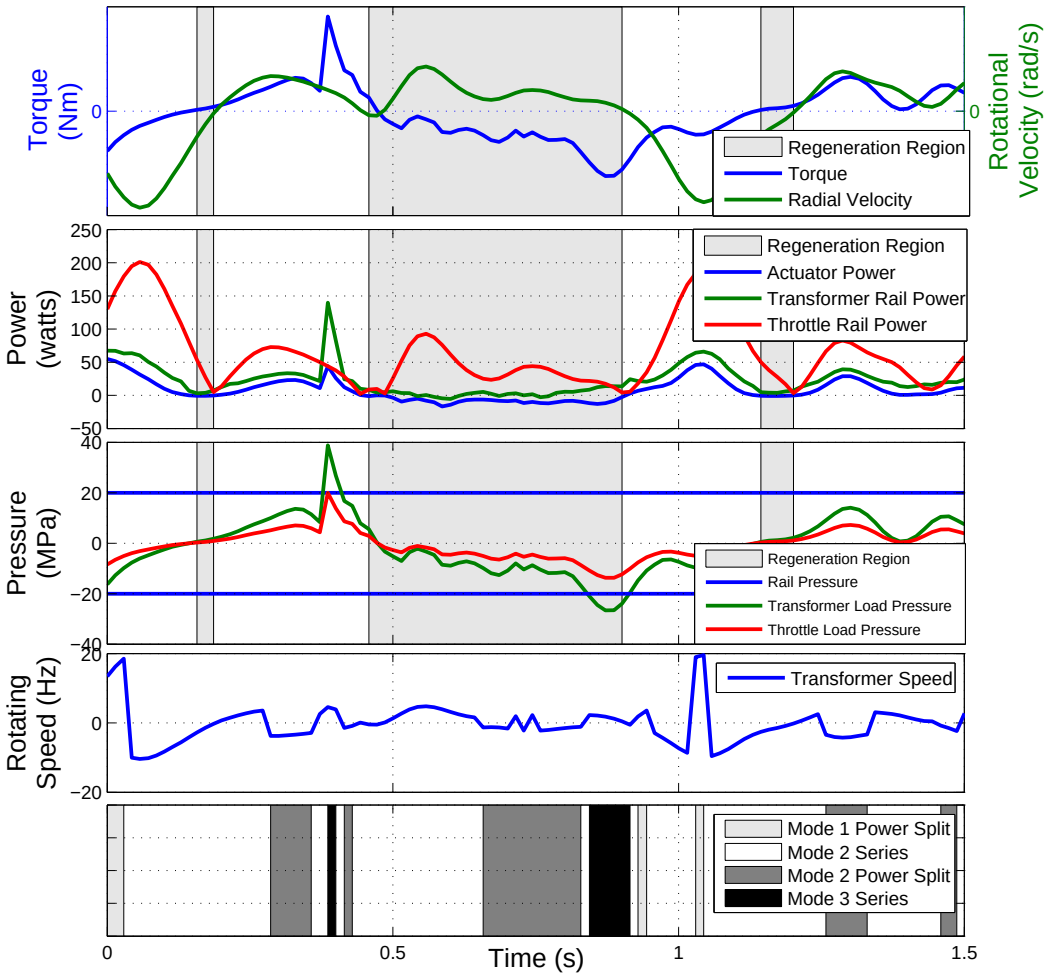

Figure 6.4: Power, Pressure, and demand profiles for hip actuator

Table 6.2: Distribution Efficiency Results for Transformer and Throttling Architectures

	Transformer Architecture Distribution Efficiency	Throttling Distribution Architecture Efficiency
Hip System	46.0%	16.2%
Knee System	54.1%	18.8%
Ankle System	42.8%	12.9%
Total	48.0%	15.8%

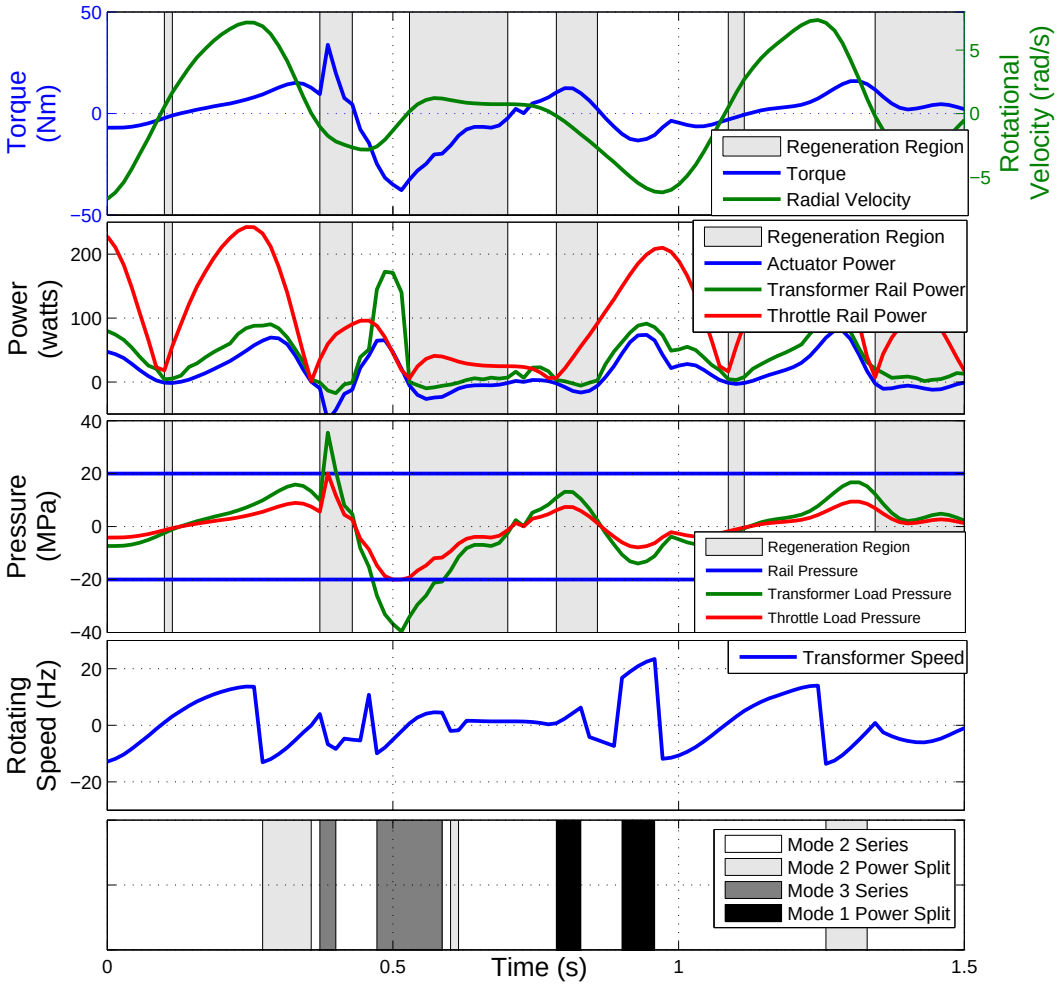

Figure 6.5: Power, Pressure, and demand profiles for knee system

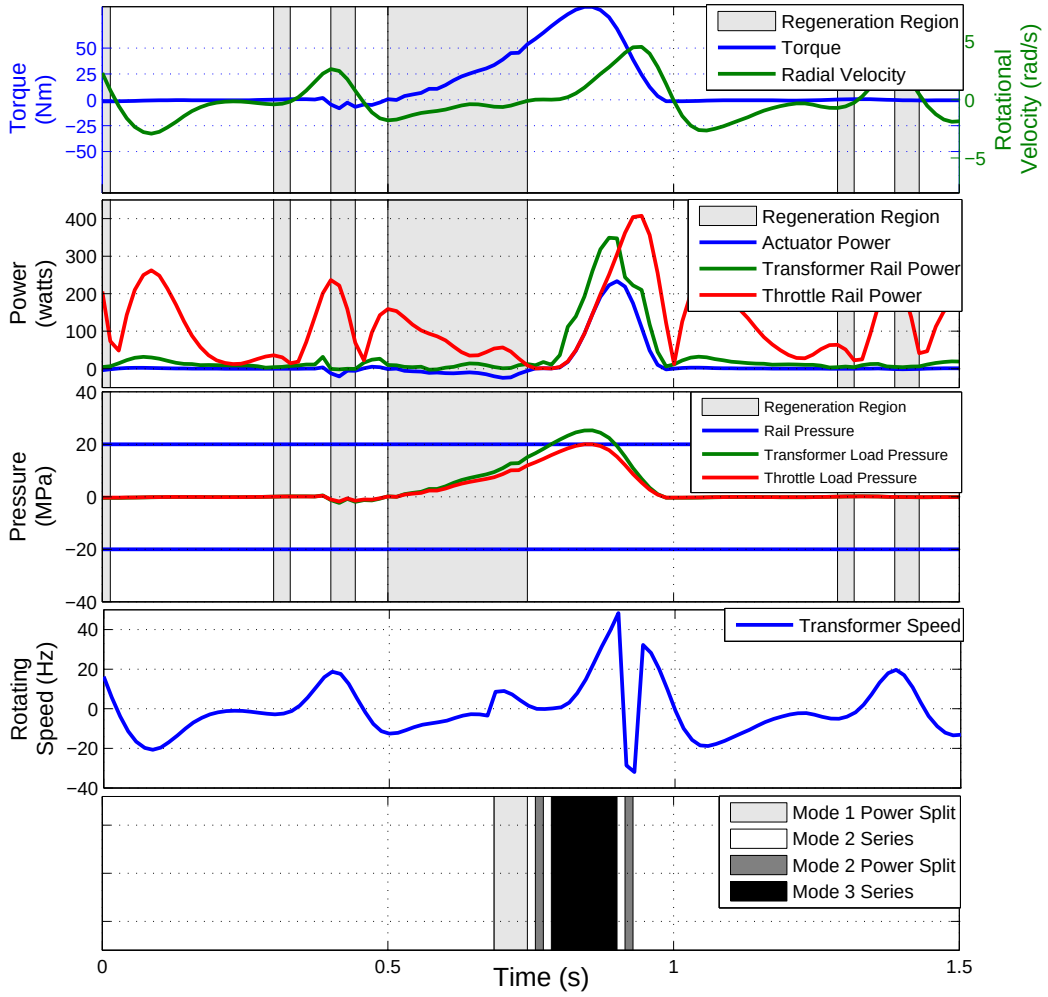

Figure 6.6: Power, Pressure, and demand profiles for ankle system

Table 6.3: Energy consumption for one cycle with transformer and throttling architectures

	Useful mechanical energy out	Transformer architecture energy consumption	Throttling architecture energy consumption
Hip System	15.2 J	33.0 J	93.8 J
Knee System	29.6 J	55.9 J	157.4 J
Ankle System	22.1 J	52.7 J	171.2 J
Total	66.9 J	141.6 J	422.4 J

6.5 Discussion of Efficiency Comparison

Transformer vs Throttle Power Profiles Figures 6.4 through 6.6 show that the instantaneous power consumption of the transformer based distribution system is much closer to the required power of the actuator for almost the entirety of the three trajectories. As any excess power consumption above the required actuator power is wasted as distribution losses, a closer instantaneous power indicates more efficient operation at that point. Table 6.2 clearly shows the cumulative result of the transformers instantaneous performance by having significantly greater total efficiency for all three cycles.

The throttling architecture briefly achieves higher efficiencies than the transformer architecture twice during the hip trajectory and once each during the knee and ankle trajectories. These events can be classified in two categories. First, the throttling architecture outperforms the transformer architecture at the point of the trajectorys maximum torque demand. At this point the throttling architecture demands a pressure drop equal to the rail pressure, resulting in a distribution efficiency of 100%. The transformer architecture, which always contains losses, cannot match this performance. The second point where the throttling architecture is more efficient is during periods of extremely low flow rate demand. The throttling system will consume very low amounts of power during this period, in contrast to the transformer system which will incur non-negligible leakage losses from the highly pressurized rail.

Bucking vs Boosting Operation Of interest is the relatively low period of time that the transformer system spent boosting the load pressure above the common rail pressure. All three trajectories saw only a single short event where pressure was boosted above the rail pressure, in conjunction with the point where the maximum torque was demanded. It is noteworthy to recognize that only the hip pressure trajectories came close to meeting the maximum allowed value of 40 MPa, which could have been achieved in the other two cases by having smaller cross-sectional area of the respective actuators.

The transformer system still boosted pressure at the point of maximum required torque, but due to the relatively small amount of power transfer during that time the optimization procedure chose displacements that favored other regions. This result was that the brief boosting event was less efficient than would have been possible if the machine had been designed for efficient boosting. This indicates that the optimization process of chapter 5 found it to be more efficient to keep the majority of the pressure trajectory within a region below the rail pressure, and then select displacements that maximized efficient operation in that region.

Referring to the composite maps of figure 5.14, it can be seen that the most efficient region of operation is located in the bucking region below 20 MPa, not boosting above the 20 MPa rail. The system efficiency analysis of chapter 3 indicates that the high efficiency region is derived from the mode 2 power split configuration. This suggests a general conclusion: that an optimization procedure will likely show that the most efficient operation can be achieved by keeping the majority of the power transfer in the bucking region and optimizing the system to be most efficient in that region.

It is important to note that a preference towards either bucking or boosting does not necessarily lead to a preference of either displacement group being larger or smaller. For example, the equation (3.29) indicates that a mode 2 series configuration has its point of highest efficiency located in the bucking region for both a situation where D_1 is the larger of the two as well as when D2 is larger. Therefore the results of this chapter, where it was found that both bucking operation and a larger D_2 were generally preferred, should not be interpreted as correlated trends.

Regeneration Performance One of the reasons for choosing a humanoid robot as a case study was to investigate the performance of a hydraulic transformer system in regenerating power from an overrunning load. All three duty cycles modeled in this case

study showed that when the transformer system was nominally in a regenerating region, it would often be oscillating between low levels of regeneration and low levels of power expenditure, such as seen between 0.5 seconds and 0.7 seconds of the ankle duty cycle. The lack of consistent regeneration can be explained by two facts. First, an examination of the duty cycle trajectories overlaid on the transformer efficiency maps of figures 5.14 indicate that the transformer is often operating in inefficient conditions while nominally regenerating, thus losing significant amounts of the power available for regeneration. Secondly, useful power is always leaking from the rail through the transformer port plate. When the leakage of useful power from the rail exceeds the quantity recovered from the overrunning load, the system is still considered to be expending power in order to achieve the desired operating point.

Despite the failure of the transformer system to regenerate most of the recoverable power, it still significantly outperformed the throttling system in the regeneration regions. The architecture of the throttling system requires fluid to be expended from the rail to generate motion regardless of the mode of operation, consuming power while giving no opportunity for regeneration. This is most noticeable between 0.5 seconds and 0.8 seconds of the hip trajectory, where the hip joint is in motion but essentially unloaded. The throttling system can be seen as inefficiently expending large amounts of power to accomplish the desired motion.

The regeneration opportunities of the duty cycles under consideration in this chapter were all relatively light, and consequentially placed the transformer in an inefficient operating region. Greater magnitudes of regeneration potential would likely result in more efficient power recovery. Such opportunities could be found while arresting the swing motion of an excavator cab or during the breaking events of vehicle motion.

Leakage Losses During Inactivity The regions of this study that had relatively low power flow indicated that the leakage of fluid from the rail through the valve plate of a transformer is a non-negligible power loss. This source of power loss could become significant in applications that have longer periods of inaction, such as a transformer powering an ancillary device only used occasionally. Such a configuration would potentially see large amounts of power lost in leakage through the transformer during inaction. This loss could be largely mitigated through the introduction of an on/off valve to separate the transformer from the rail during periods of inaction.

6.6 Chapter Summary

The case study of this chapter built upon all of the previous chapters to compare the efficiency of a hydraulic transformer architecture against a traditional throttling valve architecture as a means of distributing power to a system of hydraulic actuators driving the leg joints of a humanoid robot. It used the loss model of chapter 2 to simulate the behavior of the port switching transformer introduced in chapter 3. It was assumed that the machine could switch between configurations during operation, as experimentally demonstrated in chapter 4. Lastly, the rotating groups of the three hydraulic transformers used in the study were optimized to maximize efficiency for the duty cycle of the joint they were driving, as shown in chapter 5.

It was shown that the hydraulic transformer systems outperformed the throttling valve systems for all three joints of the humanoid robot. In terms of total combined distribution efficiency of all three joints over their trajectories, the transformer architecture achieved an efficiency of 47.6%, which is threefold increase on the throttling architecture's efficiency of 16.0%. In terms of energy consumption, the transformer architecture completed a cycle with a total of 141.6 joules, which is a 66.5% decrease from the total throttling architecture energy consumption of 422.4 joules.

Analysis of the pressure trajectories of the transformer systems revealed that the systems spent a majority of their time distributing fluid at pressures lower than the distributing rail pressure. The throttling valves impinged significant losses on their systems during periods of unloaded motion. The transformer systems did not efficiently recover energy from overrunning loads, as the operating conditions of such opportunities tended to be in inefficient regions, but they still outperformed the throttling valves which had to expend energy even during periods of nominal regeneration.

In conclusion, the hydraulic transformer power distribution architecture was shown to have the potential to significantly outperform a throttling valve architecture in terms of efficiency for a humanoid robot application. It is important to note that efficiency performance is only one of many metrics that would be used to evaluate the fitness of a particular solution to the power distribution problem. Consideration would also have to be given to the form factor, control capabilities, production cost, and reliability before a decision could be made as to which approach better fulfilled the multiple objectives

of this particular application.

Chapter 7

Conclusion

7.1 Review of Thesis Content

This thesis characterized the performance of a power distribution architecture utilizing hydraulic transformers. The development of a dynamic loss model of a hydraulic transformer was presented, along width a set of rules and assumptions that can be used to generate performance maps to show the operating region and efficiency trends of the machine.

Six configurations of a hydraulic transformer and actuator system were presented, and the unique operating regions and efficiency trends of each system were shown through simulation results from the described dynamic loss model. A set of configurations called 'power split' were introduced, where power can be communicated to or from the actuator through a nearly lossless hydraulic line parallel to the transformer.

The hydraulic circuit for a system capable of switching between transformer configurations, called a 'port switching transformer', was presented and the performance maps of such a system given. A prototype port switching transformer was assembled, experimentally characterized, and utilized to demonstrate the feasibility of switching during operation and explore the characteristics of transition events between configurations.

The potential efficiency improvements achievable through optimal sizing of a transformer's two rotating groups was demonstrated in a humanoid robot case study. The behavior and efficiency performance of the optimized transformer power distribution architectures was then compared against a throttling valve architecture in the same

humanoid robot system.

7.2 Summary of Research Conclusions

This thesis sought to thoroughly explore the various configurations of a power distribution system utilizing hydraulic transformers and characterize the potential efficiency performance of such systems. The notable conclusions of this effort are summarized below:

- The performance of six transformer system configurations were explored, and it was demonstrated that each configuration has a unique operating region and efficiency trends.
- Three of the configurations were so-called power split configurations, which were shown to be able to achieve higher system efficiencies than the highest possible transformer unit efficiency. Prior literature had briefly introduced a single power split configuration, but the performance potential had not been characterized.
- The concept of a 'port switching transformer' capable of using valves to switch between configurations based on the instantaneous operating demands was introduced, and a circuit capable of achieving such behavior was presented.
- The feasibility of implementing a port switching transformer was demonstrated on an experimental test bench that successfully transitioned between various configurations while tracking a trajectory.
- A case study exploring the potential efficiency improvements offered by optimizing the sizes of the transformer rotating groups indicated that the size ratio between the groups varied significantly, ranging from a 1:1 ratio to a 1:2.4 ratio across the three duty cycles investigated.
- The maximum efficiency improvement of a non-equal rotating group transformer over a transformer with equally-sized rotating groups was a moderate gain of 7.6%, increasing the efficiency to 42.8% from 35.2%. The smallest improvement was the unit whose optimum ratio was 1:1 and therefore saw no improvement from the sizing effort.

- A comparison of a hydraulic transformer distribution architecture against a throttling valve distribution architecture for driving the hip, knee, and ankle joints of the leg of a humanoid robot indicated that the transformer system had significantly better efficiency performance. The transformer architecture achieved a distribution efficiency of 47.6%, which was a 31.9% increase over the throttling architecture distribution efficiency of 16.0%. The transformer system consumed 142 J to drive a single step of a standard walking gait, representing a decrease of 281 J from the 422 J required by the throttling architecture.

7.3 Recommendations for Future Work

The research efforts of this thesis uncovered many questions that warrant further investigation. The areas in which further work would be most effective are described here.

The pressure distribution rail was considered to be constant throughout this thesis. The restriction is unnecessary, and it is likely that significant performance improvements could be realized by allowing the pressure rail to vary in a manner similar to a state of the art load sensing system. An exploration of the potential efficiency improvements of a variable pressure rail would be of value.

The studies within this thesis focused on the efficiency of the distribution architecture, and considered other system components to be lossless. The impact of transformers on complete system performance could be better understood by a case study that considers the losses in all of the components. Such results could further increase the relative performance of a transformer architecture as compared to alternatives, for example by potentially allowing the prime mover to operate in regions of higher efficiency by partially decoupling its behavior from the actuator behavior through the pressure rail.

The experimental investigation of port switching behavior demonstrated that certain trajectories were feasible, but it also revealed that other trajectories could not be achieved with the prototype design and simple feedback controller used in chapter 4. A more advanced controller with feedforward aspects that could anticipate a transition event and prepare the machine for it would likely enable previously unattainable

transitions, as well as create smoother transitions for the trajectories that are already possible.

In conclusion, the operating region and efficiency performance of a hydraulic transformer power distribution architecture has been characterized. The performance was shown to be able to be increased by switching between configurations and optimization of the transformer rotating group sizes. It is important to note that efficiency is only one of the metrics that should be used to evaluate the fitness of a particular solution to the power distribution question. Consideration should also be given to form factor, control capabilities, production cost, and reliability before a decision is made as to which approach better fulfills the multiple objectives of the application under consideration.

References

[1] R Hippalgaonkar, M Ivantysynova, and J Zimmerman. Fuel savings of a mini-excavator through a hydraulic hybrid displacement controlled system. In *Proceedings of the 8th International Conference on Fluid Power*.

[2] T.R. Morgan. Transformer for hydraulic machines, August 4 1896. US Patent 565,014.

[3] G.E.M. Vael, P.A.J. Achten, and Z. Fu. The innas hydraulic transformer the key to the hydrostatic common pressure rail. In *International Off-Highway and Powerplant Congress and Exposition*, 2000.

[4] K.H. H. Hydraulic transformer, December 14 1971. US Patent 3,627,451.

[5] M.J. A. Hydraulic transformer, July 26 1966. US Patent 3,262,395.

[6] L.C. B. Hydraulic transformer, April 18 1967. US Patent 3,314,367.

[7] P.A.J. Achten, Z. Fu, and G.E.M. Vael. Transforming future hydraulics: a new design of a hydraulic transformer. In *The Fifth Scandinavian International Conference on Fluid Power SICFP '97*, page 287ev, 1997.

[8] J. Clarke. Hydraulic transformer using a pair of variable displacement gear pumps, August 8 2002. US Patent App. 09/776,842.

[9] E.D. Bishop. Digital hydraulic system, March 14 2013. US Patent App. 13/652,054.

[10] Y. Kita. Rotational hydraulic transformer, August 29 2000. US Patent 6,109,884.

[11] D.C. Hale. Hydraulic pressure transformer, December 24 2002. US Patent 6,497,558.

[12] Ronnie Werndin, Peter Achten, Mikael Sannelius, and Jan Ove Palmberg. Efficiency performance and control aspects of a hydraulic transformer. In *The Sixth Scandinavian International Conference on Fluid Power SICFP '99*, pages 385–407, 1999.

[13] Ma Jien, Xu Bing, Ouyang Xiaoping, and Yang Huayong. The cfd simulation research on hydraulic transformer. *Proceedings of the 6th JFPS International*, 2:334–339, 2005.

[14] H.A. L, K.A. M, and W.J.W.A. Van. Motor vehicle hydraulic system, April 14 1959. US Patent 2,881,706.

[15] Peter Achten, T Brink, Jeroen Potma, Marc Schellekens, and Georges Vael. A four-quadrant hydraulic transformer for hybrid vehicles. In *The 11th Scandinavian International Conference on Fluid Power, Sweden*, 2009.

[16] P.A.J. Achten. Changing the paradigm. In *The Tenth Scandinavian International Conference on Fluid Power SICFP '07*, 2007.

[17] PAJ Achten, GEM Vael, and Kim Heybroek. Efficient hydraulic pumps, motors and transformers for hydraulic hybrid systems in mobile machinery. *1st International VDI Conference "Transmissions in Vehicles"*, 2011.

[18] P. Hammelmann. Hydraulic pressure transformer, August 30 1983. US Patent 4,401,415.

[19] J. Dantlgraber. Hydrostatic drive system for an injection molding machine and a method for operating such a drive system, March 4 2003. US Patent 6,527,540.

[20] R. Werndin and J-O Palmberg. Hydraulic transformers - comparison of different designs. In *The Eighth Scandinavian International Conference on Fluid Power SICFP '03*, pages 163–174, May 2003.

[21] Triet Hung Ho and Kyoung Kwan Ahn. Saving energy control of cylinder drive using hydraulic transformer combined with an assisted hydraulic circuit. In *International*

Conference on Control, Automation and Systems 2009, pages 2115–2120. IEEE, 2009.

[22] Rikiya Inoguchi, Kazuhisa Ito, and Shigeru Ikeo. Pure hydraulic hybrid cylinder drive system with hydraulic transformer. *JFPS International Journal of Fluid Power System*, 5, 2012.

[23] MJ Martin and B Taylor. Optimised port plate timing for an axial piston pump. In *5th int fluid power symposium, Cranfield, England*, pages 13–15, 1978.

[24] Shu Wang. The analysis of cavitation problems in the axial piston pump. *Journal of Fluids Engineering*, 132(7):074502, 2010.

[25] H. Merritt. *Hydraulic Control Systems*. John Wiley & Sons, Inc., New York, NY, 1966.

[26] Yi Fang and Masataka Shirakashi. Mixed lubrication characteristics between the piston and cylinder in hydraulic piston pump-motor. *Journal of tribology*, 117(1):80–85, 1995.

[27] Bernard J Hamrock, Steven R Schmid, and Bo O Jacobson. *Fundamentals of fluid film lubrication*. CRC press, 2004.

[28] Shuo Lin and Jibin Hu. Tribo-dynamic model of slipper bearings. *Applied Mathematical Modelling*, 39(2):548–558, 2015.

[29] Changbin Guan, Zongxia Jiao, and Shouzhan He. Theoretical study of flow ripple for an aviation axial-piston pump with damping holes in the valve plate. *Chinese Journal of Aeronautics*, 2013.

[30] JM Bergada, J Watton, and S Kumar. Pressure, flow, force, and torque between the barrel and port plate in an axial piston pump. *Journal of Dynamic Systems, Measurement, and Control*, 130(011011), 2008.

[31] Baek-Hyun Cho, Hyoun-Woo Lee, and Jong-Sun Oh. Estimation technique of air content in automatic transmission fluid by measuring effective bulk modulus. *International journal of automotive technology*, 3(2):57–61, 2002.

[32] Noah D Manring. Friction forces within the cylinder bores of swash-plate type axial-piston pumps and motors. *Journal of dynamic systems, measurement, and control*, 121(3):531–537, 1999.

[33] S. Duan and T. Nielsen. Modeling and analysis of directional control valves with tapered-angle and eccentric clearance. *2007 ASME International Mechanical Engineering Congress and Exposition*, November 2007.

[34] Toshiharu Kazama and Atsushi Yamaguchi. Application of a mixed lubrication model for hydrostatic thrust bearings of hydraulic equipment. *Journal of tribology*, 115(4):686–691, 1993.

[35] A Schenk, M Zecchi, and M Ivantysynova. Accurate prediction of axial piston machines performance through a thermo-elasto-hydrodynamic simulation model. In *ASME/BATH 2013 Symposium on Fluid Power and Motion Control*, pages V001T01A034–V001T01A034. American Society of Mechanical Engineers, 2013.

[36] Matteo Pelosi and Monika Ivantysynova. Heat transfer and thermal elastic deformation analysis on the piston/cylinder interface of axial piston machines. *Journal of Tribology*, 134(4):041101, 2012.

[37] Jiong-Ki Kim, Hyoung-Eui Kim, Yong-Bum Lee, Jae-Youn Jung, and Seok-Hyung Oh. Measurment of fluid film thickness on the valve plate in oil hydraulic axial piston pumps (part ii: Spherical design effects). *Journal of mechanical Science and technology*, 19(2):655–663, 2005.

[38] Jonathan Early Baker. *Power losses in the lubricating gap between cylinder block and valve plate of swash plate type axial piston machines*. PhD thesis, PURDUE UNIVERSITY, 2008.

[39] Andrew SCHENK and Monika IVANTYSYSNOVA. An investigation of the impact of elastohydrodynamic deformation on power loss in the slipper swashplate interface. In *Symposium on Fluid Power*, volume 2011, 2011.

[40] Peter AJ Achten and Jan-Ove Palmberg. What a difference a hole makes: the commercial value of the innas hydraulic transformer. In *Proceedings of the 6th Scandinavian International Conference on Fluid Power*, pages 873–886, 1999.

[41] GEM Vael, E Orlando, and R Stukenbrock. Toward maximum flexibility in working machinery, iht control in a mecalac excavator. In *Proceedings of The 4th International Fluid Power Conference Dresden, IFK 04*, 2004.

[42] Kai Loon Cheong, Perry Y Li, and Thomas R Chase. Optimal design of power-split transmissions for hydraulic hybrid passenger vehicles. In *American Control Conference (ACC), 2011*, pages 3295–3300. IEEE, 2011.

[43] Georges Vael, Peter Achten, Jeroen Potma, and BV Innas. Cylinder control with the floating cup hydraulic transformer. *Proc. SICFP*, 2003.

[44] Rikiya INOGUCHI, Kazuhisa ITO, and Shigeru IKEO. Pure-hydraulic hybrid cylinder drive system with hydraulic transformer. *JFPS International Journal of Fluid Power System*, 5(1):1–5, 2012.

[45] Brett C Neubauer, Jonathan Nath, and William K Durfee. Design of a portable hydraulic ankle-foot orthosis. In *Engineering in Medicine and Biology Society (EMBC), 2014 36th Annual International Conference of the IEEE*, pages 1182–1185. IEEE, 2014.

[46] David A Winter. *Biomechanics and motor control of human movement*. John Wiley & Sons, 2009.

[47] Marc Raibert, Kevin Blankespoor, Gabriel Nelson, Rob Playter, et al. Bigdog, the rough-terrain quadruped robot. In *Proceedings of the 17th World Congress*, volume 17, pages 10822–10825, 2008.

Appendix A

Model Parameters for Hydraulic Transformer Simulations

The physical parameters of this transformer were obtained from measurements of a 3.15 cc Micro Pump manufactured by Takako Industries.

Table A.1: Transformer Simulation Parameters

Parameter Or Constraint	Value	Unit
Maximum Displacement of Rotating Group 1	3.15	cc
Maximum Displacement of Rotating Group 2	3.15	cc
Number of Pistons per Rotating Group	7	N/A
Maximum swashplate angle	13	degrees
Maximum allowed rotation speed	30	Hz
Maximum allowed output pressure	40	MPa
Piston diameter	9.1	mm
Piston assembly length	33	mm
Radial location of piston	15.3	mm
Shoe outer land radius	6.5	mm
Shoe inner land radius	3.5	mm
Piston leakage length at zero swash angle	25	mm
Piston chamber dead volume at zero swash angle	3.43 x 10^-7	m^3
Piston bore clearance	8	micrometer
Piston shoe average gap height	13.8	micrometer
Valve plate average gap height	16.7	micrometer
Valve plate parameter r1	9.8	mm
Valve plate parameter r2	12.8	mm
Valve plate parameter r3	17.3	mm
Valve plate parameter r4	22.3	mm
Barrel tip fraction	0.7	N/A
Bulk modulous of air-free oil	855	MPa
Discharge flow coefficient for orifice	0.5	N/A
Fluid density	860	kg/m^3
Fluid absolute viscosity	5.855e-2	m^2/s
Piston eccentricity ratio	0.9	N/A

Appendix B

Model Parameters for Hydraulic Transformer Simulations

The measured physical dimensions of several Micro Pumps manufactured by Takako Industries. These measurements were used to develop scaling laws such that the performance of units of non-measured displacements could be simulated.

Table B.1: Measured Dimensions of Takako Micropumps

Displacement of Takako Micropump	Radial distance between piston center and shaft center	Piston diameter	Piston and shoe assembly length	Outer radius of shoe land	Inner radius of shoe land
0.4 cc	7.8mm	4.5mm	16.5mm	4.0mm	1.6mm
0.8 cc	10.0mm	6.0mm	18.7mm	4.6mm	2.3mm
1.6 cc	12.3mm	7.5mm	24.0mm	5.5mm	2.7 mm
3.15 cc	15.3mm	9.1mm	33.0mm	6.5mm	3.5mm

Appendix C

List of Instrumentation and Valves

The following table gives details on the instrumentation and valves used in the experimental investigations of this thesis.

Table C.1: Instrument and valve list

Device	Specifications	Manufacturer	Part Number
Flow Meter	Positive Displacement Gear, 0.063 - 126 cc/s range	AW Gear Meters	JV#-30KG
Pressure Sensor	3000 psi	Honeywell	MLH03KPSB01A
Pressure Sensor	500 psi	Honeywell	MLH500PSB01A
Encoder	Optical, 100 counts/rev	US Digital	HB6M-100-750-NE-S-H
3/2 Directional Valve	12 gpm capacity, 50 ms response	Sun Hydraulics	DM-DAMAN812
4/2 Directional Valve	12 gpm capacity, 50 ms response	Sun Hydraulics	DNDAMNN812